PRECISE LESION FORMATION IN HISTOTRIPSY THERAPY USING STRATEGIC PULSING METHODS

by

Kuang-Wei Lin

A dissertation submitted in partial fulfillment
of the requirements of the degree of
Doctor of Philosophy
(Biomedical Engineering)
in the University of Michigan
2014

Doctoral Committee:

Professor Charles A. Cain, Chair
Professor J. Brian Fowlkes
Assistant Research Scientist Timothy L. Hall
Assistant Professor Zhen Xu

Dedication

To my family

Acknowledgement

Foremost, I would like to express my sincere gratitude to my advisor and mentor, Dr. Charles Cain, for his continuous guidance, support, patience, and encouragement throughout the years of my graduate study. I have felt very fortunate and honored to have had the opportunity to work with him, as his great motivation, enthusiasm, and dedication about research and our projects have and continue to inspire me. I would also like to thank my dissertation committee members, Drs. Brian Fowlkes, Zhen Xu, and Timothy Hall, for their advice, guidance, and help, which greatly improved the quality of this dissertation. Brian's expertise in acoustics and ultrasound imaging, especially bubble dynamics and ultrasound contrast imaging, provided me with a solid background and source for my questions. Zhen accepted me into the lab and guided me toward my very first project. She not only continues providing valuable guidance and support in my research, but also has provided valuable advice to my wife and I as new parents. As an expert in laboratory instruments, Tim introduced me to designing transducers and shared his knowledge in amplifiers, general electronics, and optics. I greatly appreciate his patience throughout the process.

The current and former members in the Histotripsy lab also deserve my sincerest appreciations, including Dr. Tzu-Yin Wang, Dr. Adam Maxwell, Dr. Yohan Kim, Dr. Jonathan Sukovich, Ryan Miller, Alex Duryea, Eli Vlaisavljevich, Steven Allen, Simone Park, Xi Zhang, Hedieh Tamaddoni, and Yige Li. I especially thank Tzu-Yin, who was a senior student when I first came into lab. She taught me everything she knew and learned in the lab, ranging from the

very basics, like how to use specific lab equipment, to how to perform a controlled study with minimal confounding error. She also oriented me to life in Ann Arbor when I first arrived, providing sound advice and sharing her experience about living in Ann Arbor. Throughout my graduate study, Adam's expertise was the key to my understanding about of acoustics, cavitation, and transducer design. When I had questions regarding electronics, Yohan was indispensable, and he shared a great deal of his experience with low-frequency transducer design and lent me his first transcranial transducer for the intrinsic threshold study. Alex, who is very astute at construction, assisted me in designing and assembling my dual frequency transducer after sharing with me his 2-cm modular design. As a fellow Wolverine, I will miss our talks about Michigan football and basketball in particular. Ryan, Eli, Steven, Simone, Xi, Jonathan, Hedieh, and Yige were fun-loving companions in the lab and on conference trips, and I am grateful for the friendship.

I wish to thank my colleagues in Urology, Radiology, and Pediatric-Cardiology, Drs. William Roberts, Kimberly Ives, Oliver Kripfgans, and Gabe Owens. Will, for allowing me to use his laboratory facilities and the insightful discussion about clinical applications of histotripsy. Kim, for her valuable assistance in animal studies and tissue excision. Oliver, for providing such a well-managed machine shop. Gabe, for sharing his knowledge and expertise in cardiology.

I also want to thank Dr. Cheri Deng for lending me her VisualSonics ultrasound system and Dr. Ronald Kumon for sharing his knowledge on tissue characterization. Former and present members of Dr. Deng's lab, including Drs. Zhenzhen Fan, Yi-Sing (Tina) Hsiao, Ziqi Wu, Madhu Gudur and Di Chen, became supportive friends and colleagues throughout.

I also appreciate the acute and inspiring discussion with Dr. Yousuf Khalifa from the University of Rochester about ophthalmological applications for histotripsy.

Additionally, I'm grateful to all of our administrative staff, who kept everything running smoothly in the lab, especially to Kathleen McCrumb and Maria Steele. Kathy helped me place orders and receive reimbursements. She cared about students and was willing to share my joy in my personal life events when I got married and had my first child. Maria straightened out my student paperwork and always welcomed me warmly whenever I asked questions.

Last, but not the least, I would like to thank my family for their ever-lasting support and love. My parents, Wen-Chan Lin (Dad) and Chin-Chih Chang (Mom), who raised me up and provided me with a fine education that brought me to this point, they cared, supported, and encouraged me from very little things to major life events. I'd like to say how fortunate and grateful I am to have my beloved wife, Min-Lee Yang, who I greatly appreciate for her support, encouragement, and love, and she was always with me throughout this journey. I also want to thank my in-laws for their unconditional support. And, finally, to my daughter, Olivia Lin, I thank her for the joy and excitement that she brought me these last few months of dissertation writing and now for the rest of my life.

Ann Arbor, Michigan

March, 2014

Table of Contents

List of Figures

List of Tables

Abstract

Histotripsy is a noninvasive, cavitation-based ultrasound therapy that can create mechanical tissue ablation through dense energetic clouds of microbubbles generated by high-pressure and short ultrasound pulses. These microbubbles in the clouds act as “micro-scalpels” and mechanically fractionate tissue into a liquid homogenate with a well-demarcated boundary. Histotripsy therapy has been shown capable of 1) creating intracardiac flow channels for congenital heart disease treatment, 2) fractionating blood clots for treating deep vein thrombosis, 3) fractionating prostatic tissue for benign prostatic hyperplasia (BPH) treatments, and 4) fragmenting model renal calculi for treating kidney stone. Many other applications are being studied.

The overall objective of this dissertation is to develop ultrasound pulsing techniques that can lead to more precise and controlled bubble cloud generation in histotripsy therapy. Three strategic pulsing methods have been developed and characterized in this dissertation.

1) Bubble cloud formation using the intrinsic threshold mechanism: when ultrasound pulses shorter than 3 cycles are applied, the generation of bubble clouds only depends on one or two negative half cycles exceeding an intrinsic threshold of the medium. This intrinsic threshold is highly repeatable and has a very sharp transition zone. At negative pressure amplitudes not significantly greater than this, a dense energetic lesion-forming bubble cloud is generated consistently with a spatial pattern similar to the part of the negative half cycles(s) exceeding the intrinsic threshold.

2) Dual-beam histotripsy: a low-frequency pump pulse is applied to enable a high-frequency probe pulse to exceed the intrinsic threshold. The high-frequency probe pulse provides precision in lesion formation, while the low-frequency pump pulse, which is more resistant to attenuation and aberration, raises the pressure level of the targeted treatment region.

3) Frequency compounding: a near half-cycle (monopolar) pulse is synthesized using an array transducer composed of elements with various resonant frequencies. Histotripsy using a negative-polarity half-cycle pulse can limit the influence of positive phases on bubble cloud generation, leading to a more precise and controlled lesion formation.

These three techniques were realized using custom design ultrasound array transducers and examined in red-blood-cell tissue-mimicking phantoms, and the first two techniques were further validated in *ex vivo* tissues. Additionally, an application in metastatic lymph node ablation is studied *in vivo* using supra-intrinsic-threshold pulses.

In conclusion, this dissertation demonstrates three strategic ultrasound pulsing methods that can lead to precise lesion formation in histotripsy therapy. Future work involves examining the applicability of these pulsing methods in *in vivo* experiments and studying potential applications for monopolar pulses in ultrasound diagnostic imaging.

Chapter 1
Introduction

The main objective of this dissertation is to investigate approaches for precise lesion formation using a pulsed cavitational ultrasound therapy, or histotripsy. More specifically, this work explores strategic histotripsy pulsing sequences for precise lesion formation, including 1) supra-intrinsic-threshold short (< 1.5 cycles) acoustic pulses, 2) dual-frequency acoustic pulses wherein a high-frequency probe pulse is enabled by a low-frequency probe pulse to exceed the intrinsic threshold, and 3) near half-cycle (monopolar) acoustic pulses generated by a multiple-frequency transducer (frequency compounding). The treatment effect of these pulsing sequences is evaluated using red-blood-cell tissue mimicking phantoms and validated in excised tissues. Lastly, a potential application in metastatic lymph node ablation using this precise lesion formation is discussed and studied with an *in vivo* acute porcine model, in addition to *ex vivo* excised porcine lymph node treatments.

This chapter will give a brief introduction to histotripsy therapy, followed by an overview of two bubble cloud formation mechanisms (shockwave backscattering and intrinsic threshold) used in histotripsy therapy. The bubble cloud formation mechanism is introduced since the concept of the intrinsic threshold mechanism is an essential component of this work, and it will be constantly used and referred to throughout this dissertation. This chapter will then be concluded with an outline of the dissertation, which provides an overview of each chapter.

1.1 Histotripsy Therapy

Histotripsy is a noninvasive, cavitation-based, ultrasound therapy that uses very short (< 20 cycles), high-pressure (peak negative pressure [P–] > 10 MPa), and low duty-cycle (<1%) ultrasound pulses to generate a dense, energetic, lesion-producing bubble cloud. These micron-sized bubbles in the cloud act as "micro-scalpels," which can fractionate soft tissues into sub-cellular debris with a very sharp boundary. This histotripsy therapy can create controlled tissue erosion when it is targeted at a fluid-tissue interface, e.g. removing cardiac tissue and creating intracardiac flow channels for congenital heart disease [1-3]. Histotripsy can also generate localized well-demarcated tissue fractionation when it is targeted within bulk tissue, e.g. prostatic tissue ablation for treating benign prostatic hyperplasia (BPH) [4-8] and hepatic tissue ablation for liver tumor treatment [9]. Additionally, histotripsy has been shown capable of fragmenting model kidney stones using surface erosion that is mechanistically distinct from conventional shockwave lithotripsy (SWL) [10, 11].

Histotripsy therapy can be guided and monitored using ultrasound B-mode imaging in real-time, since 1) the cavitating bubble cloud appears as a temporally changing hyperechoic region in B-mode imaging, allowing the treatment to be precisely targeted, and 2) the echogenicity of the targeted region decreases as the degree of tissue fractionation increases, which can be used as a way of monitoring lesion production (image feedback) in real-time [12-14]. Moreover, recent studies showed that histotripsy therapy could also be monitored by elasticity-based image feedback: 1)Wang *et al.* used shear wave elastography to monitor the elasticity change in tissue and found out this elasticity-based metric is more sensitive in detecting histotripsy-induced lesions in early stages, compared to B-mode imaging [15], and 2) Miller *et al.*

used color Doppler to detect histotripsy bubble cloud induced motion in the increasingly softer tissue resulting from histotripsy fractionation [16].

Histotripsy therapy, which mechanically ablates soft tissue through acoustic cavitation, is mechanistically different from high intensity focused ultrasound (HIFU) therapy [17, 18]. In HIFU, the energy of propagated ultrasound beams is deposited into tissue as heat, which rapidly raises its local temperature above a certain threshold (56℃ for 1 second), thus resulting in irreversible cell death through coagulative necrosis [17, 18]. This HIFU therapy operates at a lower pressure level with a much higher duty cycle than histotripsy wherein the treatment effect heavily relies on the thermal dose that it imposes on the tissue. Additionally, HIFU therapy often requires other imaging modalities for treatment monitoring since conventional b-mode ultrasound imaging cannot provide sufficient image contrast between coagulated and unaffected tissue. Magnetic resonance (MR) imaging has the advantage of better image quality and the ability to monitor temperature (treatment targeting) and it has been used widely in HIFU treatment monitoring [19-22]. However, MR imaging is expensive, often slow and more complex than ultrasound imaging. Some recent studies also investigated the potential of using ultrasound elastography to monitor HIFU treatment [23, 24].

Additionally, histotripsy is mechanistically different from another ultrasound therapy that uses rapid boiling as a mechanism to create bubbles for emulsification [25-27]. In this therapy, millisecond-duration, shocked, focused ultrasound pulses are applied to induce rapid heating and boiling of the medium, thus producing the large bubbles used in its mechanical action.

1.2 Shock Scattering Mechanism for Bubble Cloud Formation

In conventional histotripsy treatments, ultrasound pulses with ≥ 3 acoustic cycles are applied, and the bubble cloud formation relies on the pressure release scattering of the positive shock fronts (sometimes exceeding 100 MPa, P+) from initially generated, sparsely distributed bubbles (or a single bubble). This has been called the "shock scattering mechanism" [28]. This mechanism depends on one (or a few sparsely distributed) bubble(s) initiated with the primary negative half cycle(s) of the pulse at the focus of the transducer. A cloud of microbubbles then forms due to the pressure release backscattering of the high peak positive shock fronts from these sparsely initiated bubbles. These back-scattered high-amplitude rarefactional waves exceed the intrinsic threshold, thus producing a localized dense bubble cloud. Each of the following acoustic cycles then induces further cavitation by the backscattering from the bubble cloud surface, which grows towards the transducer. As a result, an elongated dense bubble cloud growing along the acoustic axis opposite the ultrasound propagation direction is observed with the shock scattering mechanism. This shock scattering process makes the bubble cloud generation not only dependent on the peak negative pressure, but also on the number of acoustic cycles and the amplitudes of the positive shocks. Without these intense shock fronts developed by nonlinear propagation, no dense bubble clouds are generated when the peak negative half-cycles are below the intrinsic threshold.

Therefore, the cavitation threshold for the shock scattering mechanism varies with the applied exposure conditions, and the reported thresholds (P–) range from 6 to 15 MPa [29, 30] for degassed water and 13.5 to 21 MPa in tissue and tissue phantoms [28, 31]. The spatial extent of the bubble cloud is not well-defined, and it changes with the variation in shock scattering process created by different exposure conditions. Moreover, for pulses longer than about 8–10

cycles, the elongating bubble cloud moves out of the focal zone. Thus, longer pulses do not necessarily enhance lesion formation [32].

A more recent study by Maxwell *et al* [33] using numerical modeling and simulation shows that the P– of the backscattered shockwave increases with the size of the pre-existing bubble that provides the pressure-release scattering surface. Additionally, if the pre-existing bubble is hemispherical, which provides a flattened scattering surface, it can result in higher P– for the backscattered shockwave, compared to that backscattered from a convex scattering surface provided by a spherical bubble.

1.3 Intrinsic Threshold Mechanism for Bubble Cloud Formation

In another work by Maxwell *et al* [34], a second mechanism for bubble cloud formation was proposed and investigated. This occurs when one or more negative half cycle(s) of the applied ultrasound pulses exceed(s) an "intrinsic threshold" of the medium, thus directly forming a dense bubble cloud without shock scattering. This intrinsic threshold is defined by a very sharp transition zone and is relatively insensitive to the inhomogeneities in soft tissue or the lack of dissolved gases. Moreover, this intrinsic threshold is independent on the applied positive pressure, since the influence of shock scattering is minimized when applying pulses fewer than 2 cycles. The reported threshold (P–), where the probability of cavitation (formation of a dense bubble cloud) for one single pulse is 0.5, is between 26.4 – 30.0 MPa in samples with high water content, including water, hydrogel, and soft tissue.

Because of the sharp, highly repeatable threshold, at negative pressure amplitudes not significantly greater than this, a dense energetic lesion-forming cloud of microbubbles is generated consistently with a spatial pattern similar to the part of the negative half cycles(s)

exceeding the intrinsic threshold. That part of the therapy pulse exceeding intrinsic threshold, and the resulting spatial extent of the lesion forming bubble cloud, are independent of positive shocks and the somewhat chaotic shock scattering phenomenon. Therefore, the spatial extent of the lesion generated using this mechanism is expected to be well-defined and more predictable. The lesion size can be easily controlled, even for small lesions, simply by a precise adjustment of the therapy pulse amplitude.

1.4 Outline of this dissertation

This dissertation is organized in seven chapters to present techniques for precise lesion formation and potential applications that requires precise lesion formation.

Chapter 1 describes the objective of this dissertation and introduces histotripsy therapy and the two bubble cloud formation mechanisms for histotripsy. Additionally, it gives an overview of the topics discussed in this dissertation.

Chapter 2 investigates lesion formation using the intrinsic threshold mechanism. It examines the characteristics of the lesions generated with supra-intrinsic-threshold 1.5-cycle pulses at various pressure levels, and the correspondence between the size of the lesions and the size of the focal region exceeding the intrinsic threshold.

Chapter 3 proposes a dual-frequency excitation method for precise lesion formation, called “dual-beam histotripsy,” wherein a low-frequency pump pulse is applied to enable a high-frequency probe pulse to exceed the intrinsic threshold. The low-frequency pump pulses, which is more resistant to acoustic attenuation and aberration, can raise the P– level for a region of interest (ROI); while the high-frequency probe pulses, which provides more precision, can pin-point a targeted location within the ROI and raise its P– above the intrinsic threshold.

Chapter 4 utilizes the dual-beam histotripsy technique and studies the lesion formation using an ultrasound imaging transducer enabled by a low-frequency pump transducer. One advantage of using an imaging transducer is that it provides the steering capability for lesion formation when it is driven by a programmable ultrasound system.

Chapter 5 proposes a novel "frequency compounding" approach to synthesize a near monopolar (half-cycle) pulse using an array transducer composed of elements with various resonant frequencies. The time delays of individual frequency components are varied to allow them to constructively interfere at the focus. These monopolar pulses can further limit shock scattering during histotripsy treatment, making the lesion formation more predictable and controllable. They also have many interesting applications in ultrasound imaging.

Chapter 6 explores an application in metastatic lymph node ablation using histotripsy therapy. In this application, precise lesion formation is required at a superficial target since lymph nodes are generally small (5 – 40 mm) and shallow (5 – 50 mm). In this chapter, histotripsy therapy is performed in porcine lymph nodes, using both shock scattering and intrinsic threshold mechanisms.

Chapter 7 summarizes the findings and contributions of this dissertation, and discusses future work and potential applications for these precise lesion formation techniques.

1.5 References

[1] Z. Xu, A. Ludomirsky, L. Y. Eun, T. L. Hall, B. C. Tran, J. B. Fowlkes, and C. A. Cain, "Controlled ultrasound tissue erosion," *IEEE Trans Ultrason Ferroelectr Freq Control*, vol. 51, pp. 726-36, Jun 2004.

[2] Z. Xu, G. Owens, D. Gordon, C. Cain, and A. Ludomirsky, "Noninvasive creation of an atrial septal defect by histotripsy in a canine model," *Circulation*, vol. 121, pp. 742-9, Feb 16 2010.

[3] G. E. Owens, R. M. Miller, G. Ensing, K. Ives, D. Gordon, A. Ludomirsky, and Z. Xu, "Therapeutic ultrasound to noninvasively create intracardiac communications in an intact animal model," *Catheterization and Cardiovascular Interventions,* vol. 77, pp. 580-588, 2011.

[4] J. E. Parsons, C. A. Cain, G. D. Abrams, and J. B. Fowlkes, "Pulsed cavitational ultrasound therapy for controlled tissue homogenization," *Ultrasound Med Biol,* vol. 32, pp. 115-29, Jan 2006.

[5] W. W. Roberts, "Focused ultrasound ablation of renal and prostate cancer: current technology and future directions," *Urol Oncol,* vol. 23, pp. 367-71, Sep-Oct 2005.

[6] A. M. Lake, T. L. Hall, K. Kieran, J. B. Fowlkes, C. A. Cain, and W. W. Roberts, "Histotripsy: Minimally Invasive Technology for Prostatic Tissue Ablation in an In Vivo Canine Model," *Urology,* vol. 72, pp. 682-686, 2008.

[7] C. R. Hempel, T. L. Hall, C. A. Cain, J. B. Fowlkes, Z. Xu, and W. W. Roberts, "Histotripsy Fractionation of Prostate Tissue: Local Effects and Systemic Response in a Canine Model," *The Journal of Urology,* vol. 185, pp. 1484-1489, 2011.

[8] G. R. Schade, T. L. Hall, and W. W. Roberts, "Urethral-sparing Histotripsy of the Prostate in a Canine Model," *Urology,* vol. 80, pp. 730-735, 2012.

[9] E. Vlaisavljevich, Y. Kim, S. Allen, G. Owens, S. Pelletier, C. Cain, K. Ives, and Z. Xu, "Image-Guided Non-Invasive Ultrasound Liver Ablation Using Histotripsy: Feasibility Study in an In Vivo Porcine Model," *Ultrasound in medicine & biology,* vol. 39, pp. 1398-1409, 2013.

[10] A. P. Duryea, T. L. Hall, A. D. Maxwell, Z. Xu, C. A. Cain, and W. W. Roberts, "Histotripsy erosion of model urinary calculi," *J Endourol,* vol. 25, pp. 341-4, Feb 2011.

[11] A. P. Duryea, A. D. Maxwell, W. W. Roberts, Z. Xu, T. L. Hall, and C. A. Cain, "In vitro comminution of model renal calculi using histotripsy," *IEEE Trans Ultrason Ferroelectr Freq Control,* vol. 58, pp. 971-80, May 2011.

[12] B. A. Rabkin, V. Zderic, and S. Vaezy, "Hyperecho in ultrasound images of HIFU therapy: involvement of cavitation," *Ultrasound Med Biol,* vol. 31, pp. 947-56, Jul 2005.

[13] T. L. Hall, J. B. Fowlkes, and C. A. Cain, "A real-time measure of cavitation induced tissue disruption by ultrasound imaging backscatter reduction," *IEEE Trans Ultrason Ferroelectr Freq Control,* vol. 54, pp. 569-75, Mar 2007.

[14] T. Y. Wang, Z. Xu, F. Winterroth, T. L. Hall, J. B. Fowlkes, E. D. Rothman, W. W. Roberts, and C. A. Cain, "Quantitative ultrasound backscatter for pulsed cavitational ultrasound therapy- histotripsy," *IEEE Trans Ultrason Ferroelectr Freq Control,* vol. 56, pp. 995-1005, May 2009.

[15] T. Y. Wang, T. L. Hall, Z. Xu, J. B. Fowlkes, and C. A. Cain, "Imaging feedback of histotripsy treatments using ultrasound shear wave elastography," *Ultrasonics, Ferroelectrics and Frequency Control, IEEE Transactions on,* vol. 59, pp. 1167-1181, 2012.

[16] R. M. Miller, A. D. Maxwell, T.-Y. Wang, J. B. Fowlkes, C. A. Cain, and X. Zhen, "Real-time elastography-based monitoring of histotripsy tissue fractionation using color Doppler," in *Ultrasonics Symposium (IUS), 2012 IEEE International*, 2012, pp. 196-199.

[17] J. E. Kennedy, G. R. ter Haar, and D. Cranston, "High intensity focused ultrasound: surgery of the future?," *The British Journal of Radiology,* vol. 76, pp. 590-599, 2003.

[18] J. E. Kennedy, "High-intensity focused ultrasound in the treatment of solid tumours," *Nat Rev Cancer,* vol. 5, pp. 321-7, Apr 2005.

[19] K. Hynynen, O. Pomeroy, D. N. Smith, P. E. Huber, N. J. McDannold, J. Kettenbach, J. Baum, S. Singer, and F. A. Jolesz, "MR Imaging-guided Focused Ultrasound Surgery of Fibroadenomas in the Breast: A Feasibility Study," *Radiology,* vol. 219, pp. 176-185, 2001.

[20] Z. Ram, Z. R. Cohen, S. Harnof, S. Tal, M. Faibel, D. Nass, S. E. Maier, M. Hadani, and Y. Mardor, "Magnetic Resonance Imaging-Guided, High-Intensity Focused Ultrasound for Brain Tumor Therapy," *Neurosurgery,* vol. 59, pp. 949-956 10.1227/01.NEU.0000254439.02736.D8, 2006.

[21] F. A. Taran, C. M. C. Tempany, L. Regan, Y. Inbar, A. Revel, and E. A. Stewart, "Magnetic resonance-guided focused ultrasound (MRgFUS) compared with abdominal hysterectomy for treatment of uterine leiomyomas," *Ultrasound in Obstetrics and Gynecology,* vol. 34, pp. 572-578, 2009.

[22] R. Catane, A. Beck, Y. Inbar, T. Rabin, N. Shabshin, S. Hengst, R. Pfeffer, A. Hanannel, O. Dogadkin, B. Liberman, and D. Kopelman, "MR-guided focused ultrasound surgery (MRgFUS) for the palliation of pain in patients with bone metastases—preliminary clinical experience," *Annals of Oncology,* vol. 18, pp. 163-167, January 1, 2007 2007.

[23] R. Righetti, F. Kallel, R. J. Stafford, R. E. Price, T. A. Krouskop, J. D. Hazle, and J. Ophir, "Elastographic characterization of HIFU-induced lesions in canine livers," *Ultrasound in medicine & biology,* vol. 25, pp. 1099-1113, 1999.

[24] L. Curiel, R. Souchon, O. Rouvière, A. Gelet, and J. Y. Chapelon, "Elastography for the follow-up of high-intensity focused ultrasound prostate cancer treatment: Initial comparison with MRI," *Ultrasound in medicine & biology,* vol. 31, pp. 1461-1468, 2005.

[25] M. S. Canney, V. A. Khokhlova, O. V. Bessonova, M. R. Bailey, and L. A. Crum, "Shock-Induced Heating and Millisecond Boiling in Gels and Tissue Due to High Intensity Focused Ultrasound," *Ultrasound in medicine & biology,* vol. 36, pp. 250-267, 2010.

[26] V. A. Khokhlova, M. R. Bailey, J. A. Reed, B. W. Cunitz, P. J. Kaczkowski, and L. A. Crum, "Effects of nonlinear propagation, cavitation, and boiling in lesion formation by high intensity focused ultrasound in a gel phantom," *The Journal of the Acoustical Society of America*, vol. 119, pp. 1834-1848, 2006.

[27] B. A. Rabkin, V. Zderic, L. A. Crum, and S. Vaezy, "Biological and physical mechanisms of HIFU-induced hyperecho in ultrasound images," *Ultrasound in medicine & biology*, vol. 32, pp. 1721-1729, 2006.

[28] A. D. Maxwell, T. Y. Wang, C. A. Cain, J. B. Fowlkes, O. A. Sapozhnikov, M. R. Bailey, and Z. Xu, "Cavitation clouds created by shock scattering from bubbles during histotripsy," *J Acoust Soc Am*, vol. 130, pp. 1888-98, Oct 2011.

[29] Z. Xu, J. B. Fowlkes, A. Ludomirsky, and C. A. Cain, "Investigation of intensity thresholds for ultrasound tissue erosion," *Ultrasound in Medicine & Biology*, vol. 31, pp. 1673-1682, 2005.

[30] A. D. Maxwell, C. A. Cain, A. P. Duryea, L. Yuan, H. S. Gurm, and Z. Xu, "Noninvasive Thrombolysis Using Pulsed Ultrasound Cavitation Therapy ??Histotripsy," *Ultrasound in medicine & biology*, vol. 35, pp. 1982-1994, 2009.

[31] Z. Xu, T. L. Hall, J. B. Fowlkes, and C. A. Cain, "Effects of acoustic parameters on bubble cloud dynamics in ultrasound tissue erosion (histotripsy)," *The Journal of the Acoustical Society of America*, vol. 122, pp. 229-236, 2007.

[32] T.-Y. Wang, A. D. Maxwell, S. Park, Z. Xu, J. B. Fowlkes, and C. A. Cain, "Why Are Short Pulses More Efficient in Tissue Erosion Using Pulsed Cavitational Ultrasound Therapy (Histotripsy)?," vol. 1215, H. Kullervo and S. Jacques, Eds., ed: AIP, 2009, pp. 40-43.

[33] A. D. Maxwell, E. Johnson, J. B. Fowlkes, C. A. Cain, and Z. Xu, "Numerical modeling and simulation of focused shocks scattering from bubbles during histotripsy " *Journal of Acoustic Society of America*, submitted Dec. 2013 (In Review).

[34] A. D. Maxwell, C. A. Cain, T. L. Hall, J. B. Fowlkes, and Z. Xu, "Probability of Cavitation for Single Ultrasound Pulses Applied to Tissues and Tissue-Mimicking Materials," *Ultrasound Med Biol*, vol. 39, pp. 449-465, 2013.

Chapter 2
Microtripsy: Precise Lesion Formation using the Intrinsic Threshold Mechanism

A majority component of this chapter has been published in *IEEE Transactions on Ultrasonics, Ferroelectric, and Frequency Control* © 2014 IEEE. Reprinted, with permission, from [1].

2.1 Introduction

Conventional histotripsy treatments use ultrasound pulses with ≥ 3 acoustic cycles and the bubble cloud formation relies on the pressure release scattering of the positive shock fronts from initially generated, sparsely distributed bubbles, which is called the "shock scattering mechanism" [2]. This shock scattering process makes the bubble cloud generation not only dependent on the peak negative pressure, but also on the number of acoustic cycles and the amplitudes of the positive shocks. Without these intense shock fronts developed by nonlinear propagation, no dense bubble clouds are generated when the peak negative half-cycles are below the intrinsic threshold.

In a recent work [3], a second mechanism for bubble cloud formation was proposed and investigated. This occurs when one or more negative half cycle(s) of the applied ultrasound pulses exceed(s) an "intrinsic threshold" of the medium, thus directly forming a dense bubble cloud without shock scattering. This intrinsic threshold is defined by a very sharp transition zone and is relatively insensitive to the inhomogeneities in soft tissue or the lack of dissolved gases.

The reported threshold (P–), where the probability of dense bubble cloud formation for one single pulse is 0.5, is between 26.4 – 30.0 MPa in samples with high water content, including water, hydrogel, and soft tissue. Because of the sharp, highly repeatable threshold, at negative pressure amplitudes not significantly greater than this, a dense energetic lesion-forming cloud of microbubbles is generated consistently with a spatial pattern similar to the part of the negative half cycles(s) exceeding the intrinsic threshold.

In this chapter, the characteristics of the lesions generated by the intrinsic threshold mechanism were investigated using red-blood-cell (RBC) tissue-mimicking phantoms and *ex vivo* canine tissues. More specifically, a 500 kHz therapy transducer, which generated histotripsy pulses of less than 2 cycles, was used, and various sizes of lesions in RBC phantoms and canine tissues were generated using various acoustic pressure levels. The smallest possible lesion that could be generated consistently with this transducer was tested by lowering the applied acoustic pressure to a level that was just above the intrinsic cavitation threshold. The lesion sizes in RBC phantoms were quantified based on the optical images taken by a high speed camera, and the lesion sizes in *ex vivo* tissue were quantified based on ultrasound B-mode images and histological sections. Estimates for the sizes of the lesions based on how large the focal regions were above the cavitation thresholds were also computed and compared to the sizes of the lesions generated experimentally.

2.2 Methods

2.2.1 Sample preparation

Experiments were performed on red-blood-cell (RBC) tissue-mimicking phantoms and *ex vivo* canine kidneys and livers. The procedures described in this study were approved by the University of Michigan's Committee on Use and Care of Animals.

The RBC tissue-mimicking phantom can be used for the visualization and quantification for cavitation-induced damage [4]. In this study, fresh canine blood was obtained from adult research canine subjects in an unrelated study. An anticoagulant solution of citrate-phosphate-dextrose (CPD) (C7165, Sigma-Aldrich, St. Loius, MO, USA) was added to the blood with a CPD-to-blood ratio of 1:9 (v:v), and kept at 4℃ before usage. The blood stored under these conditions could last for approximately one month, and, in this study, it was used within three weeks after blood collection. The RBC phantoms were prepared from an agarose-saline mixture and RBCs, following the protocols described in a previous paper [4]. The agarose-saline mixture consists of low-melting-point agarose powder (AG-SP, LabScientific, Livingston, NJ, USA) and 0.9% saline at an agarose-to-saline ratio of 1:100 (w:v). This RBC tissue-mimicking phantom has a three-layer structure with a very thin (~500 μm) RBC-agarose-saline hydrogel layer in the center, and a transparent agarose-saline hydrogel layer (~2 cm thick) on the top and at the bottom. The central RBC-agarose layer serves as a real-time indicator for cavitational damage, since, at the place where cavitational damage is induced, the RBC-agarose mixture will change from translucent and red to transparent and colorless within one second due to RBC lysis [4].

Experiments were also performed in *ex vivo* canine kidneys and livers to validate the results observed in the RBC phantoms. The excised canine kidneys and livers were collected from adult canine subjects from an unrelated study, kept in 0.9% saline at 4℃, and used within

36 hours. Before the experiments, the kidneys and livers were submerged in degassed 0.9% saline and placed in a chamber under partial vacuum (~33 kPa absolute) at room temperature for 1–2 hours. The tissues were then sectioned into small specimens (~3×3×3 cm) and embedded in a 1% agarose hydrogel that consisted of low-melting-point agarose and 0.9% saline.

2.2.2 Transducer Calibration

Histotripsy pulses were generated by a 32-element, 500 kHz therapy transducer that was directly mounted on one side of a water tank filled with degassed water at room temperature (40% of normal saturation determined by pO_2). The gas saturation was measured by a commercial dissolved oxygen meter (YSI5000, YSI Inc., Yellow Springs, OH, USA). The active elements in the transducer consisted of 50.8 mm diameter PZT-8 discs, each individually mounted to an acoustic lens with a geometric focus of 150 mm. The elements were arranged in a large hemispherical configuration with an f-number of approximately 0.5. To generate short therapy pulses, a custom high voltage pulser developed in-house was used to drive the transducer elements. The pulser was connected to a field-programmable gated array (FPGA) development board (Altera DE1, Terasic Technology, Dover, DE, USA) specifically programmed for histotripsy therapy pulsing. This setup allowed the transducer to output short pulses consisting of less than two cycles.

A fiber-optic probe hydrophone (FOPH) adapted from a previously published design [5] was used to measure the acoustic output pressure of the therapy transducer. Figure 2.1(a) shows the directly measured, free-field acoustic waveform of a typical histotripsy pulse generated by the 32-element, 500 kHz therapy transducer prior to inducing cavitation on the tip of FOPH. The peak negative pressures beyond the cavitation threshold were estimated by the summation of the

output focal P– from individual elements. Above the cavitation threshold, the glass fiber sensor was consistently shattered. In the previous study [3], this estimate had a good agreement with the P– measured directly in a higher cavitation threshold medium, 1,3 butanediol. Furthermore, for the therapy transducer used in this study, each element was self-focused, and their acoustic waves did not overlap significantly until they reached the focus.

Figure 2.1(b) plots the focal acoustic pressure as a function of the peak-to-peak electrical driving voltage (to one representative element in the therapy transducer), with both axes in logarithmic scales. The actual P– values prior to reaching cavitation threshold were measured directly by driving all the elements at the same time, and plotted as solid circles (●). The estimated P– values from the summation of individual elements are plotted as squares (□). The P– estimates from the summation showed a similar trend as the ones from the direct measurement, and they had a good agreement at the driving voltage of 492 Volts where P– = 20.9 MPa via direct measurement and P– = 21.0 MPa via the estimate from summation. The −6dB beamwidths (calculated based on P–) at the output pressure level of P– = 8.5 MPa were measured to be 1.80 and 4.04 mm in the lateral and axial directions, respectively.

Rectangular, custom-made, plastic gel holders (4×4×8 cm) with acoustically transparent membranes (50μm thick clear DuraLar polyester films, McMaster-Carr, Aurora, OH) glued on their sides, as shown in Figure 2.1(c), were used to hold the RBC phantoms and agarose-hydrogel-embedded tissue specimens. The influence of the plastic gel holders on focal P– and one-directional (1D) beam profiles was also investigated. Based on the acoustic pressure measurement with the plastic gel holder in place, the P– was attenuated by 12% (1.1 dB), and this attenuation could be attributed to both the reflection due to impedance mismatch and absorption in the plastic material. However, the 1D beam profiles in lateral and axial directions

did not change significantly, as shown in Figures 2.1(d) and 2.1(e). The applied P– was then corrected by the attenuation contributed by the plastic gel holder. Additionally, the applied P– was further linearly corrected for the attenuation contributed by agarose hydrogel and canine specimens with previously reported attenuation coefficients [3, 4, 6]. Tables 2.1 and 2.2 list the estimated P– used in the RBC Phantom experiments and ex vivo canine tissue experiments, respectively.

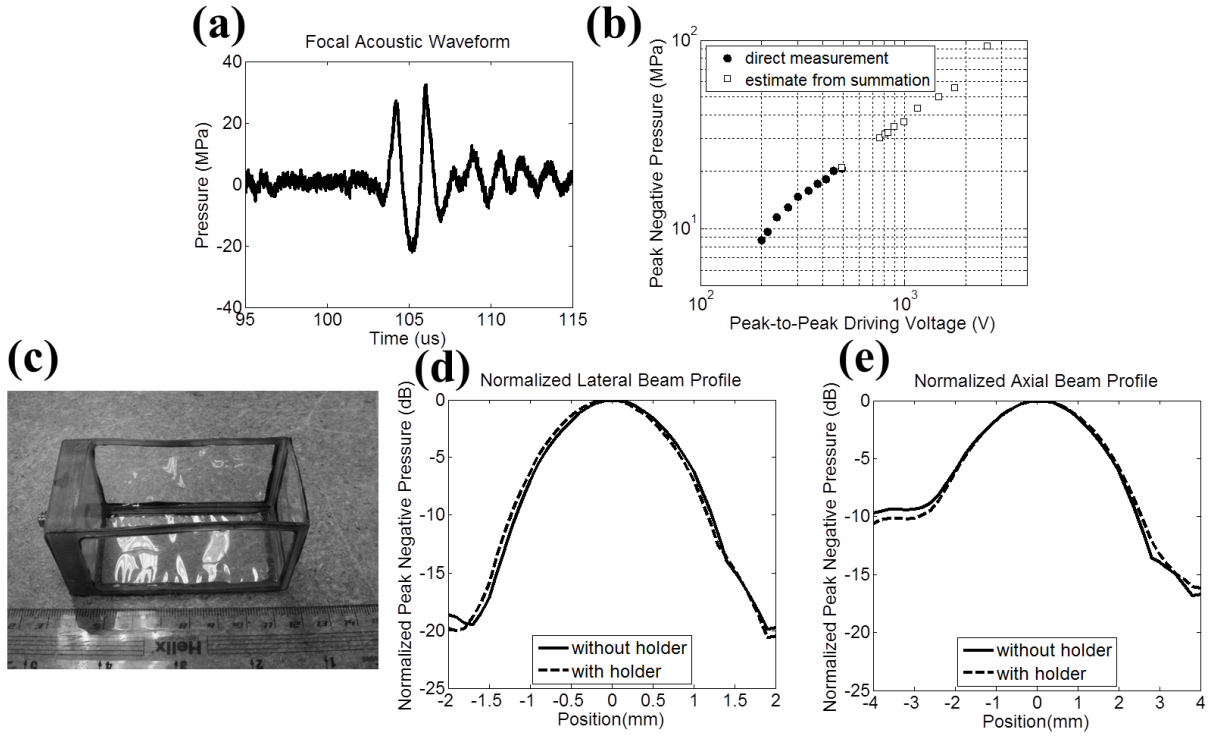

Figure 2.1 Histotripsy pulse calibration (a) A representative free-field 1.5-cycle acoustic waveform for the 500 kHz therapy transducer. (b) A plot of the measured focal P– versus the peak-to-peak electrical driving voltage (c) A photograph of the gel holder. (d) Normalized lateral beam profile. (e) Normalized axial beam profile.

2.2.3 Treatment in red-blood-cell phantoms and lesion analysis

The experiment setup in the RBC phantom experiment is illustrated in Figure 2.2. Besides the histotripsy pulse generation described in the previous section, a digital, CMOS, high-speed camera (Phantom V210, Vision Research, Wayne, NJ, USA) was positioned

perpendicularly to the water tank in an orientation that allowed for the visualization of the axial-lateral plane of the therapy transducer. The camera received trigger signals from the FPGA board, which maintained the synchronization of image capturing and the delivery of histotripsy pulses. The RBC phantoms were mounted on a 3-axis motorized positioner (Parker, Cleveland, OH, USA), submerged in the water tank with the corresponding orientation for the visualization of axial-lateral-plane lesions, and illuminated by a continuous wave (CW) white light source for high speed photography. The RBC phantom, therapy transducer, and camera were aligned by visually adjusting the sharpness of the RBC layer and the cavitation bubble as they appeared in the high speed images.

Each intended treatment region in the RBC phantoms was exposed to 500 histotripsy pulses at a PRF of 1 Hz. Single-focal-point exposures were performed in each case. A PRF of 1 Hz was chosen to exclude the contribution of the cavitation memory effect described in a previous paper [7]. Pressure levels listed in column 4 of Table 2.1 were used in these RBC phantom experiments.

Table 2.1 Pressure levels used in the RBC phantom experiments of the microtripsy study

Peak-to-Peak Electrical Driving Voltage* (Volts)	Estimated Focal P– from Summation of Individual Elements (MPa)	Focal P– with Attenuation Correction (MPa)	
		Gel Holder	Agarose Hydrogel
685	28.3	25.0	24.5
757	30.3	26.7	26.2
801	31.6	27.8	27.3
831	32.2	28.4	27.9
995	36.9	32.6	32.0
1165	43.7	38.5	37.8
1474	49.9	44.0	43.2
1764	56.0	49.4	48.5
2547	93.2	82.2	80.7

* The peak-to-peak electrical driving voltage is the representative driving voltage from one of the elements in the therapy transducer.

During histotripsy treatment, the cavitational bubble clouds and their resulting damage in RBC phantoms were evaluated by optical images captured by the Phantom V210 high-speed camera. With an additional magnifying lens (Tominon, 1:4.5, f = 135 mm) used along with the camera, the resolution of these captured images was approximately 14–15 μm per pixel. The RBC phantoms were back lit with CW white light, thus the captured optical images would appear as "shadow graphs" in which the cavitational bubble clouds appeared dark black, the RBCs appeared gray, and the histotripsy-induced lesions appeared white. For every delivered histotripsy pulse, two images were acquired, one (bubble cloud image) at 10 μs after the arrival of the pulse, where the maximal spatial extent of the bubble cloud was observed, and the other (lesion image) at 500 ms after the arrival of the pulse, where only histotripsy-induced damage in the RBC phantom was observed.

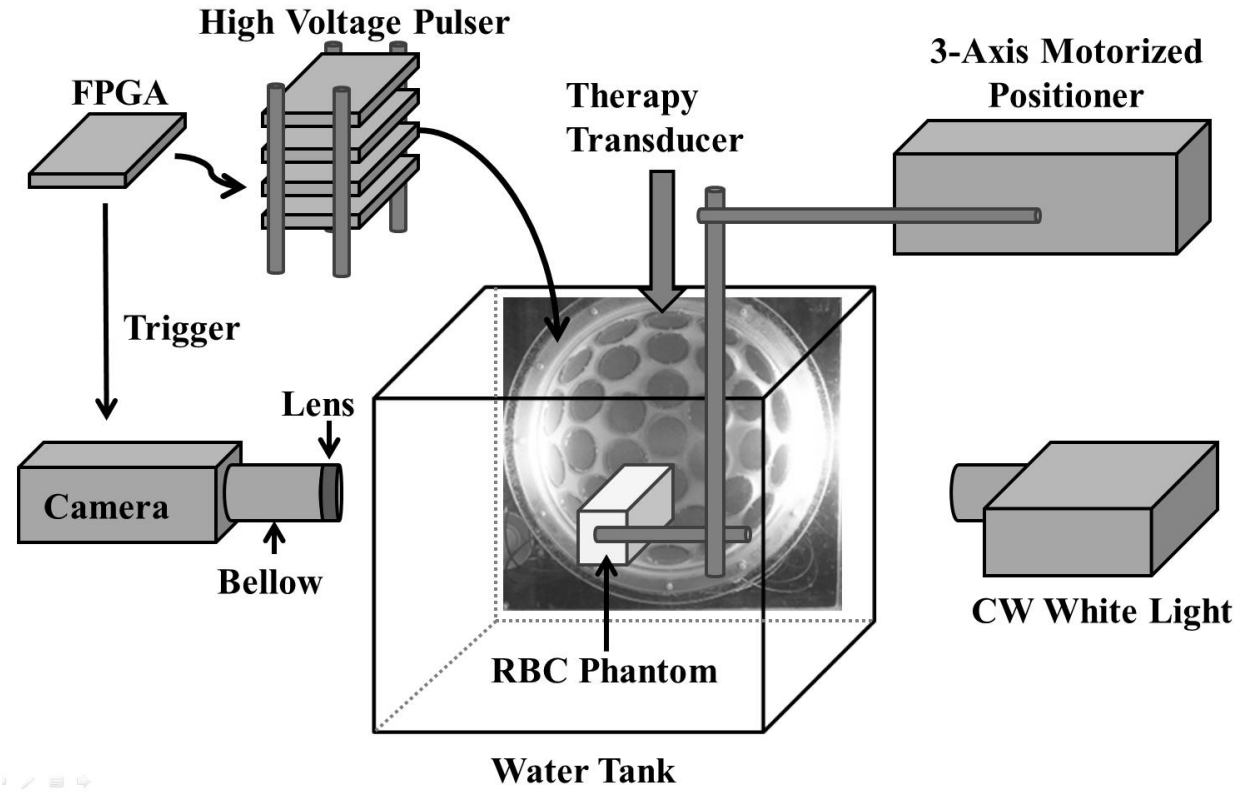

Figure 2.2 A schematic illustration of the experimental setup for RBC phantom experiments.

These optical images were then post-processed with MATLAB (R2011a, MathWorks, Natick, MA, USA) using a method similar to those described in previous papers [4, 7]. The lesion image was firstly converted to gray-scale, and then converted to a binary image using the threshold determined by the built-in function, *graythresh*, in MATLAB. The regions with brightness that were higher than the threshold would become "1 (white)" in the binary image and would be considered "damaged." In contrast, the regions with brightness less than the threshold would become "0 (black)" and be considered "intact." The white regions that were smaller than 4 pixels (correspond to regions less than 8 μm in radius) were considered to be noise and excluded from the damage zone. By counting the number of the white pixels in the binary image and converting it to actual size with the help of a pre-captured scale image, the area, length, and width of the lesion were determined. The bubble cloud images were quantified in a similar way, except the thresholds for binary image conversion were calculated based on the mean and standard deviation of the intensity of the bubble cloud, and the bubble cloud would be identified as "0 (black)." Then, the regions occupied by bubble clouds were overlaid after 500 applied histotripsy pulses, and the sizes in the lateral and axial dimensions of the overlaid bubble cloud occupied regions were further quantified.

For each lesion, the lesion development process was studied by investigating the relationship between the quantified lesion area and the number of the histotripsy pulses that had been applied. In order to compare this lesion development process for different pressure levels, the lesion sizes were further normalized to their maximal extents, which occurred after the application of 500 histotripsy pulses.

2.2.4 Treatment in ex vivo tissue

In order to validate the results in RBC phantoms, experiments were also performed in *ex vivo* canine renal and hepatic specimens as mentioned earlier. Canine renal and hepatic specimens that were embedded in agarose hydrogels were mounted on the 3-axis motorized positioner, and ultrasound B-mode imaging, instead of high speed photography, was used to monitor the histotripsy treatment. The ultrasound B-mode imaging was performed using a commercial ATL L12-5 linear ultrasound probe (Advanced Technology Laboratories, Inc., Bothell, WA, USA), along with a commercial ATL HDI 5000 ultrasound scanner.

Each intended treatment region was exposed to 500 histotripsy pulses at a PRF of 1 Hz, and a single-focal-point exposure was performed. Various pressure levels, listed in column 4 and 5 of Table 2.2, were applied to various regions of the specimens. In order to better identify the smaller lesions after treatment, two surface markers (10 mm separation) with higher pressure levels were generated on the surface of canine tissue specimen, along with two large lesions generated 6 mm right beneath the two surface markers. The small lesion was then generated in between these two large lesions and approximately 6 mm beneath the surface of the tissue specimen.

Table 2.2 Pressure levels used in the *ex vivo* canine tissue experiments of the microtripsy study

Peak-to-Peak Electrical Driving Voltage* (Volts)	Estimated Focal P– from Summation of Individual Elements (MPa)	Focal P– with Attenuation Correction (MPa)		
		Gel Holder	Kidney	Liver
894	34.8	30.7	28.5	29.3
995	36.9	32.6	30.2	31.0
1764	56.0	49.4	45.8	47.1

* The peak-to-peak electrical driving voltage is the representative driving voltage from one of the elements in the therapy transducer.

The lesions were then evaluated with both histological sections and ultrasound B-mode imaging. For histological section preparation, the treated canine specimens were fixed with 10%

phosphate buffered formalin (Fisher Scientific, Fair Lawn, NJ, USA) and sectioned into approximate 3mm-thick slices along the lateral-axial planes of the lesions using a regular kitchen knife and surgical scalpels. These slices were then further processed into 4µm-thick histological sections with 100 µm sectioning step size using a microtome and stained with hematoxylin and eosin (H&E). Visual inspection using bright field microscopy was performed to identify the section with maximal spatial extent of the damage among all sections for each sample. The maximal extents of the lesions in the lateral and axial directions were quantified based on the bright field microscopic images with the help of a pre-calibrated scale.

Ultrasound B-mode imaging allows us to evaluate the tissue treatment outcome in real-time, since the echogenicity in B-mode imaging of a treated region decreases as the degree of tissue fractionation increases [8, 9]. In this study, in order to resolve the lesions generated in the tissue specimens, especially the smaller ones generated with lower pressure level, a high-frequency ultrasound probe, RMV 707B (15-45 MHz, VisualSonics, Toronto, ON, Canada), along with a high-frequency ultrasound scanner, Vevo 770 (VisualSonics), was used to evaluate the lesion after treatment. Due to the short working distance of the ultrasound probe (focal length = 12.7mm), tissue specimens were taken out of the gel holder and agarose hydrogel was removed during the ultrasound evaluation process. The axial and lateral dimensions of the lesions were then measured based on the hypoechoic regions that appeared in the recorded B-mode images.

2.2.5 Lesion size estimation

The probability for the generation of a dense bubble cloud using a single, short pulse (≤ 2 cycles) is a function of the applied P–. This cavitation probability curve follows a sigmoid function [3], given by

$$P_{cav}\left(p_{-}\right)=\frac{1}{2}\left[1+erf\left(\frac{p_{-}-p_{t}}{\sqrt{2\sigma^{2}}}\right)\right], \qquad \text{.....Equation 2.1}$$

where *erf* is the error function, p_t is the pressure that gives a cavitation probability (P_{cav}) of 0.5, and σ is a variable that relates to the transition width in the cavitation probability curve, with ± σ giving the difference in pressure for cavitation probability from 0.15 to 0.85. The p_t's and σ's in water, gelatin gel, and high water content soft tissue were found to be within the range of 26 – 30 MPa (p_t) and 0.8 – 1.4 MPa (σ) [3].

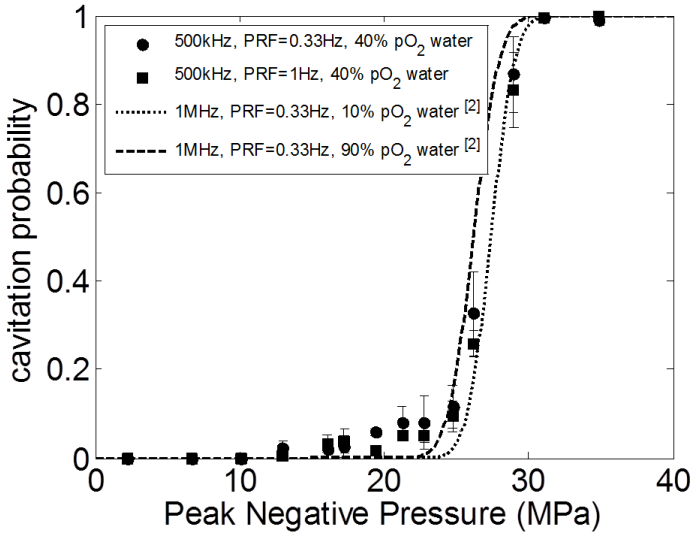

Figure 2.3 The probability for the generation of a dense bubble cloud using a single, short (≤ 2 cycles) pulse.

Figure 2.3 shows representative cavitation probability curves for producing dense bubble clouds in water plotted using the empirical values of p_t and σ determined in the previous study. Since the histotripsy pulses used in this study (500 kHz center frequency at PRF = 1 Hz) were different from those used in the previous study [3] (1 MHz center frquency at PRF = 0.33 Hz), the cavitation probabilities for the 500 kHz histotripsy pulses were also experimentally investigated and plotted in Figure 2.3. This investigation was performed using a passive cavitation detection (PCD) approach similar to the one described in [3]. A needle hydrohpone

(HNR-0500, ONDA Corp., Sunnyvale, CA, USA) was mounted orthogonal to the acoustic propagation path, and pointing to the focus of the transducer. For the signal analysis, the spectral energies within 600kHz–900kHz (1.5*f*) of the received scattered signals were firstly integrated (integrated power spectrum , S_{PCD}). For each applied pressure, the "expected" value for S_{PCD} without caivatiaon was then determined by extrapolating the S_{PCD} from really low pressures (1–5MPa) based on their focal intensities obtained from calibration measurements. If the measured S_{PCD} is greater than the expected value by five standard deviations, a dense bubble cloud is considered to have occurred during the pulse.

From this measurement and the results showing in Figure 2.3, it's reasonable to assume the cavitation thresholds are insensitive to both the center frequency of the transducer (at least between 500 kHz and 1 MHz) and the pulse repetition frequency (when PRF $\leq$ 1 Hz, with minimal cavitation memory effect [7] involved). The empirical values of p_t and σ listed in [3] for gel phantom and renal tissue were then used in the size estimation for the lesions generated in this study.

As illustrated in Figure 2.4, the expected lesion sizes in the lateral and axial dimensions were estimated by linearly scaling 1D beam profiles to the applied P–, then evaluating the regions on the scaled profiles where the P– valeus exceed a pressure threshold. This pressure threshold for lesion size estimation (P_{LSE}) was defined as the P– that gives a 50% probability of observing at least one dense bubble cloud generation event over the course of 500 delivered pulses.

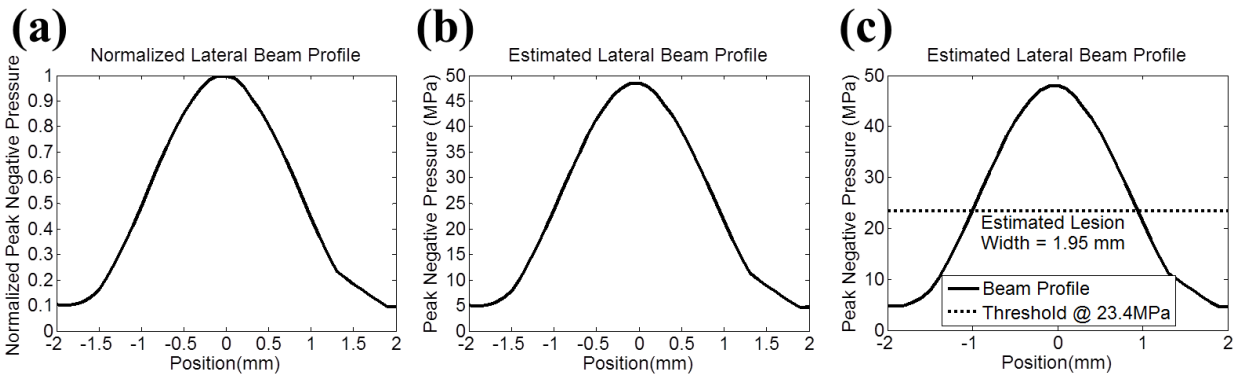

Figure 2.4. Illustration for the lesion size estimation using the lateral direction as an example. (a) A normalized lateral beam profile for P–. (b) The estimated lateral beam profile was obtained by multiplying the normalized beam lateral proflie with the estimated focal P–. (c) A threshold based on the cavitation probability curve was applied, and then the region above the threshold would be determined as damage zone.

Since Equation 2.1 only showed the cavitation probability curve for one "single" pulse (P_{cav}), we first used the binomial theorem to calculate the P_{cav} that would give a 50% probability of observing at least one dense bubble cloud generation per 500 pulses. This P_{cav} was calculated to be 0.0014. In 5% gelatin hydrogel, the P– that resulted in P_{cav} = 0.0014 was caluclated to be 23.4 MPa (P_{LSE}) using the empirical values of of p_t and σ listed in [3]. This P_{LSE} was used to estimate the size of the lesions that would be produced in RBC phantoms, since the acoustic properties of 1.5% agarose hydrogel are similar to those of 5% gelatin hydrogel. In renal tissue, the P_{LSE} was calculated to be 26.1 MPa, which was then used to estimate the size of the lesion that would be produced in the *ex vivo* canine kidney experiments.

2.3 Results

2.3.1 Experiments on RBC Phantoms

A total of 74 lesions were generated in RBC phantoms with nine pressure levels (listed in column 4 of Table 2.1), and each pressure level contained a total of nine lesions, with the

exception of two lesions for P– = 24.5 MPa. In the case of P– = 24.5 MPa, cavitational bubbles were not generated in response to every applied histotripsy pulse, and the shapes of the lesions were not well-confined and they varied between samples. Therefore, for P– = 24.5 MPa, only the lesion and bubble cloud images are shown in Figures 2.5 – 2.6, and no further quantitative analysis was performed. In the pressure levels from P– = 26.2 MPa to P– = 80.7 MPa, bubble clouds were consistently generated in every applied histotripsy pulse.

Figure 2.5 shows representative lesion and bubble clouds images at the 500th pulse, whereas Figure 2.6 demonstrates the lesion development process and shows representative lesion images for pulses 1, 10, 20, 50, 100, and 500. The images for P– = 27.3 MPa and 27.9 MPa did not vary significantly from the images for P– = 26.2 MPa, so they are not included. The pressure level of P– = 80.7 MPa resulted in an extreme outcome, and its result is shown separately in Figure 2.7. As can be seen in the Figure 2.5, the spatial extent of both the lesion and the bubble clouds increased as the applied pressure level increased. As shown in Figure 2.6, the lesion development process started from the center with minimal damage at the periphery. Then, the lesion gradually grew outwards as the number of applied pulses increased.

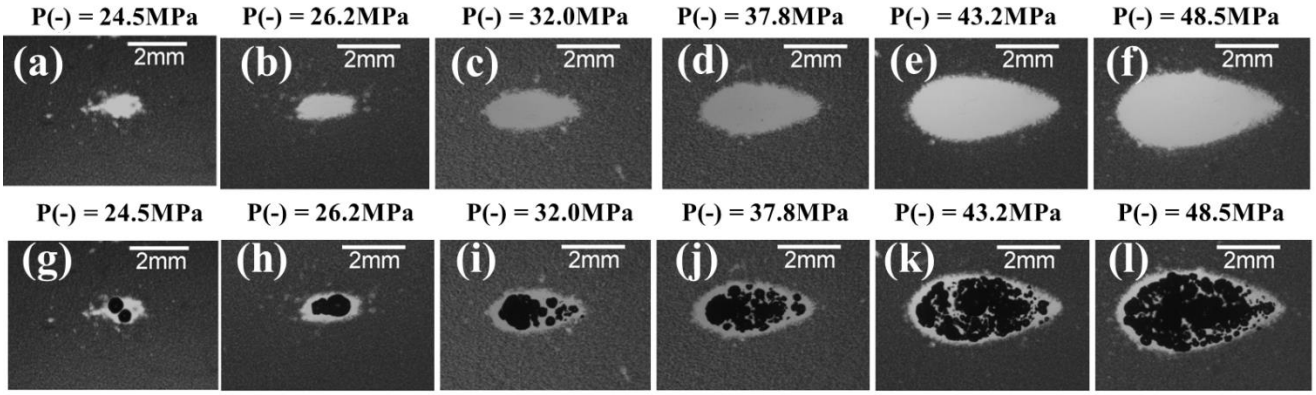

Figure 2.5 Representative lesion [(a)-(f)] and bubble cloud [(g)-(l)] images in RBC phantoms after 500 histotripsy pulses had being applied. These images were taken in the axial-lateral plane of the therapy transducer, and the histotripsy pulses propagated from the left to the right of the field.

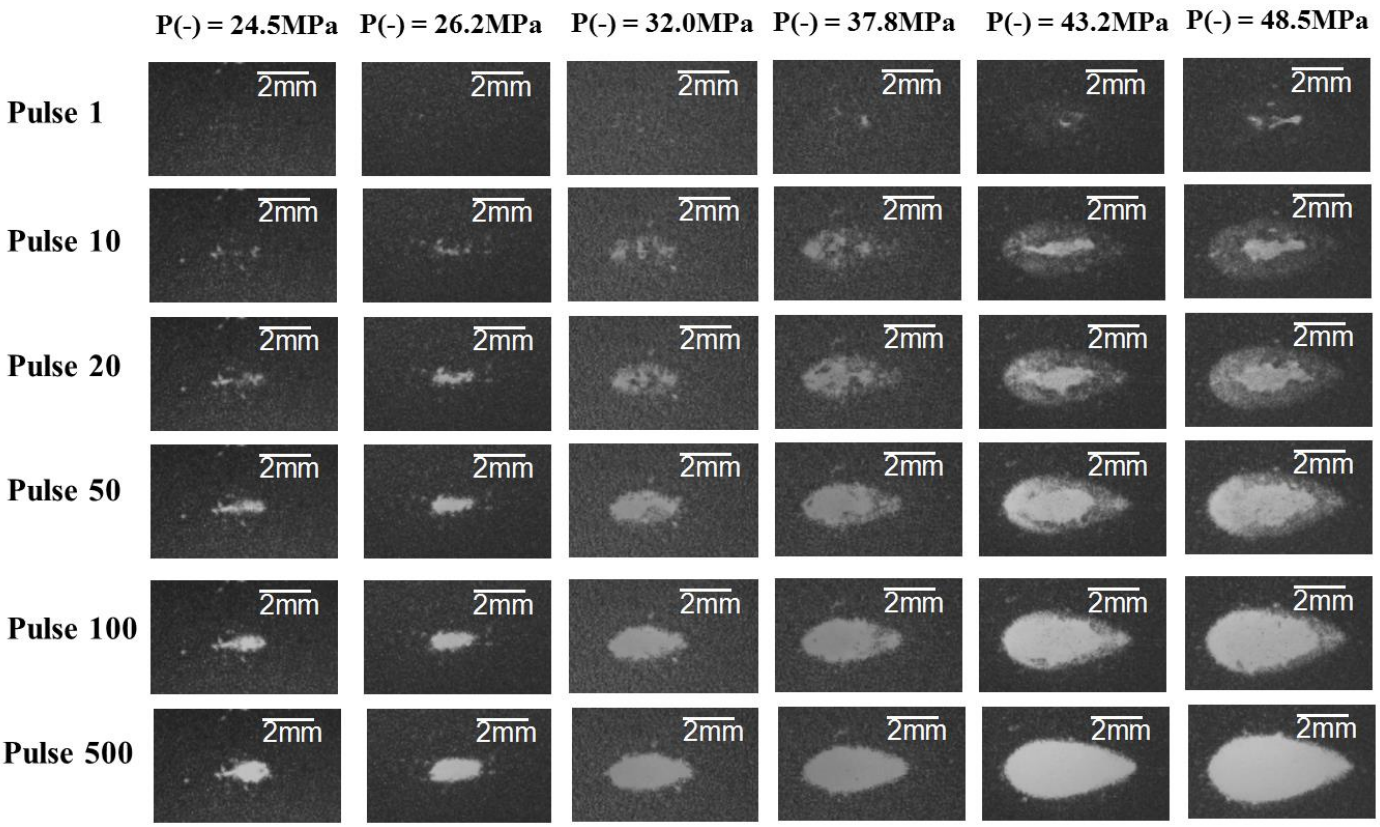

Figure 2.6 Representative lesion images in RBC phantoms demonstrating the lesion development processes. These images were taken in the axial-lateral plane of the therapy transducer, and the histotripsy pulses propagated from the left to the right of the field. The images for P– = 27.3 and 27.9 MPa are not included in this figure.

The extreme case came when the applied P– was increased to 80.7 MPa, where collateral damage along the axial direction was observed [Figure 2.7(a)]. Based on the 1D extrapolated beam profiles along axial [Figure 2.7(b)] and lateral [Figure 2.7(c)] directions at this pressure level, the applied pressure at the post-focal grating lobe in the axial direction was close to the threshold for lesion size estimation, P_{LSE}. This corresponded well with the finding in Figure 2.7(a), demonstrating that collateral damage occurred at the location where the grating lobe was close to that threshold.

The quantified sizes of the lesions and the overlaid bubble cloud occupied regions are plotted in Figures 2.8(a) and (b), along with their estimates based on the focal profile regions above the P_{LSE} threshold. As shown in the figure, the quantified sizes for both the lesions and overlaid bubble cloud occupied regions increased linearly with the applied P–. The sizes for lesions were slightly smaller than those for the overlaid bubble cloud occupied regions, and the differences between them were in the range of 0.5–1 mm. The average lesion widths ranged from 0.90 mm (P– = 26.2 MPa) to 3.91 mm (P– = 80.7 MPa), while the average lesion lengths ranged from 1.86 mm (P– = 26.2 MPa) to 7.57 mm (P– = 80.7 MPa). The estimates derived using P_{LSE} = 23.4 MPa corresponded well to the quantified lesion sizes in lower pressure levels. However, as the pressure level increased, higher discrepancy between the quantified lesion sizes and the estimates was observed in both lateral and axial directions. Note that there was a discontinuity in the estimated lesion size in axial direction around P– = 70 MPa. This was due to an inflection in the 1D axial beam profile at the bottom of the main lobe, as shown in Figure 2.7(b) (around –3 mm).

Figures 2.8(c) and 2.8(d) plot the quantitative results of the lesion development processes for various pressure levels. For clarity, the results from P– = 27.3, 27.9, and 43.2 MPa are not displayed (the results for P– = 27.3 and 27.9 MPa lie between P– = 26.2 and 32.0 MPa, and the result for 43.2 MPa lies between P– = 37.8 and 48.5 MPa). Figure 2.8(c) shows the quantified area of the lesion as a function of the number of applied histotripsy pulses. The normalized lesion area is shown in Figures 2.8(d), and as can be seen, the lesions that were created with lower pressure levels developed more slowly. The average numbers of histotripsy pulses required to reach 80% lesion development were 200 (P– = 26.2 MPa), 181 (P– = 27.3 MPa), 170 (P– = 27.9 MPa), 121 (P– = 32.0 MPa), 86 (P– = 37.8 MPa), 92 (P– = 43.2 MPa), 87 (P– = 48.5

MPa), and 115 (P– = 80.7 MPa). An exception occurred at P– = 80.7 MPa, where the lesion developed more slowly than P– = 48.5 MPa. This could be attributed to the sparsely distributed single bubbles generated in the prefocal grating lobe since the applied pressure there approached the P_{LSE} threshold.

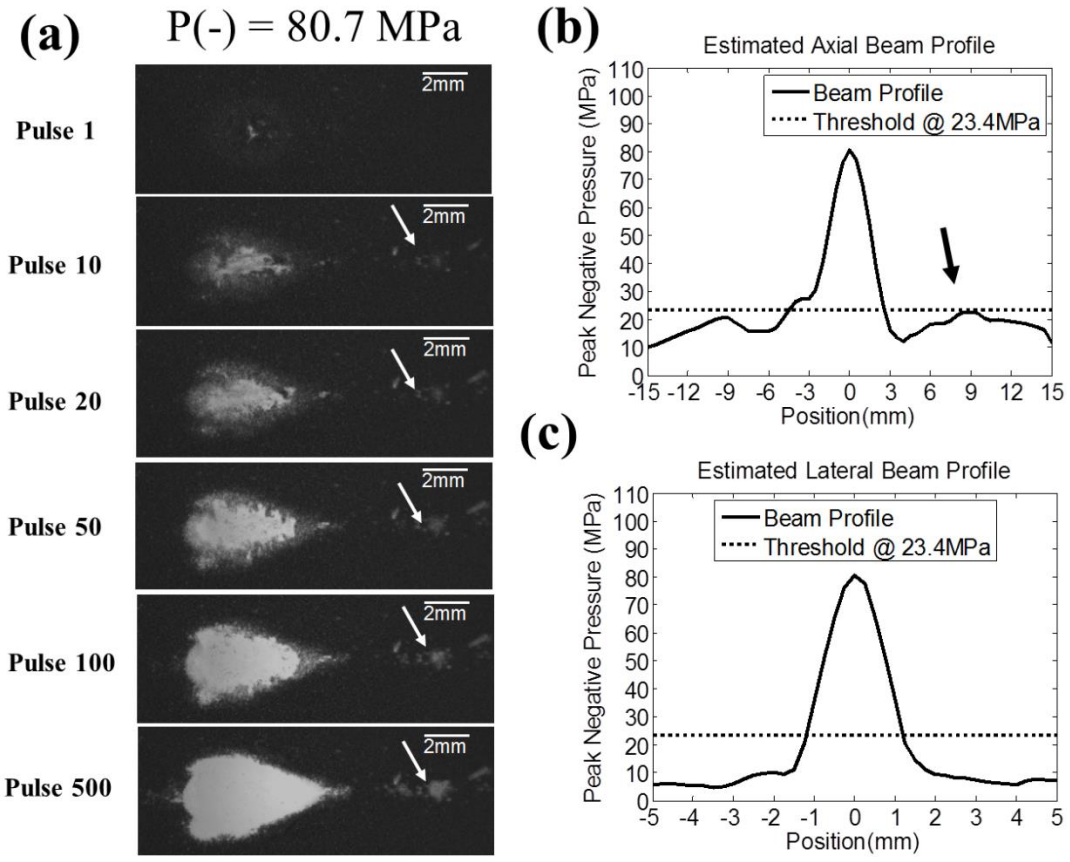

Figure 2.7 The extreme case where P– = 80.7 MPa was applied and one of the grating lobes (post-focal) in the axial direction was close to the threshold for lesion size estimation, P_{LSE}. (a) The representative lesion images in RBC phantom. These images were taken in the axial-lateral plane of the therapy transducer, and the histotripsy pulses propagated from the left to the right of the image. Collateral damage along axial direction was observed. (b) and (c) 1D estimated axial and lateral beam profiles are plotted as solid lines (–), whereas the dotted lines (…) represents the thresholds at P_{LSE} = 23.4 MPa

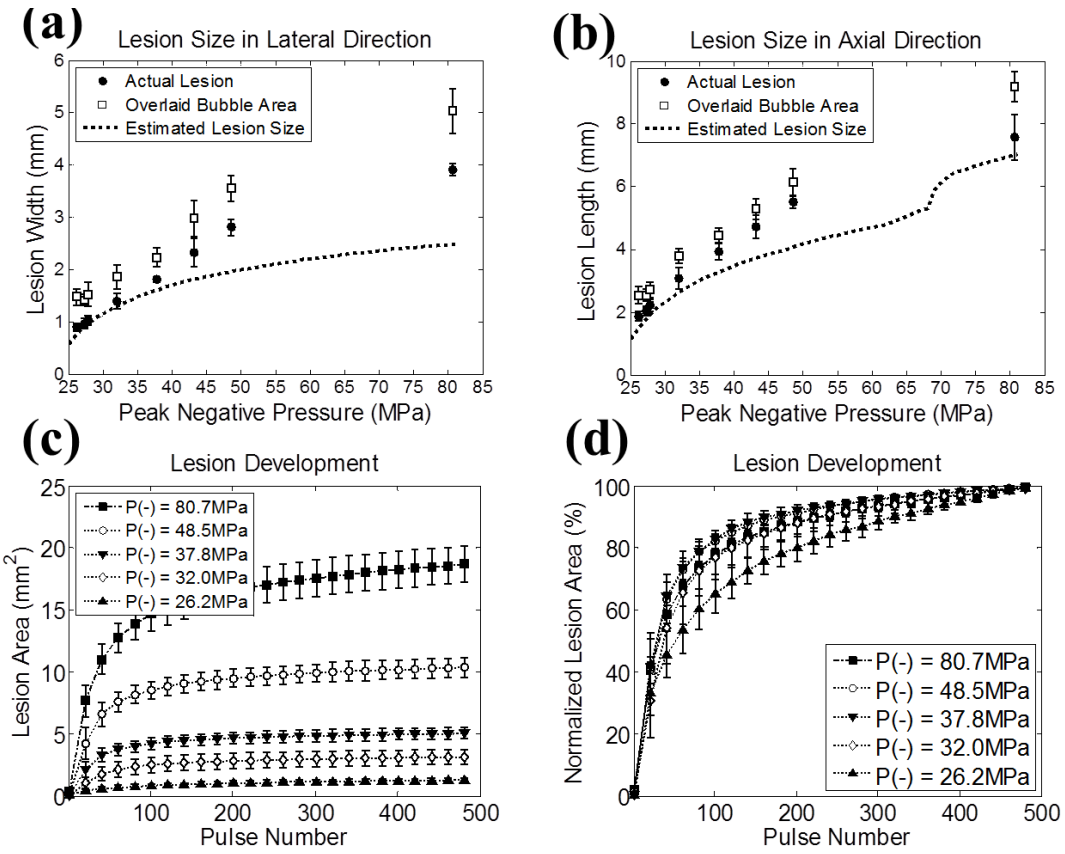

Figure 2.8 The quantified lesion sizes [(a) and (b)] and the lesion development processes [(c) and (d)] as a function of the applied P– in RBC phantom experiments. The sample sizes are nine (N = 9) for each pressure level, and the vertical error bars represent ± one standard deviation.

2.3.2 Ex Vivo Canine Kidney Experiments

The results for the experiments performed on the canine renal specimens are summarized as follows and shown in Figures 2.9 – 2.10. The sample sizes for the pressure levels of P– = 28.5, 30.2, and 45.8 MPa are 5, 5, and 7, respectively. Figure 2.9 shows representative B-mode images of the canine renal specimens after the application of 500 histotripsy pulses with these three pressure levels. As can be seen, the backscatter intensity of the tissue specimen decreased after treatment, resulting in hypoechoic regions on B-mode imaging. Moreover, these hypoechoic regions were larger when histotripsy at a higher pressure level was applied.

The representative histological sections are displayed in Figures 2.10 (a) – (c). As shown in the histological sections, the intended treatment regions had lost their normal architecture and contained only acellular granular debris, and a larger spatial extent of the lesion occurred when a higher pressure level was applied. The lesion sizes quantified from histological sections and B-mode images are shown in Figures 2.10(d) and (e), along with the estimates for the lesion sizes based on the regions that are above the P_{LSE} threshold. As can be seen from the figure, the lesion sizes quantified by the histological sections were similar as those quantified by B-mode images, with statistically significant difference occurring only at the applied pressure level of P– =30.2 MPa (p-values = 0.002 and 0.02 in the lateral and axial directions, respectively). In the lateral dimension of the lesion [Figure 2.10(d)], the quantified lesion widths lay close to the estimates, where the quantified lesion widths in histological sections were 0.22 (P– = 28.5 MPa), 0.31 (P– = 30.2 MPa), and 0.73 mm (P– = 45.8 MPa) larger than the estimates. In the axial dimension of the lesion [Figure 2.10(e)], the quantified lesion lengths lay close to the estimates, where the quantified lesion lengths in histological sections were 0.31 (P– = 28.5 MPa), 0.62 (P– = 30.2 MPa), and 0.65 mm (P– = 45.8 MPa) larger than the estimates.

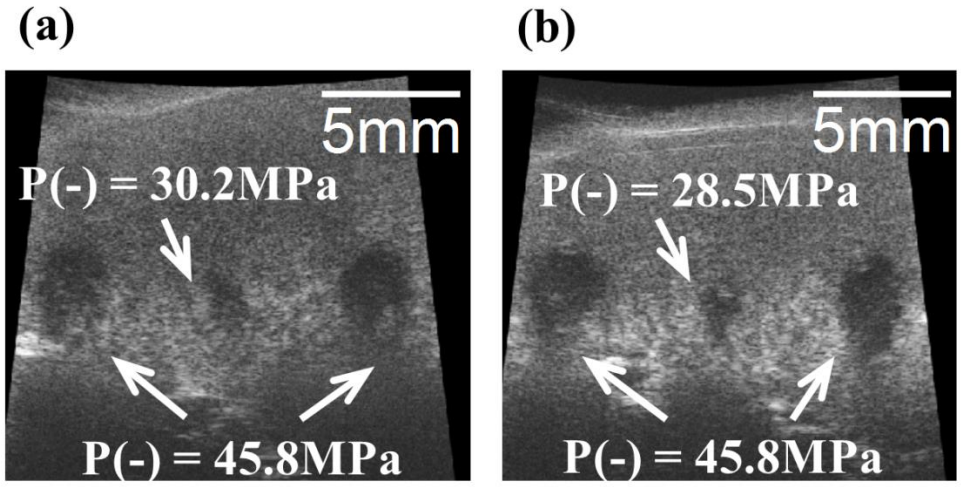

Figure 2.9 Representative B-mode images of canine renal specimens after the application of 500 histotripsy pulses. The histotripsy pulses propagated from the top to the bottom in the images.

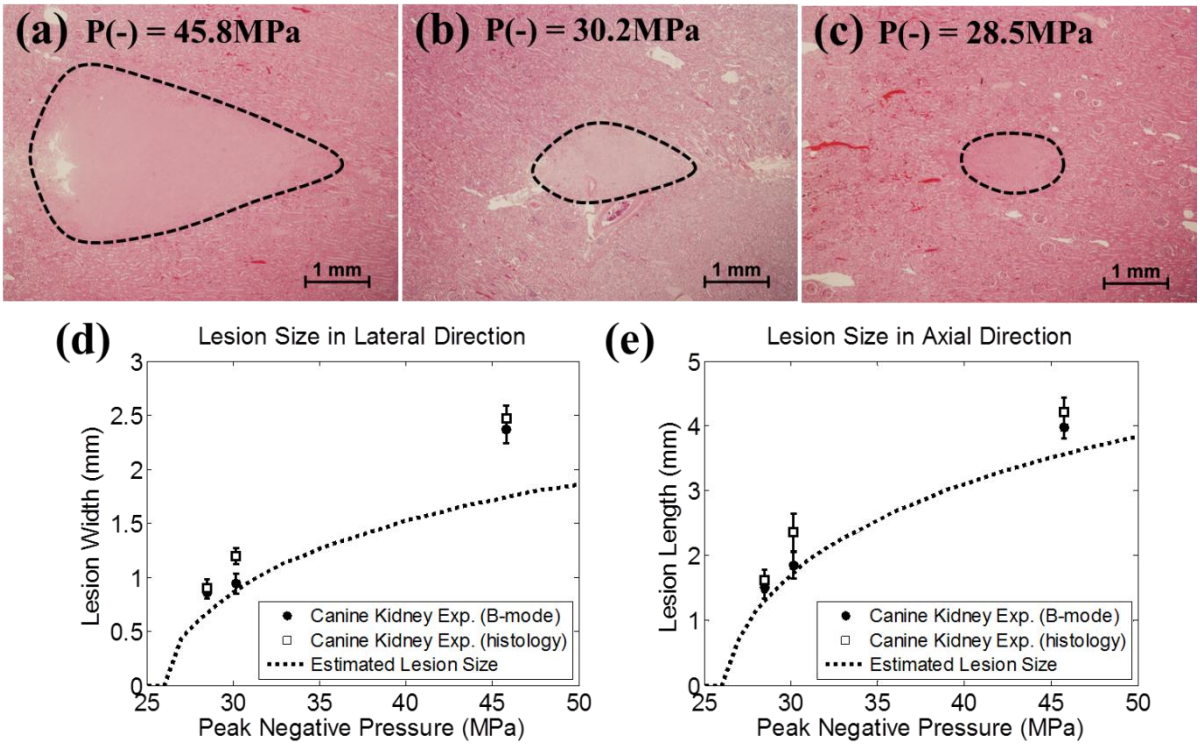

Figure 2.10 Representative histological sections in the canine renal tissue treatment, with the applied P– of 45.8 MPa (a), 30.2 MPa (b), and 28.5 MPa (c). The histological sections represent the axial-lateral planes of the lesions and the histotripsy pulses propagate from left to the right in the image. (d) and (e) plot the quantified lateral and axial dimensions of the lesions and their estimates based on the regions above the threshold.

2.3.3 Ex Vivo Canine Liver Experiments

The results for the experiments performed on the canine hepatic specimens are summarized as follows and shown in Figure 2.11 – 2.12, and the sample sizes for the pressure levels of P– = 29.3, 31.0, and 47.1 MPa are 5, 5, and 8, respectively. Figure 2.11 shows representative B-mode images of the hepatic specimens after the application of 500 histotripsy pulses. Similar as the result in Figure 2.9, hypoechoic regions occurred on B-mode images after histotripsy treatment, and these regions were larger when histotripsy at a higher pressure level was applied.

The representative histological sections are displayed in Figures 2.12(a) – (c). Similar to the case in renal specimens, the intended treatment regions had lost their normal architecture and contained only acellular granular debris, and a larger spatial extent of the lesion occurred when a higher pressure level was applied. The lesion sizes quantified from histological sections are shown in Figures 2.12(d) and (e), along with the lesions sizes of canine kidney for comparison. As can be seen, lesion sizes in both lateral and axial directions increased as the applied P– increased. Since the empirical values of p_t and σ for liver were not determined [3], no estimates were calculated in this case.

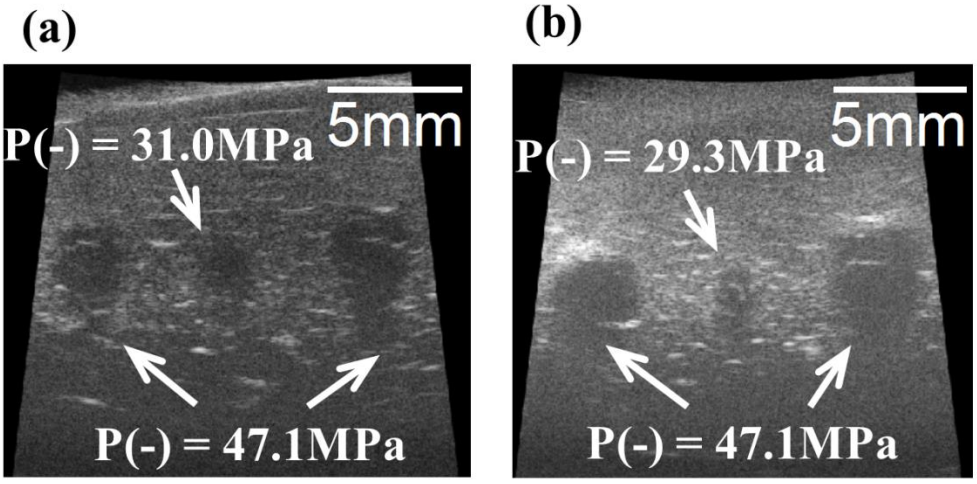

Figure 2.11 Representative B-mode images of canine hepatic specimens after the application of 500 histotripsy pulses. The histotripsy pulses propagated from the top to the bottom in the images.

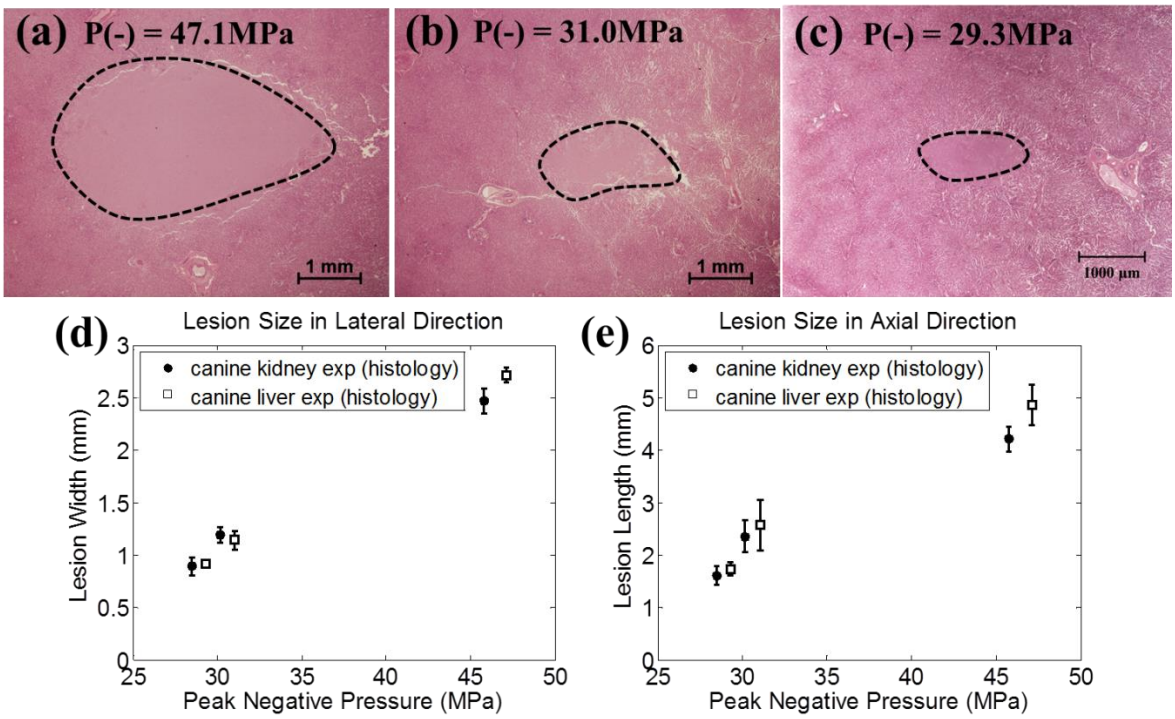

Figure 2.12 Representative histological sections in the canine hepatic tissue treatment, with the applied P– of 47.1 MPa (a), 31.0 MPa (b), and 29.3 MPa (c). The histological sections represent the axial-lateral planes of the lesions and the histotripsy pulses propagate from the left to the right in the images. The quantified lateral and axial dimensions of the lesions based on histological sections in hepatic tissue are plotted in (d) and (e), along with the lesion sizes in renal tissue.

2.4 Discussion

In this paper, precise and controlled lesions were generated by the intrinsic threshold mechanism in both RBC phantoms and *ex vivo* canine specimens. In comparison to the bubble clouds and lesions generated by the shock scattering mechanism shown in our previous studies [2, 4, 7, 10], those generated by the intrinsic threshold mechanism have two advantageous characteristics. First, the shape of the bubble cloud generated by the intrinsic threshold mechanism is well-confined and corresponds well to the shape of the transducer focal zone, whereas the shape of the bubble cloud generated by the shock scattering mechanism is variable and somewhat unpredictable. Because tissue fractionation is directly correlated to the activity of

the cavitational bubble cloud, the shape of the lesions produced by the intrinsic threshold mechanism is more predictable and has a better agreement to the shape of the transducer focal zone. Second, the bubble clouds generated by the intrinsic threshold mechanism are more uniform and consistent within the region exceeding the intrinsic threshold, whereas the bubble clouds generated by the shock scattering mechanism can be isolated to subvolumes of the focus due to complex scattering behavior. Therefore, the intrinsic threshold mechanism can potentially lead to more efficient and complete lesion development.

Moreover, using this intrinsic threshold mechanism, very small and controlled lesions can be generated by allowing only a small fraction of the focal region to exceed the cavitation threshold. In this paper, the smallest reproducible lesions generated in RBC phantoms, canine renal specimens, and canine hepatic specimens averaged 0.90 × 1.86 mm (lateral × axial), 0.89 × 1.61 mm, and 0.91 × 1.73 mm, respectively. These values were much smaller than the wavelength of the transducer (λ = ~3 mm for 500 kHz in agarose hydrogel, kidney, and liver). In the lateral direction, the lesion widths were even smaller than the diffraction limited –6dB focal pressure, $\lambda/2$. These results demonstrate that microscopic and precise lesions can be achieved using the intrinsic threshold mechanism, hence we call it "microtripsy."

The sizes of the lesions generated in this study corresponded well with the estimates based on how large the regions were above the P_{LSE} threshold. However, a discrepancy was observed at higher pressure level, as can be seen in Figures 2.8 and 2.10. In order to address this discrepancy, we studied whether the focal size of the transducer remained the same at higher pressure levels. A University of Washington (UW) study [11] has investigated the dependency of focal size on the applied pressure level in high intensity focused ultrasound (HIFU). Both their simulated and experimental results suggested that, when the applied acoustic pressure increased

to a certain level, the –6dB beamwidths based on P– increased while the beamwidths based on P+ decreased, due to nonlinear acoustic propagation. Hence, we investigated whether the focal size, for the therapy transducer used in this study, changed with the applied pressure level. Using the fiber optic probe hydrophone (FOPH), 1D beam profile scans along the lateral and axial directions were performed with 100µm step size, and the corresponding –6dB beamwidths based on P+ and P– are plotted in Figure 2.13. The –6dB beamwidths based on P– increased from 1.80 × 4.04 mm (lateral × axial) at P– = 8.7 MPa to 1.94 × 4.26 mm at P– = 18.4 MPa. The –6dB beamwidths based on P+ decreased from1.72 × 3.77 mm at P– = 8.7 MPa to 1.58 × 3.43 mm at P– = 18.4 MPa. These results follow a similar trend described in the study from UW [11], and is the likely explanation for the discrepancy between experimental lesion sizes and their estimates at higher pressure levels. Though we couldn't get a direct measurement of the beamwidths at the pressure levels used in this study (due to the unavoidable cavitation on the fiber tip in FOPH), this effect can be potentially modeled using a proper nonlinear simulation that we may investigate in the future. Other potential explanations for the discrepancy between actual lesion sizes and the estimates include 1) the maximal bubble expansion is dependent on the applied peak negative pressure, and the higher the applied P–, the larger the expansion, 2) the estimates of the lesion size were based on a simplified model rather than a sophisticated Monte-Carlo simulation demonstrated in [3].

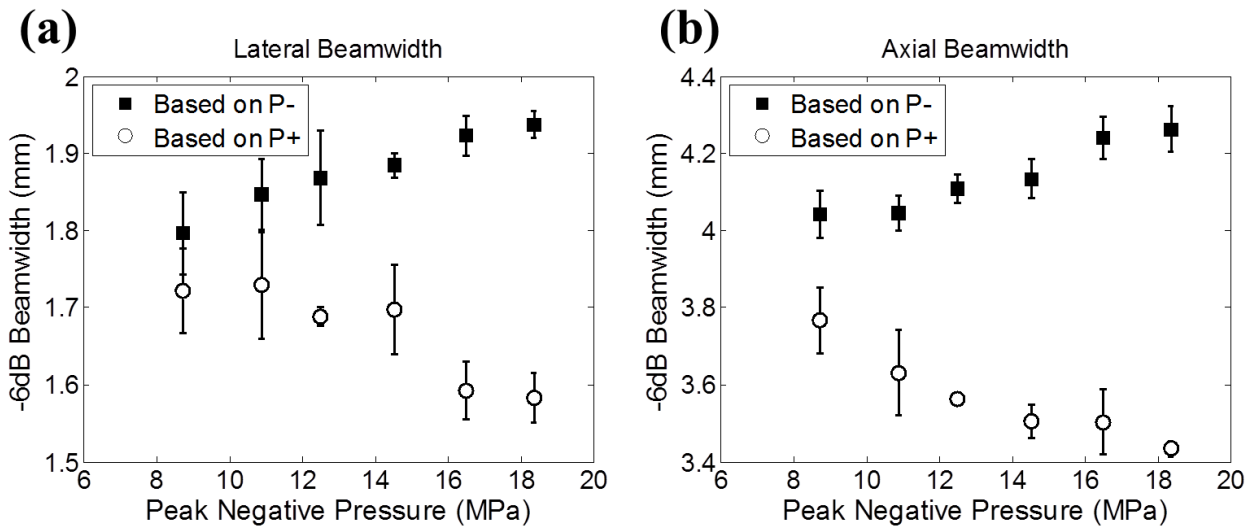

Figure 2.13 The calibrated –6dB beamwidths in lateral (a) and axial (b) directions for the 500 kHz therapy transducer as a function of the applied P–. The sample sizes for each point in (a) are three, and the samples sizes for each point in (b) are four.

The ellipsoidal-shape of the lesions generated at lower pressure levels correspond well with the shape of the focal regions above the P_{LSE} threshold. However, anomalous "tear-drop-shaped" lesions were observed at higher pressure levels and became pronounced at P– of 80.7 MPa, as shown in Figures 2.6 and 2.7(a). This "self-quenching" phenomenon may be due to a reduction in pulse intensity as it propagates through the significantly larger lesion resulting in a progressive reduction in the spatial extent of the supra-P_{LSE} zone and the size of the bubble cloud. The reduction in intensity could result from work done in generating the bubble cloud in the proximal zone of the lesion and some self-shadowing resulting from the rapidly expanding bubbles. Small residual bubbles from previous pulses would have a similar shadowing effect on subsequent pulses, particularly for larger lesions.

In the *ex vivo* canine tissue experiments, the lesions generated in hepatic tissue are slightly larger than the ones generated in renal tissue, at the same applied pressure levels (before attenuation correction). A majority of this difference can be attributed to the difference in

attenuation, since, as shown in Figures 2.12(d) and (e), the results from two different tissues are actually closer to each other and follow a similar trend after attenuation correction. Another potential explanation is that hepatic tissue has lower Young's modulus (YM) than renal tissue, since a previous study [12] shows that the tissue erosion process is faster in softer tissue (*i.e.* lower YM). Additionally, as shown in [3], the expansion of the bubble is larger in softer tissue, thus could potentially resulting in larger produced lesions.

Besides the lesions generated using the 500 kHz transducer in this study, an experiment was performed in a RBC phantom using a 3 MHz 7-element transducer to demonstrate the lesion production of the intrinsic threshold mechanism using a transducer of considerably higher frequency (3 MHz). The active elements in the transducer consisted of 20 mm diameter PZT-4 discs, each individually mounted to an acoustic lens with a geometric focus of 40 mm. The lateral and axial −6dB beamwidths of the 7-element transducer were measured to be 0.31 and 1.42 mm, respectively. The elements were driven by a high voltage pulser that gave an acoustic output of less than 2 cycles. Histotripsy pulses (100 pulses in total) were delivered at a PRF of 1 Hz for each intended treatment location. The smallest reproducible lesion for a single-focal-spot exposure has an average size of 0.16 × 0.27 mm (axial × lateral). Though this 3 MHz transducer did not share the same design as the 500 kHz transducer, the size of the smallest reproducible lesion was approximately 1/6 of that generated with the 500 kHz transducer. Figure 2.14 shows a lesion generated in a RBC phantom using this 3 MHz transducer, and this phantom was moved mechanically with a motorized positioning system during the treatment, creating an "M" character followed by a vertical "scale bar" and a string of characters showing "1 mm." This figure demonstrates the precision that can be achieved with "microtripsy" using a 3 MHz transducer.

This “microtripsy” technique based on the bubble clouds generated by the intrinsic threshold mechanism can be quite beneficial in the case where microscopic and well-defined tissue ablation is required. Especially, as shown in the study, very precise lesions could still be achieved using a low frequency transducer as long as we carefully allow only a small fraction of the focal zone to exceed the intrinsic threshold. Low frequency transducers would be favorable in applications that require long ultrasound penetration depth or where the intended targets have very attenuative overlying tissues, such as in transcranial brain therapy. Moreover, low-frequency single cycle (or close) pulses minimize phase aberration. In the future, we plan to apply supra-intrinsic threshold histotripsy (“microtripsy”) to very specific applications including transcranial and ophthalmologic procedures. We also plan to investigate different strategies on how to more precisely control the small fraction of the focal volume that exceeds the intrinsic threshold.

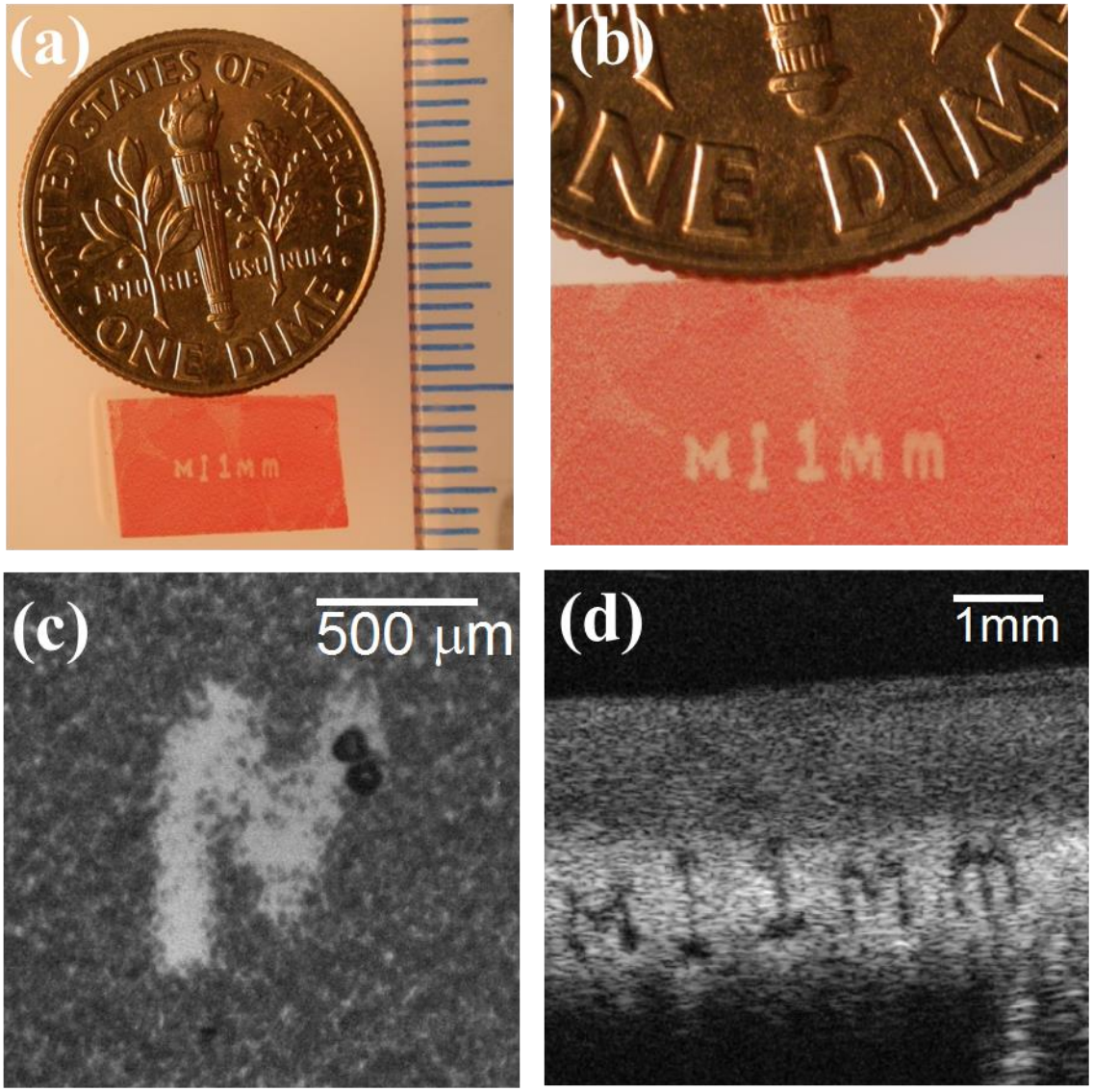

Figure 2.14 A representative lesion in RBC phantom generated by a 3 MHz transducer. (a) An overlook of the lesion along with a US dime coin and a ruler with millimeter tick marks. (b) A magnified view of the lesion (c) A high speed image showing the bubble cloud generated during treatment (d) An ultrasound B-mode image of the lesion after treatment.

2.5 Conclusion

In this chapter, the capability of histotripsy to generate precise, sub-wavelength lesions is demonstrated both in RBC phantoms and ex vivo canine tissues. This microtripsy procedure uses the highly repeatable and very sharp transition zone in cavitation probability inherent to bubble

cloud generation above the intrinsic threshold. Lesion sizes in both axial and lateral directions can be increased by increasing the applied peak negative pressure. These lesion sizes corresponded well to the dimensions of the focal beam profile estimated to be beyond the intrinsic cavitation threshold, although there was a discrepancy at higher applied pressure levels ($P- > 35$ MPa), most likely accounted for by an increase in the size of the peak negative pressure focal zone as a result of nonlinear propagation processes. This microtripsy technique can be significantly useful in the clinical applications where precise, microscopic tissue ablation is required, particularly where low frequencies are indicated, while still maintaining small precise sub-wavelength lesions.

2.6 References

[1] K.-W. Lin, Y. Kim, A. D. Maxwell, T.-Y. Wang, T. L. Hall, Z. Xu, J. B. Fowlkes, and C. A. Cain, "Histotripsy beyond the Intrinsic Cavitation Threshold using Very Short Ultrasound Pulses: Microtripsy," *IEEE Trans Ultrason Ferroelectr Freq Control,* vol. 61, pp. 251-265, 2014.

[2] A. D. Maxwell, T. Y. Wang, C. A. Cain, J. B. Fowlkes, O. A. Sapozhnikov, M. R. Bailey, and Z. Xu, "Cavitation clouds created by shock scattering from bubbles during histotripsy," *J Acoust Soc Am,* vol. 130, pp. 1888-98, Oct 2011.

[3] A. D. Maxwell, C. A. Cain, T. L. Hall, J. B. Fowlkes, and Z. Xu, "Probability of Cavitation for Single Ultrasound Pulses Applied to Tissues and Tissue-Mimicking Materials," *Ultrasound Med Biol,* vol. 39, pp. 449-465, 2013.

[4] A. D. Maxwell, T.-Y. Wang, L. Yuan, A. P. Duryea, Z. Xu, and C. A. Cain, "A Tissue Phantom for Visualization and Measurement of Ultrasound-Induced Cavitation Damage," *Ultrasound in Medicine & Biology,* vol. 36, pp. 2132-2143, 2010.

[5] J. E. Parsons, C. A. Cain, and J. B. Fowlkes, "Cost-effective assembly of a basic fiber-optic hydrophone for measurement of high-amplitude therapeutic ultrasound fields," *J Acoust Soc Am,* vol. 119, pp. 1432-40, Mar 2006.

[6] T. D. Mast, "Empirical relationships between acoustic parameters in human soft tissues," *Acoustics Research Letters Online,* vol. 1, pp. 37-42, 2000.

[7] T.-Y. Wang, Z. Xu, T. L. Hall, J. B. Fowlkes, and C. A. Cain, "An Efficient Treatment Strategy for Histotripsy by Removing Cavitation Memory," *Ultrasound in Medicine & Biology*, vol. 38, pp. 753-766, 2012.

[8] T. L. Hall, J. B. Fowlkes, and C. A. Cain, "A real-time measure of cavitation induced tissue disruption by ultrasound imaging backscatter reduction," *IEEE Trans Ultrason Ferroelectr Freq Control*, vol. 54, pp. 569-75, Mar 2007.

[9] T. Y. Wang, Z. Xu, F. Winterroth, T. L. Hall, J. B. Fowlkes, E. D. Rothman, W. W. Roberts, and C. A. Cain, "Quantitative ultrasound backscatter for pulsed cavitational ultrasound therapy- histotripsy," *IEEE Trans Ultrason Ferroelectr Freq Control*, vol. 56, pp. 995-1005, May 2009.

[10] Z. Xu, M. Raghavan, T. L. Hall, C.-W. Chang, M. A. Mycek, J. B. Fowlkes, and C. A. Cain, "High Speed Imaging of Bubble Clouds Generated in Pulsed Ultrasound Cavitational Therapy - Histotripsy," *Ultrasonics, Ferroelectrics and Frequency Control, IEEE Transactions on*, vol. 54, pp. 2091-2101, 2007.

[11] M. S. Canney, M. R. Bailey, L. A. Crum, V. A. Khokhlova, and O. A. Sapozhnikov, "Acoustic characterization of high intensity focused ultrasound fields: A combined measurement and modeling approach," *The Journal of the Acoustical Society of America*, vol. 124, pp. 2406-2420, 2008.

[12] M. Cooper, X. Zhen, E. D. Rothman, A. M. Levin, A. P. Advincula, J. B. Fowlkes, and C. A. Cain, "Controlled ultrasound tissue erosion: the effects of tissue type, exposure parameters and the role of dynamic microbubble activity," in *Ultrasonics Symposium, 2004 IEEE*, 2004, pp. 1808-1811 Vol.3.

Chapter 3
Dual-Beam Histotripsy: A Low-Frequency Pump Enabling a High-Frequency Probe for Precise Lesion Formation

A majority component of this chapter has been published in *IEEE Transactions on Ultrasonics, Ferroelectric, and Frequency Control* © 2014 IEEE. Reprinted, with permission, from [1].

3.1 Introduction

As shown in the previous chapter, using the intrinsic threshold mechanism, the size of the smallest reproducible lesion becomes smaller with higher frequency histotripsy pulses, which is beneficial in applications that require precise lesion generation. However, higher frequency pulses are more susceptible to attenuation and aberration, rendering problematical treatments at a longer penetration depth or through a highly aberrative medium, e.g., transcranial procedures. In this chapter, we propose and study a strategic application of histotripsy pulses to address this issue: a low-frequency pump pulse (< 2 cycles) is applied together with a high-frequency probe pulse (< 2 cycles) wherein their peak negative pressures constructively interfere to exceed the intrinsic threshold. The low-frequency pump, which is more resistant to attenuation and aberration, can raise the P– level for a region of interest (ROI); while the high-frequency probe (perhaps an imaging transducer), which provides more precision, can pin-point a targeted location within the ROI and raise the P– above the intrinsic threshold. We call this approach "dual-beam histotripsy."

Previous studies from Umemura *et al* [2, 3] showed that the superimposition of the 2nd-harmonic onto the fundamental frequency can enhance cavitation activity. More specifically, Umemura *et al* [2] demonstrated that the superimposition of the 2nd-harmonic onto the fundamental frequency with two confocal transducers can enhance sonodynamic therapy wherein cavitation enhances the therapeutic effect of certain agents administered prior to treatment. Yoshizawa *et al* [3] studied the bubble cloud generation near a rigid wall by 2nd-harmonic superimposed ultrasound, and their results showed that the negative pressure emphasized wave had an advantage in cavitation inception over the positive pressure emphasized wave.

Several other studies have also investigated waveform manipulation methods to either enhance or reduce cavitation activity. The study conducted by Chapelon *et al* [4] showed that the sonoluminescence activity (using luminol as a cavitation detector) generated with pseudorandom phase-modulated signals was significantly lower than that generated with continuous-wave (CW), single-frequency ultrasound. Sokka *et al* [5] investigated the effect of dual-frequency driving waveforms on injected microbubbles both theoretically and experimentally, and the results showed that their developed dual-frequency methods could preferentially lower the cavitation threshold at the focus relative to the rest of the field. Matsumoto *et al* [6] and Ikeda *et al* [7, 8] utilized dual frequency excitation for cloud cavitation control in renal stone comminution, wherein the bubble cloud was firstly created by a high-frequency pulse and then forced into a violent collapse with a succeeding low-frequency pulse for fragmentation of kidney stones. Liu and Hsieh [9] generated dual-frequency ultrasound waves using a single-element transducer and demonstrated its capability in enhancing acoustic cavitation. Hasanzadeh *et al* [10] investigated the enhancement of acoustic cavitation generated on aluminum foil using dual-frequency sonication with transducers of several different frequencies.

The dual-beam histotripsy approach proposed in this paper is mechanistically different from the previous studies [2-10]. In the previous studies, longer pulses (>50 μs in [6-8], 125μs in [3], and CW for the rest) were used and the enhancement (or suppression) of acoustic cavitation was accomplished by pseudo-random phase-modulation, harmonic superimposition, and high frequency pulse followed by low frequency pulse, not necessarily increasing the applied pressure level using the 2^{nd} frequency component. In contrast, dual-beam histotripsy uses pulses less than two cycles, and the arrival times of the pump and probe were adjusted to enhance P– constructive interference. Additionally, the cavitation probability was enhanced in the previous studies by microbubble seeding or reflection from a rigid interface (except for [4]), whereas dual-beam histotripsy generates a dense bubble cloud without any pre-existing microbubbles or special interfaces.

In this chapter, the feasibility of dual-beam histotripsy was investigated using red-blood-cell (RBC) tissue-mimicking phantoms and ex vivo porcine livers. More specifically, a 20-element dual-frequency array transducer, in which 500-kHz (pump) and 3-MHz (probe) elements were confocally aligned, was used to generate dual-beam histotripsy pulses at a pulse repetition frequency (PRF) of 1 Hz. Three experimental sets were performed in RBC phantoms wherein: 1) the arrival times of 500-kHz and 3-MHz pulses (both below the intrinsic threshold) were varied to investigate whether lesions could only be generated when combined P− values exceeded the intrinsic threshold, 2) the relative amplitude of 500-kHz and 3-MHz pulses was varied to study the size of the smallest reproducible lesion with different proportions of pump and probe, and 3) the relative propagation direction between 500-kHz and 3-MHz pulses was varied to determine the effect on the shape and size of the produced lesions. Finally, selected dual-beam histotripsy pulses were tested in ex vivo porcine hepatic specimens to validate the results in real tissue.

3.2 Methods

3.2.1 Sample Preparation

Experiments were performed on red-blood-cell (RBC) tissue-mimicking phantoms and *ex vivo* porcine livers to investigate the treatment effect for the dual-beam histotripsy pulses. The procedures described in this study were approved by the University of Michigan's Committee on Use and Care of Animals.

The RBC tissue-mimicking phantoms can be used for the visualization and quantification of cavitation-induced damage [11]. In this study, fresh canine blood was obtained from adult research canine subjects in an unrelated study. An anticoagulant solution of citrate-phosphate-dextrose (CPD) (C7165, Sigma-Aldrich, St. Louis, MO, USA) was added to the blood with a CPD-to-blood ratio of 1:9 (v:v), and the blood was kept at 4℃ and used within 3 weeks. A low-melting-point agarose powder (AG-SP, LabScientific, Livingston, NJ, USA) was used along with the canine blood to prepare RBC phantoms following the protocol described in [11]. In this study, since the expected lesions are very small (in the range of 200 - 500 μm), the central layer preparation differed slightly from the protocol. Instead of lying flat when the central layer was solidifying, the gel holder was mounted vertically such that the agarose-saline-RBC mixture trickled down the previous agarose-only casting while solidifying into a very thin central layer (~ 60 – 100 μm) [Figure 3.1(a)]. Additionally, in order to provide sufficient image contrast between treated and untreated regions, the ratio of RBCs to agarose-saline mixture was increased from 5:95 to 33:67 (v:v). The gel holder for RBC phantoms is shown in Figure 3.1(b).

Experiments were also performed in *ex vivo* porcine livers to validate the results observed in the RBC phantoms. The excised porcine livers were collected from a local abattoir, kept in 0.9% saline at 4℃, and used within 36 hours. Before the experiments, the livers were sectioned

into small specimens (~2 × 2 × 2 cm), submerged in degassed 0.9% saline and placed in a chamber under partial vacuum (~33 kPa, absolute) at room temperature for 1 – 2 hours. The specimens were then embedded in a 1% agarose hydrogel that consisted of low-melting-point agarose and 0.9% saline. The gel holder for liver experiments is shown in Figure 3.1(c).

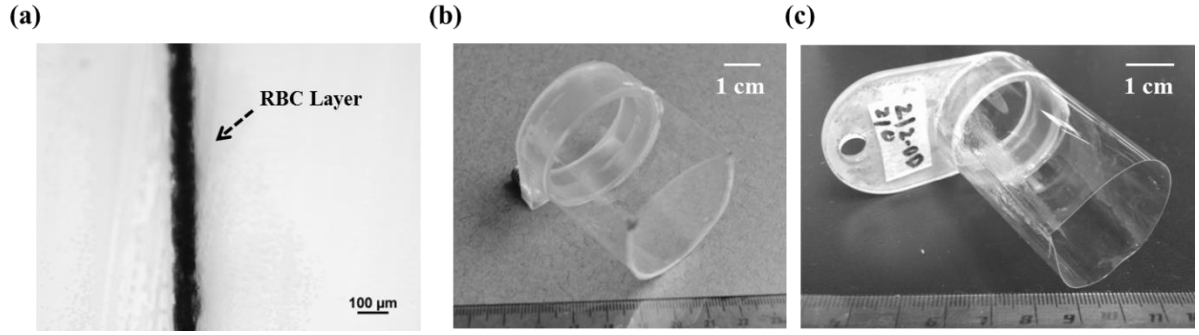

Figure 3.1 (a) A bright field microscope image with a 10× objective showing the cross-section of a representative RBC phantom. (b) A picture of a representative gel holder for RBC phantoms. (c) A picture of a representative holder for agarose-embedded porcine hepatic specimens.

3.2.2 Histotripsy Pulse Generation and Calibration

Histotripsy pulses were generated by a custom, 20-element, dual-frequency array transducer (Figure 3.2) that consisted of twelve 500 kHz elements and eight 3 MHz elements. Each 500 kHz element consisted of two 1 MHz, 20-mm-diameter piezoceramic discs (PZ36, Ferroperm, Kvistgaard, Denmark) stacked together with epoxy, while each 3 MHz element consisted of a single 3 MHz, 20-mm-diameter piezoceramic disc (SM111, Steiner and Martins, Miami, FL, USA). Both 500 kHz and 3 MHz elements were individually mounted to acoustic lenses with a geometric focus of 40 mm. The elements were confocally aligned and arranged in the following order: 1) the very bottom of the array transducer – one 3 MHz element, 2) 1st ring from the bottom – six 500 kHz elements with a 37-degree tilt angle, 3) 2nd ring from the bottom – six 500 kHz elements with a 64-degree tilt angle, 4) 3rd ring from the bottom – six 3 MHz elements with a 85-degree tilt angle, and 5) on top of the array transducer – one 3MHz element

that was attached to a supporting frame and had an opposite propagation direction, which was from top to bottom. This top element was used only during the study that investigated the effect of different propagation directions of the 3 MHz element relative to the 500 kHz component. Note that the 20-element dual frequency transducer actually had four additional elements above its third ring with 103-degree tilt angle [can be seen in Figures 3.2(a) and (b)], but they were never used in this study. In drawings of the cross-sections [Figures 3.2(c) and 2(d)], and following figures and calibration measurements, these four elements were excluded.

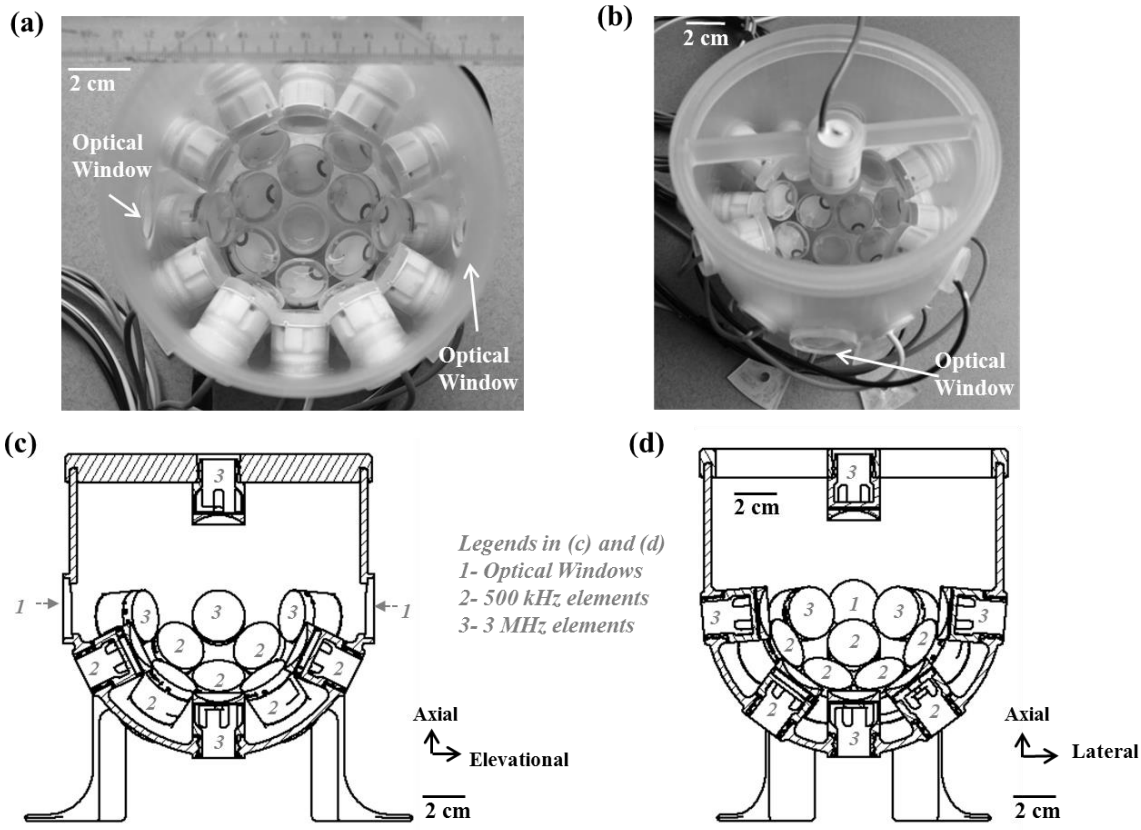

Figure 3.2 20-element dual-frequency array transducer (a) A top-down view of the transducer without the top element and adapting frame. (b) An angled view of the transducer with the top element and adapting frame. (c) A cross-sectional drawing of the transducer in the axial-elevational plane with the top element and adapting frame. (d) A cross-sectional drawing of the transducer in the axial-lateral plane with the top element and adapting frame.

Additionally, this dual-frequency array transducer also had two diametrically opposed optical windows, approximately at the same height as the 3rd ring and facing each other, for the visualization of the cavitating bubble clouds and lesions generated in RBC phantoms. To generate short therapy pulses, a custom high voltage pulser developed in-house was used to drive the transducer. The pulser was connected to a field-programmable gated array (FPGA) development board (Altera DE1, Terasic Technology, Dover, DE, USA) specifically programmed for histotripsy therapy pulsing. This setup allowed the transducer to output short pulses consisting of less than two cycles. The transducer was filled with degassed water (~50% of normal PO_2) during experiments, and the gas saturation was measured by a commercial dissolved oxygen meter (YSI5000, YSI Inc., Yellow Springs, OH, USA).

A fiber-optic probe hydrophone (FOPH) [12] was used to measure the acoustic output pressure of the dual-frequency transducer. Figure 3.3 shows the calibration results of the 500 kHz component (a total of 12 elements) in the free-field, including a representative focal pressure waveform before inducing cavitation on the FOPH [Figure 3.3(a)], total focal P– as a function of peak-to-peak driving voltage [Figure 3.3(b)], and one-dimensional (1D) beam profiles in the axial [Figure 3.3(c)], lateral [Figure 3.3(d)], and elevational [Figure 3.3(e)] directions. Phase correction was performed to compensate for any misalignment of the 500 kHz elements. Pressure levels after inducing cavitation on the FOPH were estimated by the summation of the output focal P– values from individual elements. In a previous study [13], this estimate had a good agreement with the P– measured directly in a higher cavitation threshold medium, 1,3 butanediol. The 6 dB beam-widths (calculated based on P–) were measured to be 4.89 (axial), 1.74 (lateral) and 1.77 mm (elevational).

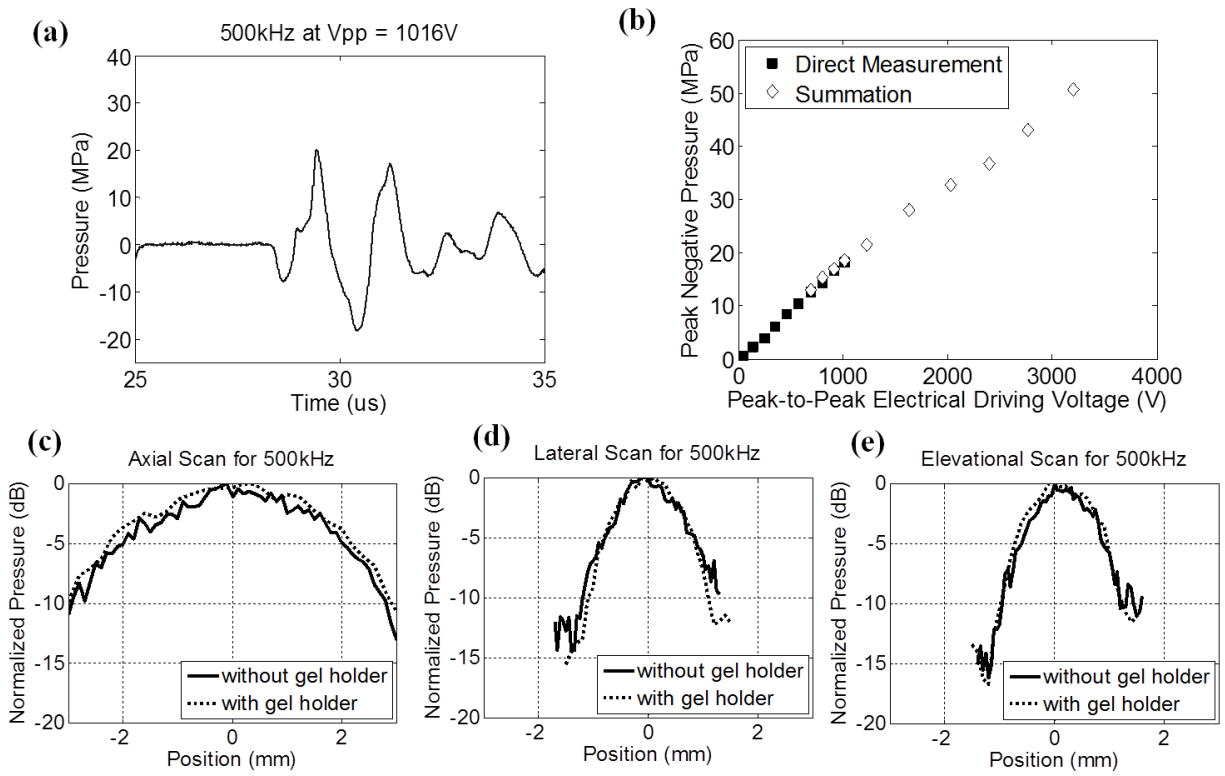

Figure 3.3 Calibration results of the 500 kHz component (a total of 12 elements) in the dual-frequency array transducer. (a) A representative acoustic waveform at the focus in the free-field. (b) Peak negative pressure as a function of peak-to-peak driving voltage. 1D beam profiles in the axial (c), lateral (d), and elevational (e) direction.

Figure 3.4 shows the calibration results of the 3 MHz component (a total of 7 elements without the top element) in the free-field, including a representative focal pressure waveform before inducing cavitation on the FOPH [Figure 3.4(a)], total focal P– as a function of DC supply voltage to the high-voltage pulser [Figure 3.4(b)], and one-dimensional (1D) beam profiles in the axial [Figure 3.4(c)], lateral [Figure 3.4(d)], and elevational [Figure 3.4(e)] directions. Phase correction was performed to compensate for any misalignment of the 3 MHz elements. The 6 dB beam-widths (calculated based on P–) were measured to be 1.42 (axial), 0.31 (lateral) and 0.31 (elevational) mm. Figure 3.4(f) shows a representative focal pressure waveform from the bottom element at the pressure level used in the 3rd experimental set that varied the relative propagation

directions between 500 kHz and 3 MHz components. Note that the waveforms in Figures 3.3(a) and 3.4(a) were not as nonlinear as the ones shown in our previous works [14-20], this was likely due to 1) this array transducer having a lower f-number (approximately 0.56 for 500 kHz components and 0.50 for 3MHz components), and 2) each element having an individual focusing lens such that acoustic beams from adjacent elements did not overlap significantly until they reached the common geometric focus.

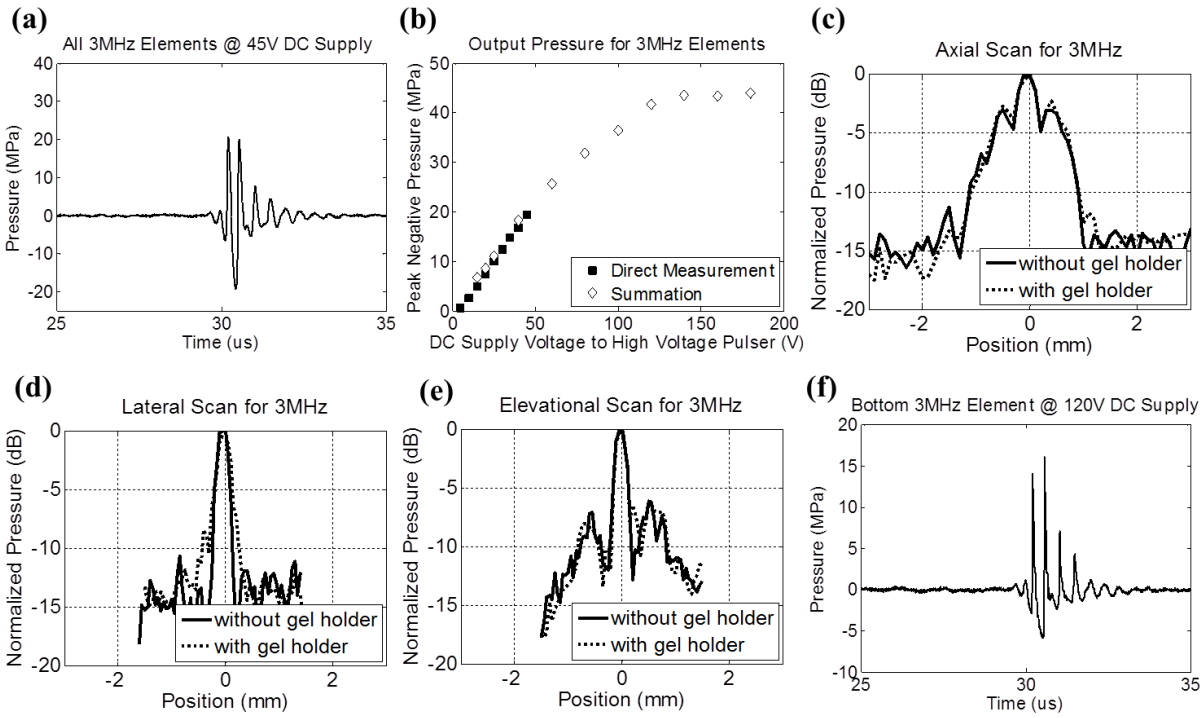

Figure 3.4 Calibration results of the 3MHz component. (a) A representative free-field focal acoustic waveform. (b) Peak negative pressure as a function of the DC supply voltage to the high voltage pulser. 1D beam profiles (with all 7 elements firing) in the axial (c), lateral (d), and elevational (e) directions. (f) A representative free-field focal acoustic waveform of an individual element (the bottom element) at the pressure level used in the 3rd experimental set.

Cylindrical, custom-made, plastic gel holders (4 cm in diameter and 8 cm in height) with thin polycarbonate membranes (254 µm thick) glued on their sides, as shown in Figure 3.1(b), were used to hold the RBC phantoms. Based on the calibration with a representative plastic gel

holder in place, the P– values were attenuated by 8.2% (500 kHz) and 9.1% (3 MHz); however, the 1D beam profiles did not change significantly, as shown in Figures 3.3 (c) – (e) and 3.4(c) – (e). Note that the attenuations for 500 kHz and 3 MHz did not scale with the frequency, and this was likely due to the difference in their incidental angles on the gel holder (3MHz elements had almost normal incidence while 500 kHz elements had oblique incidence). In the *ex vivo* porcine liver experiment, another type of cylindrical gel holder [Figure 3.1(c), 3cm in diameter and 6 cm in height] with thinner polycarbonate membranes (127 μm thick) was used to hold agarose-embedded hepatic specimens. Based on the calibration with this type of gel holder in place, the P– values were attenuated by 1.0% (500 kHz) and 6.8% (3 MHz). The attenuation for 500 kHz in this type of gel holder was significantly less than the former gel holders since this type of holder had an opening at the bottom, which was in the propagation paths of some 500 kHz elements.

The applied pressure levels used in the experiments are listed in Tables 3.1 and 3.2. The applied P– was corrected by the attenuation contributed by the plastic gel holder using the hydrophone measurement discussed above. Additionally, the applied P– was further corrected for the attenuation contributed by agarose hydrogel and porcine hepatic specimen, using reported values [11, 13, 21] and assuming linear propagation.

3.2.3 Experiments in RBC Phantoms and Lesion Analysis

Three different experimental sets were performed in RBC phantoms to investigate lesion production using dual-beam histotripsy. The applied P– values are listed in Table 3.1. Each intended treatment region was exposed with 100 pulses at a PRF of 1 Hz, and a single-focal-point exposure was performed.

Table 3.1 Peak negative pressures and time delays for capturing bubble cloud images used in the RBC phantom experiments of the dual-beam histotripsy study

Experimental Set	Case	500 kHZ			3MHz			Time Delay For Capturing Bubble Cloud Images (μs)
		Focal P– in Free-Field (MPa)*	Focal P– with Attenuation Correction (MPa)	Proportion (%)	Focal P– in Free-Field (MPa)*	Focal P– with Attenuation Correction (MPa)	Proportion (%)	
1	every case	11.7	10.6	38	20.3	17.1	62	9
2	1	0.0	0.0	0	33.0	27.8	100	5
	2	11.0	9.9	35	21.7	18.2	65	8
	3	15.8	14.3	51	16.1	13.6	49	9
	4	20.8	18.9	68	10.8	9.1	32	13
	5	29.4	26.6	100	0.0	0.0	0	17
3	every case	22.3	20.2	80	6.0	5.1	20	15

* The P– values in Experimental Set 1, 2 (Case 2-4), and 3 were linearly interpolated using the directly measured P– values for various driving voltages. The P– values of Case 1 and 5 in Experimental Set 2 were linearly interpolated using the linear summed P– values for various driving voltages.

(1) The arrival times of the 500 kHz and 3 MHz pulses were varied from no overlap to maximal P– overlap at the focus of the array transducer. More specifically, the time delay for 3 MHz relative to 500 kHz varied from –1.55 to 1.45 μs, where 0 μs is defined as the time point when the two pulses had maximal overlap in P–, and a negative time delay indicates the P– of the 3 MHz pulse arriving earlier than the P– of the 500 kHz pulse and vice versa. The applied pressures were chosen such that each individual frequency component did not reach the intrinsic threshold; rather, it could be exceeded only by the combination of the two.

(2) The relative amplitudes of the 500 kHz and 3 MHz pulses were varied to study the smallest reproducible lesions for each combination. The arrival times of the 500 kHz and 3 MHz in this experimental set were chosen to be the time delay when the two produced the maximal P– values of the composite waveforms.

(3) The propagation direction of the 3 MHz relative to the 500 kHz was varied from co-propagation, orthogonal-propagation, to counter-propagation to investigate effects in lesion

production. In this experimental set, all 500 kHz elements were firing together with one selected 3 MHz element to implement different propagation directions. The bottom 3MHz element was chosen for the co-propagation case, one selected 3 MHz element within the 3rd ring of the array transducer was chosen for the orthogonal-propagation (85 degrees), and the 3 MHz element attached to top frame was chosen for the counter-propagation case. The arrival times of the 500 kHz and 3 MHz in this experimental set were chosen to be the time delay when the two had maximal P– overlap.

The experimental setup for the treatment in RBC Phantoms is illustrated in Figure 3.5. For the visualization of the cavitational bubble clouds and their resulting damages in RBC phantoms, a digital, 1.3-megapixel, CMOS, mono-color camera (PN: FL3-U3-13Y3M-C, Flea® 3, PointGrey, Richmond, BC, Canada) was positioned perpendicularly to the dual-frequency array transducer facing one of its optical windows. A Nikon 4X objective was attached to the camera with extension tubes to magnify the image plane, giving the captured images a resolution of approximately 3.5 µm per pixel. A pulsed white-light LED was placed on the diametrically-opposed optical window of the dual-frequency array transducer, which provided back-lit illumination. This arrangement allowed for the visualization of the axial-lateral plane of the dual-frequency array transducer. The camera and the LED light source received trigger signals from the FPGA board, which maintained the synchronization of image capturing and the delivery of histotripsy pulses. For every delivered histotripsy pulse, two images were acquired, one (bubble cloud image) at the time when the maximal spatial extent of the bubble cloud was observed (see Table 3.1 for exact timing), and the other (lesion image) at 500 ms after the arrival of the pulse, where only histotripsy-induced damage in the RBC phantom was observed. The exposure time was 2 µs for every captured image. The RBC phantoms were mounted on a 3-axis motorized

positioner (Griffin Motion, Holly Springs, NC, USA) and submerged in the dual-frequency array transducer with an orientation for the visualization of axial-lateral-plane lesions.

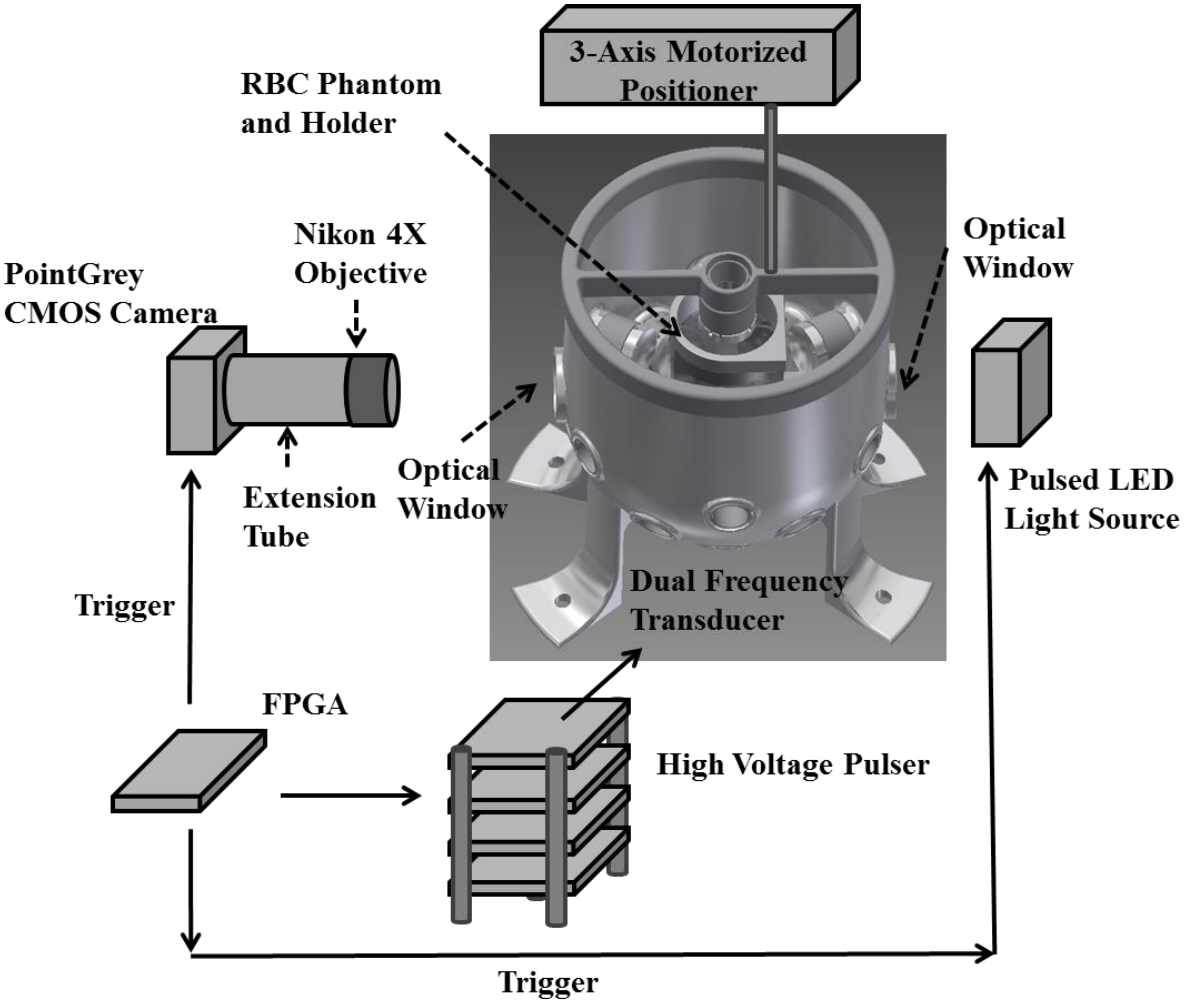

Figure 3.5 An illustration of the overall experimental setup in RBC phantom experiments.

These optical images were then post-processed with MATLAB (R2011a, MathWorks, Natick, MA, USA) using a method similar to those described in previous papers [11, 22, 23]. The lesion images were converted to binary images using the threshold calculated based on the mean intensity of the lesion. In order to exclude noise in the camera sensor and pre-existing isolated small white regions due to RBC layers being not 100% uniform, lesions smaller than

237 pixels (corresponding to regions less than 30 μm in radius) were excluded from the damage zone. By counting the number of pixels identified as damage zone and converting it to actual size with the help of a pre-captured scale image, the area, length, and width of the lesion were determined. During this analysis, the lesion was divided into two groups: 1) "main lesion," the center portion of the lesion which was induced by consistent bubble cloud presence, and 2) "peripheral damage," the damage zone outside of main lesion which was induced by incidental bubble presence. The bubble cloud images were quantified in a similar way, except the thresholds for binary image conversion were calculated based on the mean intensity of the bubble cloud. For experimental set 1, where the arrival times for 500 kHz and 3 MHz pulses were varied, a cavitation probability was further calculated based on the number of pulses with bubble cloud presence within the total delivered 100 pulses. The cavitation probabilities for bubble clouds generated in the main lesion and incidental bubbles generated in peripheral region were quantified separately.

3.2.4 Linear Transient Simulation with Fast Object-Oriented C++ Ultrasound Simulator (FOCUS) and Lesion Size Estimation

A linear transient simulation was performed using an ultrasound simulation tool, Fast Object-Oriented C++ Ultrasound Simulator (FOCUS, Version 437 for MATLAB 2010a and Windows 64-bit operating system, developed by Dr. Robert J. McGough *et al* from Michigan State University, MI, USA [24-26]). FOCUS is a cross-platform (for Windows, Linux, and MacOS) "free-ware" and it is written in object-oriented C++ with MATLAB user interface. In the simulation, "spherical shells" with a diameter of 20 mm and a focal length of 40 mm were selected to represent the elements within the dual-frequency array transducer. In order to

resemble the actual acoustic waveform better, the excitation pulse was chosen to be two-cycle, "Hanning-weighted tone-burst" pulse with the desired frequency, amplitude, and time delay. The elements were arranged in three-dimensional (3D) space according to the design of the transducer, and 3D pressure field calculation was performed for selected two-dimensional (2D) axial-lateral planes. The function "fnm_tsd" (called "transient_pressure" in the newer version) was used to calculate the transient pressure field using fast near-field methods and time-space decomposition. The sampling frequencies in time and space domain were chosen to be 40 MHz (4×10^7 samples / second) and 5×10^4 samples / meter.

For experimental set #2, where the relative amplitude proportion between the 500 kHz and 3 MHz pulses was varied, lesion size estimation was performed. 2D pressure fields in the axial-lateral plane were simulated using FOCUS and extrapolated to the applied pressure level. A pressure threshold was obtained using the same method described in [23], and then applied to the extrapolated 2D pressure field to estimate lesion sizes.

3.2.5 Experiments in Ex Vivo Porcine Hepatic Specimens and Histological Evaluation

Agarose-embedded porcine hepatic specimens were mounted on the Griffin 3-axis motorized positioner, and ultrasound B-mode imaging, instead of high speed photography, was used to monitor the histotripsy treatment. The ultrasound B-mode imaging was performed using a commercial ATL HDI 5000 ultrasound scanner (Advanced Technology Laboratories, Inc., Bothell, WA, USA) with ATL L12-5 linear probe. Each intended treatment region was exposed with 500 pulses at a PRF of 1 Hz, and a single-focal-point exposure was performed. Various pressure combinations, listed in Table 3.2, were applied to various regions of the specimens. In order to better identify smaller lesions after treatment, two large lesions (5 mm in separation)

using only the 500 kHz component were generated on the surface of the specimens, along with two large lesions, also using only the 500 kHz component, generated 3 mm right beneath the two surface lesions. These four lesions were used as landmarks, and a small lesion was then generated in between these two large lesions and 3 mm beneath the surface of the tissue specimen.

Table 3.2 Peak negative pressures used in the *ex vivo* porcine liver experiments of the dual-beam histotripsy study

Case	500 kHZ			3MHz		
	Focal P– in Free-Field (MPa)*	Focal P– with Attenuation Correction (MPa)	Proportion (%)	Focal P– in Free-Field (MPa)*	Focal P– with Attenuation Correction (MPa)	Proportion (%)
1	17.6	17.0	53	19.5	15.3	47
2	25.5	24.5	72	12.4	10.7	28
3	32.0	30.8	100	0.0	0.0	0

* The P– values in Case 1 (both frequencies) and 2 (only 3MHz component) were linearly interpolated using the directly measured P– values for various driving voltages. The P– values in Case 2 (only 500 kHz component) and 3 (only 500 kHz component) were linearly interpolated using the linear summed P– values for various driving voltages.

The lesions were evaluated with both ultrasound B-mode imaging and histological sections after treatment. A high-frequency ultrasound probe, RMV 707B (15 – 45 MHz, VisualSonics, Toronto, ON, Canada), along with a high-frequency ultrasound scanner, Vevo 770 (VisualSonics), was used to image the lesions after treatment. The axial and lateral dimensions of the lesions were then measured based on the hypoechoic regions that appeared in the recorded B-mode images. For histological evaluation, the treated porcine specimens were fixed with 10% phosphate buffered formalin (Fisher Scientific, Fair Lawn, NJ, USA) and sectioned into approximate 3-mm-thick slices along the axial-lateral planes of the lesions using a regular kitchen knife and surgical scalpels. These slices were then further processed into 4-µm-thick histological sections with 100 µm sectioning step size using a microtome and stained with hematoxylin and eosin (H&E). Visual inspection using bright field microscopy was performed to

identify the section with maximal spatial extent of the damage among all sections for each sample. The maximal extents of the lesions in the lateral and axial directions were quantified based on the bright field microscopic images with the help of a pre-calibrated scale.

3.3 Results

3.3.1 Experiments in RBC Phantoms

1) *Varying Time Delays between 500 kHz and 3 MHz Pulses:* A total of 13 time delays were investigated, including –1.55, –0.65, –0.35, –0.25, –0.15, –0.05, 0.00, 0.05, 0.15, 0.25, 0.35, 0.65, 1.45 µs. The sample size for each case was nine, leading to a total of 117 lesions generated in RBC phantoms. Figures 3.6 and 3.7 summarize the result for this experimental set.

Figure 3.6 shows directly measured acoustic waveforms (at a pressure level [combined P– = ~14 MPa] lower than that used in the RBC experiments) and representative lesion and bubble cloud images for various time delays. In order to increase readability, only 7 time delays (every other case) are shown. As can be seen from the figure, cavitational bubbles and lesions only occurred when the negative pressure peaks of the 500 kHz and 3 MHz pulses overlapped and added constructively. Neither lesions nor cavitational bubbles occurred where the negative pressure peaks of the 500 kHz and 3 MHz pulses did not overlap.

Figure 3.7 shows the quantitative result after lesion analysis, including width [Figure 3.7(a)], length [Figure 3.7(b)], and area [Figure 3.7(c)] of the main lesion, area of the peripheral damage [Figure 3.7(d)], and cavitation probabilities in main lesion [Figure 3.7(e)] and periphery [Figure 3.7(f)]. As can be seen, the width, length, area, and cavitation probability of the main lesion reached their maxima at 0 µs time delay, i.e., 500 kHz and 3 MHz pulses had maximal P– overlap. No significant changes were observed when the time delay changed to –0.05 or 0.05 µs.

When the time delay changed to even more negative or positive, the lesion size and cavitation probability in the main lesion decreased due to a reduction of combined P–. When the time delay was earlier than –0.50 μs or later than 0.20 μs, the cavitation probability in the main lesion decreased to less than 10%, and almost no lesions were observed. The lesion area and cavitation probability for the periphery showed a similar trend. Although their maxima both appeared at –0.25 μs time delay, they did not differ significantly from those at 0 μs.

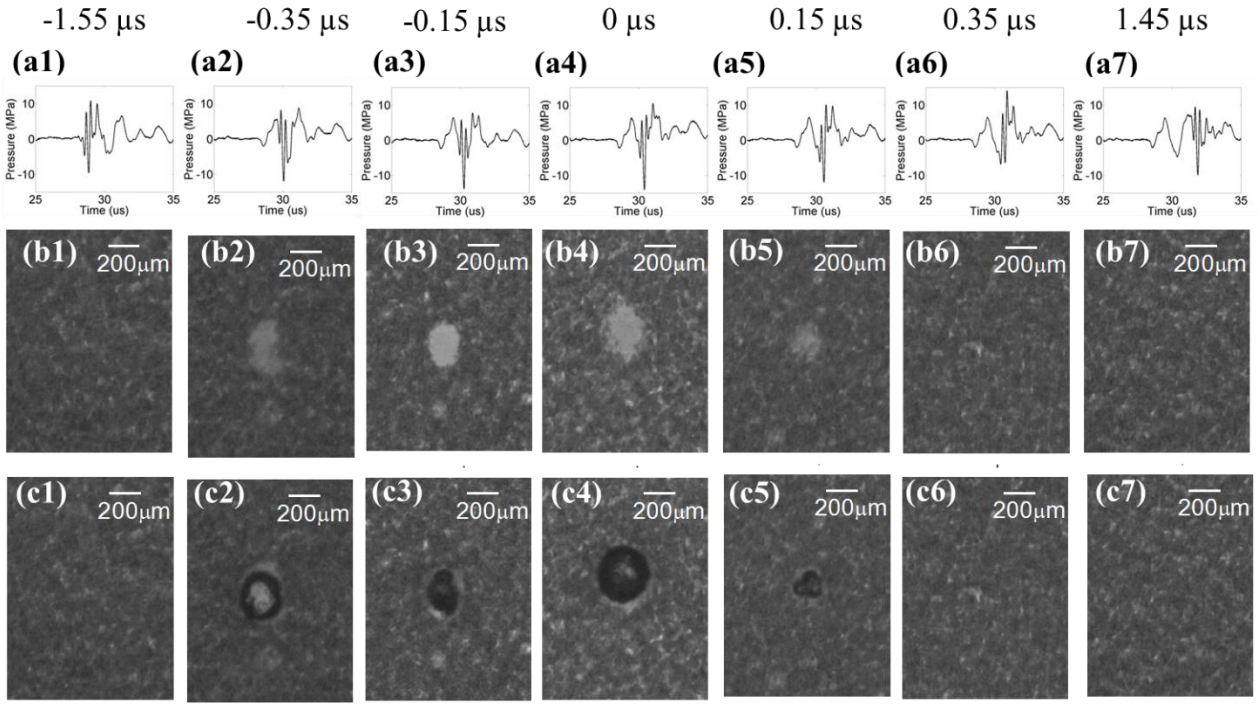

Figure 3.6 Results for experimental set #1. Due to limitation in hydrophone calibration, these waveforms (a1 – a7) were measured by the FOPH at a lower pressure level (~ ½ of the pressure used in the RBC experiments). All the bubble cloud and lesion images were taken in the axial-lateral plane of the transducer and the histotripsy pulses propagated from bottom to the top.

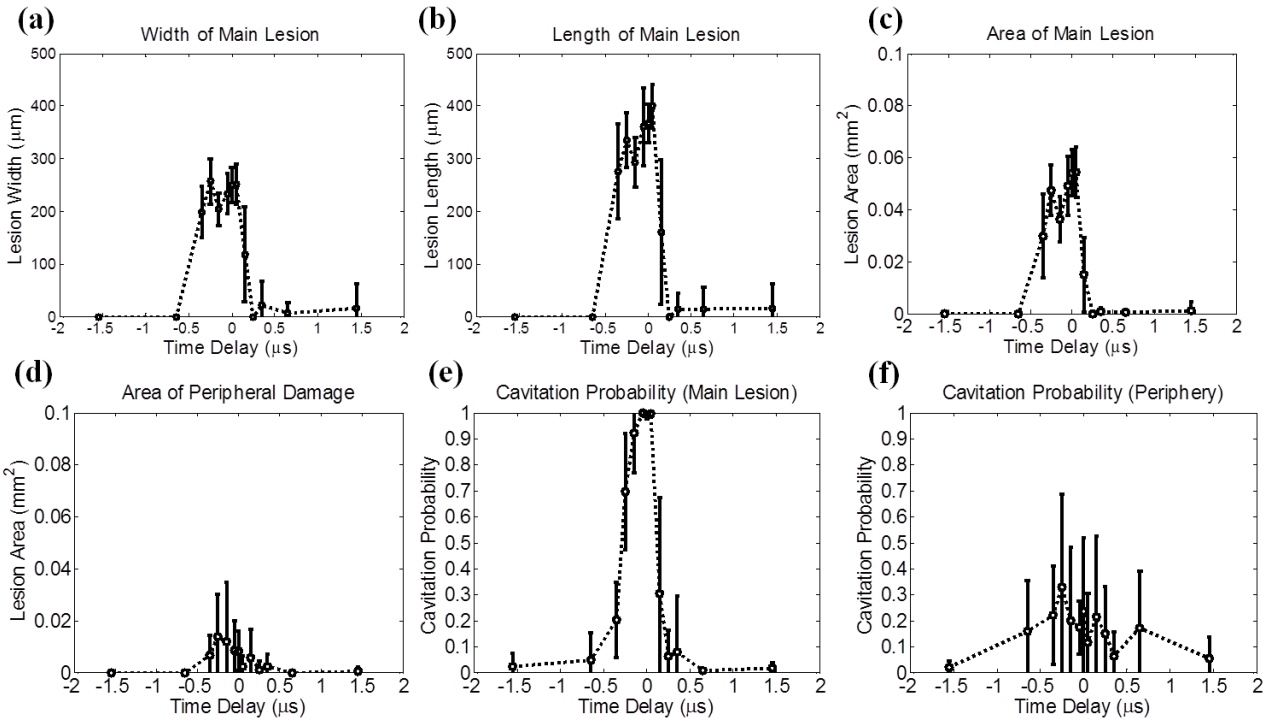

Figure 3.7 Quantitative results for experimental set #1. (a) Width of the main lesion, (b) length of the main lesion, (c) area of the main lesion, (d) area of the peripheral damage, (e) cavitation probability in the main lesion, and (f) cavitation probability in the periphery as a function of the time delay.

2) *Varying Relative Amplitudes between 500 kHz and 3 MHz Pulses:* A total of 5 different combinations, as listed in Table 3.1, were investigated, and each case had a sample size of six. Figure 3.8 shows representative lesion and bubble cloud images for each case. Figure 3.9 summarizes the quantitative results for the width [Figure 3.9(a)], length [Figure 3.9(b)] and area [Figure 3.9(c)] of the main lesion and the area of the peripheral damage [Figure 3.9(d)]. As can be seen, the sizes of the lesions and bubble clouds increased as the relative proportion of the 500 kHz pulse amplitude increased. Size estimations for main lesions using FOCUS simulation tool are also plotted in Figures 3.9(a) – (c), and the estimations have a general agreement with phantom experiment results.

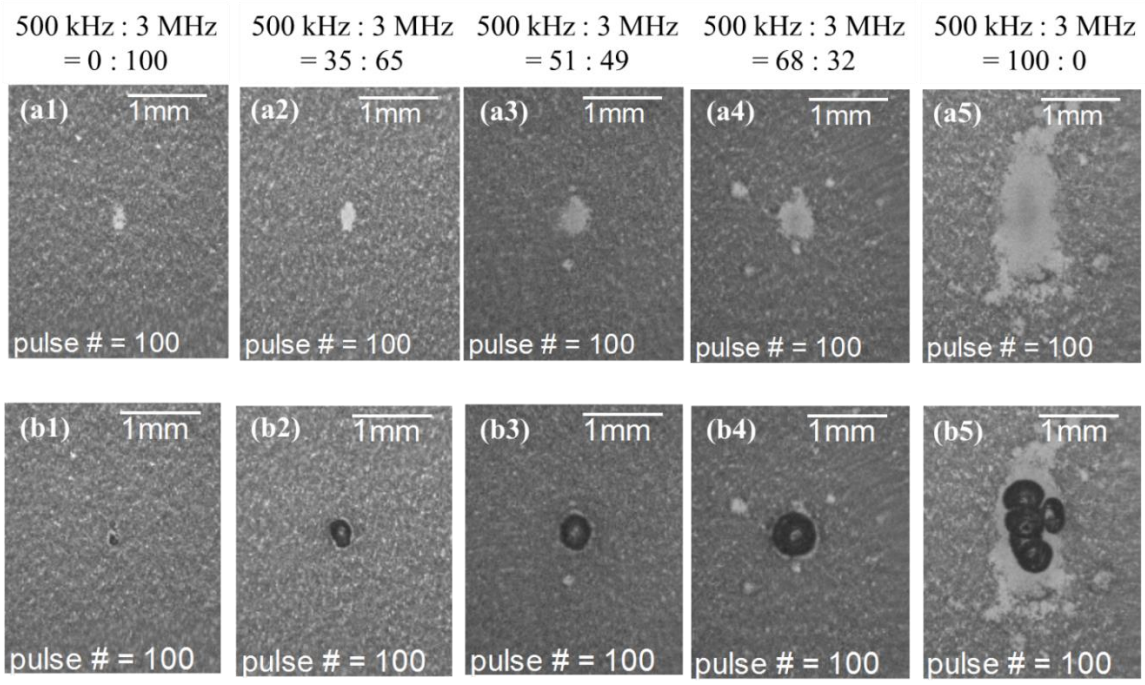

Figure 3.8 Results for experimental set #2. Figures in the first row (a1 - a5) show representative lesion images after 100 delivered histotripsy pulses in RBC phantoms. Figures in the second row (b1 - b5) show representative bubble cloud images in RBC phantoms. All the bubble cloud and lesion images were taken in the axial-lateral plane of the transducer and the histotripsy pulses propagated from bottom to the top.

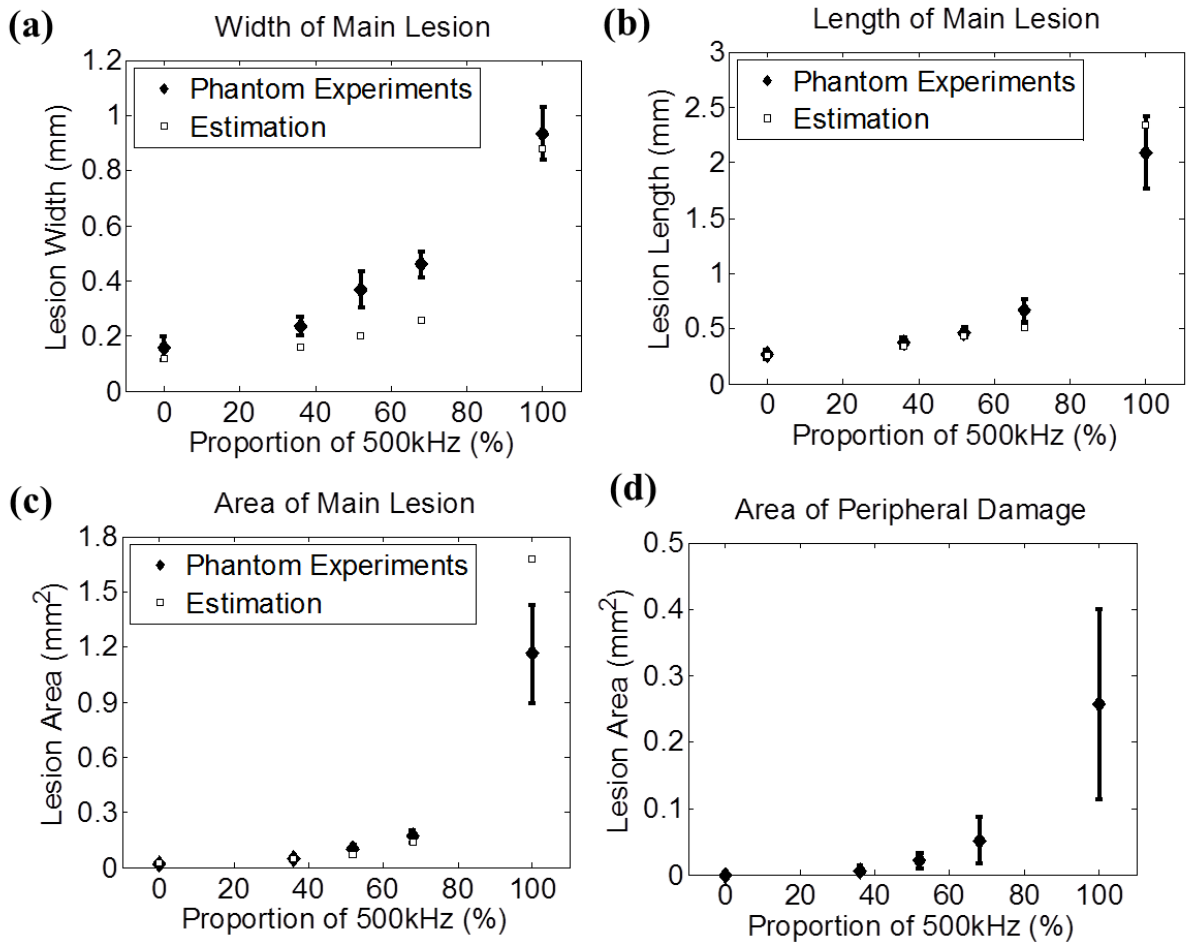

Figure 3.9 Quantitative results, along with estimations using FOCUS simulation, for experimental set #2. (a) Width of the main lesion, (b) length of the main lesion, (c) area of the main lesion, and (d) area of the peripheral damage as a function of the amplitude proportion of the applied 500 kHz pulse.

Figure 3.10 shows the number of incidental bubbles generated at the periphery, which are responsible for peripheral damage, as a function of the number of applied histotripsy pulses. As can be seen, the number of these bubbles started from its maximal value and rapidly decreased to almost no bubble presence after the 10^{th} pulse. Additionally, when the 500 kHz pulse amplitude fraction was higher, the number of incidental bubbles at the periphery increased and these bubbles disappeared more slowly.

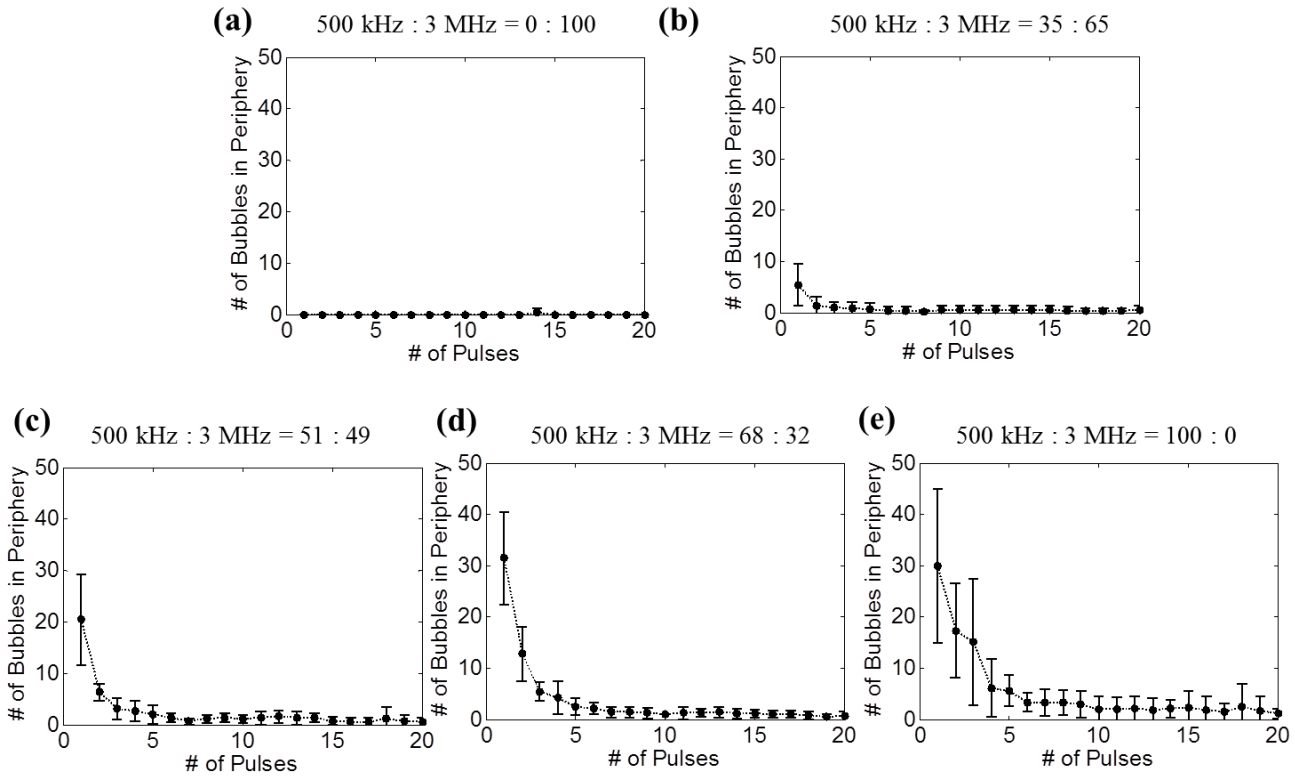

Figure 3.10 Number of incidental bubbles generated in the periphery of the focus during experimental set #2. Results after 20 pulses are not plotted since they are similar as the result of the 20th pulse.

3) *Varying Propagation Direction of the 3 MHz Pulse Relative to the 500 kHz Pulse*:

The propagation direction was varied from co-propagation, then counter-propagation, and to orthogonal-propagation, and each had a sample size of eight. Figure 3.11 shows the corresponding transducer firing arrangements [Figures 3.11(a1), 3.11(b1), and 3.11(c1)], 2D pressure fields using FOCUS simulations [Figures 3.11(a2), 3.11(b2), and 3.11(c2)], bubble cloud images [Figures 3.11(a3), 3.11(b3), and 3.11(c3)], and lesion images [Figures 3.11(a4), 3.11(b4), and 3.11(c4)] for different propagation directions. As can be seen, the lesion length in the axial direction for the counter-propagation case was significantly smaller than that for co-propagation case. Also, the lesion shape seemed tilted in the orthogonal-propagation case in

comparison to that in the co-propagation case. These results correspond well to the simulated 2D pressure (P–) fields.

The quantitative analysis of these lesions is summarized in Figure 3.12. The lesion size in the axial direction changed significantly from 1.21 mm for the co-propagation case to 0.52 mm for the counter-propagation case, while the lesion size in the lateral direction remained in similar level (0.70 mm for the co-propagation case and 0.63 mm for the counter-propagation case). The tilt angle changed from 1.0 degree for the co-propagation case to 26.8 degrees for the orthogonal-propagation case. This tilt angle was quantified by manually selecting the top and bottom points of the lesion, forming a central axis of the lesion, and then calculating the angle between this central axis and the axial propagation direction of the 500 kHz pulse component.

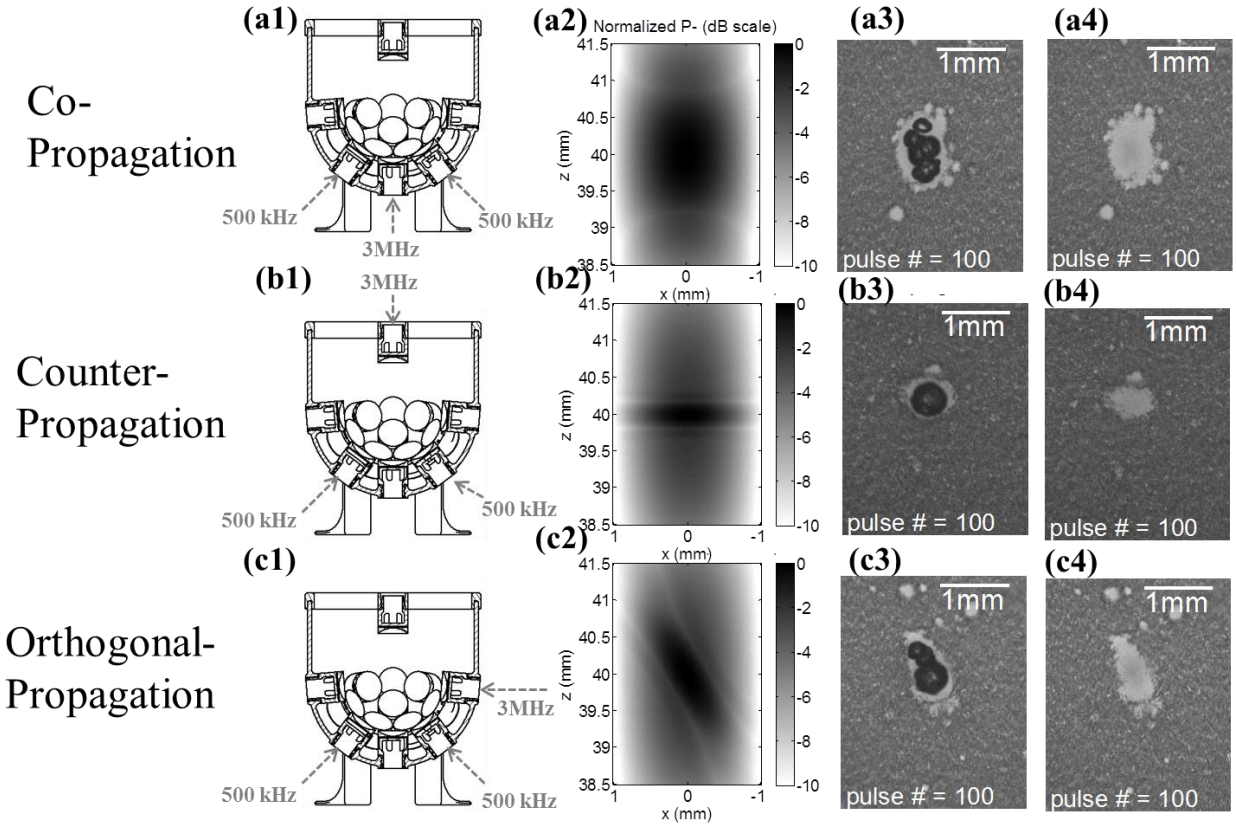

Figure 3.11 Results for the experimental set #3. Figures in the 1st column (a1, b1, and c1) illustrate the corresponding transducer firing arrangements. Figures in the 2nd column (a2, b2, and c2) show 2D pressure fields using linear transient simulation with FOCUS. Figures in the 3rd column and 4th column show representative bubble cloud and lesion images in RBC phantoms, respectively. All the bubble cloud and lesion images were taken in the axial-lateral plane of the transducer and the 500 kHz pulses propagated from the bottom to the top.

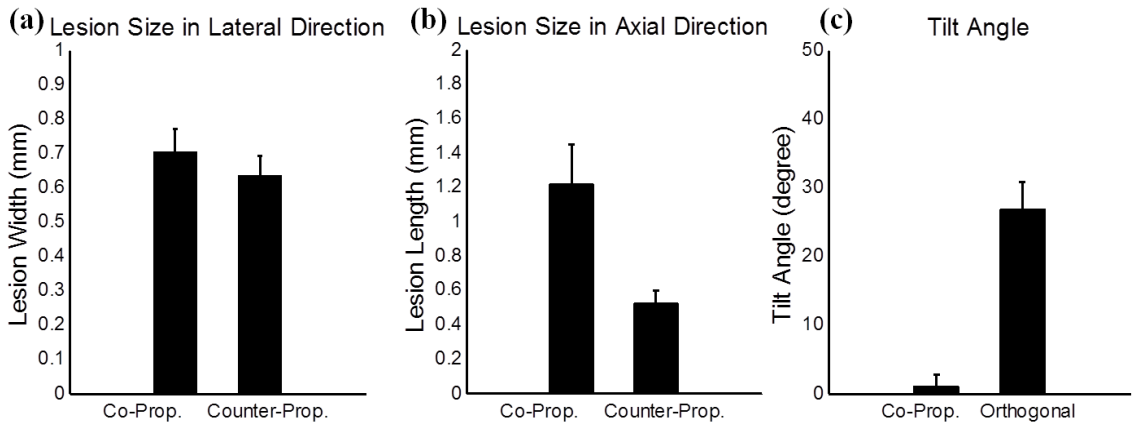

Figure 3.12 Quantitative results for the experimental set #3. (a) A comparison between co-propagation and counter-propagation for the width of the main lesion. (b) A comparison between co-propagation and counter-propagation for the length of the main lesion. (c) A comparison between co-propagation and orthogonal propagation for the tilt angle of the main lesion.

3.3.2 Experiments in Ex Vivo Porcine Hepatic Specimens

A total of 3 different pressure combinations, as listed in Table 3.2, were used to generate lesions in *ex vivo* porcine hepatic specimens, and each case had a sample size of two (N = 2). The representative histological sections are displayed in Figures 3.13(a) and (b). The intended treatment regions had lost their normal architecture and contained only acellular granular debris, and a larger spatial extent of the lesion occurred when a higher proportion of the 500 kHz pulse was applied. Figures 3.13(c) and (d) show representative B-mode images of the hepatic specimens after the application of 500 histotripsy pulses. Note that the B-mode ultrasound images were rotated 90 degrees from their original orientations in order to match the orientations of the histological sections. Hypoechoic regions occurred on B-mode images after histotripsy treatment, and these regions were larger when a higher proportion of 500 kHz pulse was applied. The histological sections and B-mode images for the case with 100% proportion of 500 kHz pulse are not displayed in Figure 3.13 since this paper focuses on using both pump (500 kHz) and probe (3MHz) pulses. The quantified lesion sizes in the lateral and axial directions are

shown in Figures 3.13(e) and (f), respectively. As can be seen, the quantified lesion sizes increased as the proportion of the 500 kHz pulse increased and the results quantified from histological sections and B-mode images were close to each other.

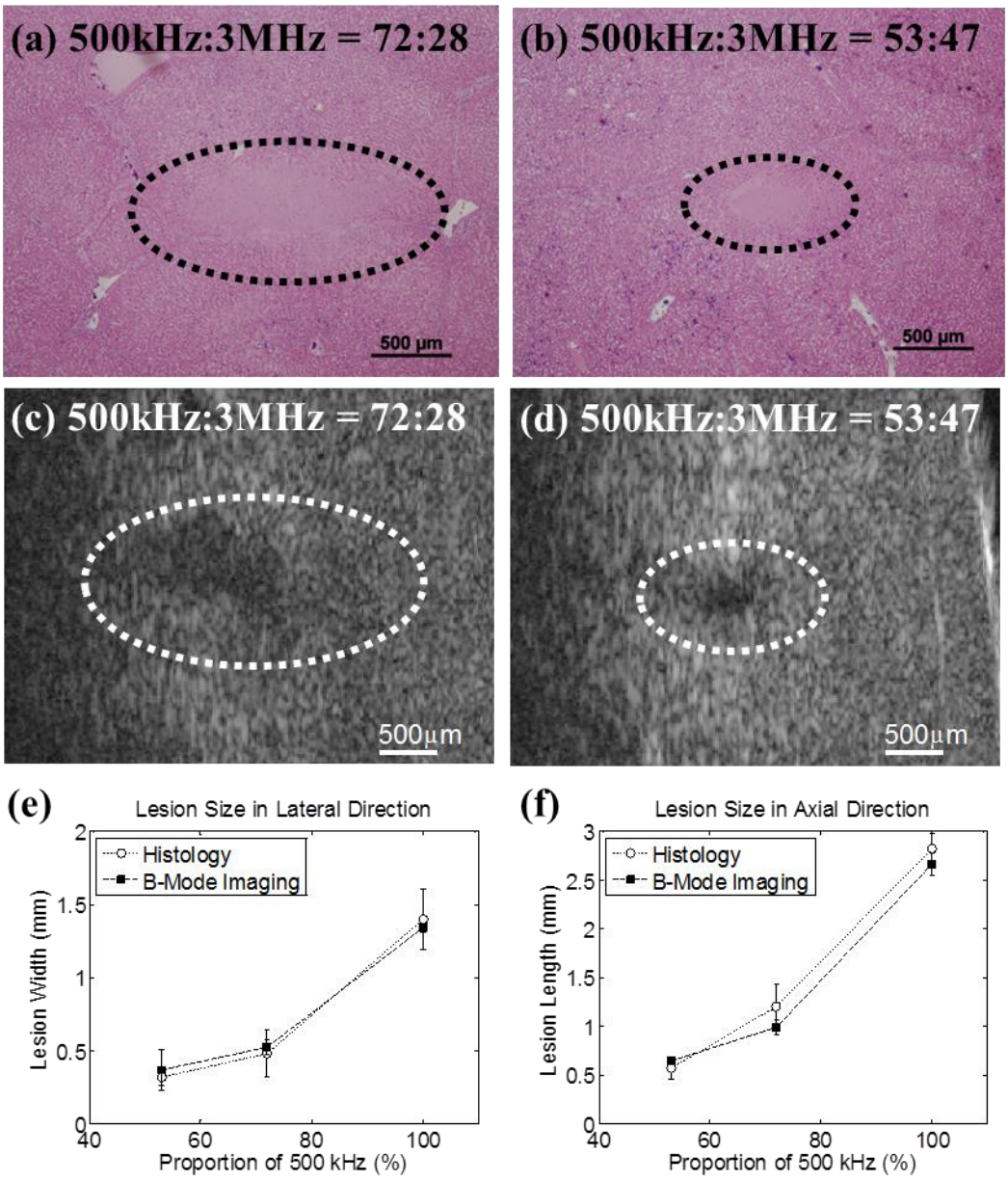

Figure 3.13 The results for excised porcine hepatic tissue treatment. The representative histological section and B-mode image for 500 kHz : 3 MHz = 72:28 are shown in (a) and (c), respectively. The representative histological section and B-mode image for 500 kHz : 3 MHz = 53:47 are shown in (b) and (d), respectively. The dotted lines circle the lesions being generated in (a) – (d). The quantified lesion sizes in the lateral and axial directions are shown in (e) and (f), respectively.

3.4 Discussion

In this paper, precise lesions were generated by "dual-beam histotripsy" pulses using the intrinsic threshold mechanism in both RBC phantoms and *ex vivo* porcine specimens. The dual-beam histotripsy pulse is comprised of a low-frequency pump pulse and a high-frequency probe pulse wherein a proper time delay between the two is chosen to allow their P– values to add constructively at the focus so as to exceed the intrinsic cavitation threshold. As can be seen in Figures 3.6 and 3.7, when the pump and probe pulses had maximal P– overlap (*i.e.* 0 µs time delay), consistent bubble clouds were generated with a cavitation probability of 100% and the size of the main lesion reached its maximum. No significant changes in the cavitation probability and lesion size were observed when the probe pulse (3 MHz) arrived 0.05 µs earlier or later than the pump pulse (500 kHz). When the time delay between the negative pressure peaks of the pump and probe pulses increased to 0.15 µs or more, the diminution of the combined P– led to decreases in the cavitation probability and lesion size (with higher variability), and both the cavitation probability and lesion size approached 0 when the negative phases of the pump and probe pulses did not have any overlap. Furthermore, these decreases were not symmetric around 0 µs time delay, which was likely due to the negative pressure phase for the 500 kHz pulse (in time domain) not being symmetric, as can be seen in Figure 3.3(a). This asymmetry in the 500 kHz waveform was probably not a result of nonlinear propagation since it also occurred at really low applied pressure level. Misalignment of individual elements was probably not the cause since phase corrections in free field for individual elements were performed during the calibration process for the phantom and tissue experiments. Imperfection in the stacking process during element assembly is a potential explanation since it only occurred in the epoxy-stacked 500 kHz elements.

Additionally, the size of the smallest reproducible lesions decreased when a higher proportion of the probe pulse (3 MHz) was applied, as indicated in Figures 3.8 and 3.9. With only 32% of the probe pulse, the lesion size decreased significantly from where pulses with 100% 500 kHz were applied. The lesion width decreased from 0.93 to 0.46 mm, the lesion length decreased from 2.09 to 0.66 mm, and the lesion area decreased from 1.16 to 0.17 mm^2. This demonstrates that, with the addition of a minor portion of the probe pulse, significantly smaller lesions can be achieved, in comparison to 100% pump pulse. This has a general agreement with a linear simulation using FOCUS as seen in Figure 3.9.

Moreover, the size and shape of the produced lesions can be further manipulated using various propagation directions between pump and probe pulses. (1) The axial dimension of the lesion can be further reduced when a probe pulse counter-propagates with a pump pulse, as shown in Figures 3.11 and 3.12. This "foreshortening" of the lesion results from the very short interaction time window when two short acoustic pulses (only one large negative pressure phase in the 2-cycle pulses) counter-propagate with each other (note that CW waves would not produce the same effect). (2) When a probe pulse orthogonally-propagates with a pump pulse, the lesion can be "tilted" from the propagation axis of the pump pulse. As shown in Figures 3.11 (c1) – (c4), when the pump pulse propagates from the bottom to the top and the probe pulse propagates from the right to the left, they firstly interact in the lower right corner of the focus. As they propagate through the focus, the two pulses produce a supra-threshold region moving from the lower right to the upper left, making the lesion appear tilted from the propagation axis of the pump pulse. Though using propagation directions other than co-propagation might not work in many applications due to the lack of accessible acoustic windows, it might still be applicable in some situations. For example, a transrectal probe pulse counter-propagating with transabdominal pump

pulse could be used in prostatic tissue ablation. Counter- or orthogonal-propagation of catheter-based probe pulses with transcostal/transabdominal pump pulses might also have potential in cardiac or hepatic tissue treatment allowing pulses from small-aperture high-frequency transducers to reach threshold levels not possible when used alone.

Peripheral damage induced by the incidental bubbles generated at the periphery of the focus was observed in both single-frequency histotripsy and dual-beam histotripsy (pump + probe). These incidental bubbles almost disappeared by the time the 20^{th} pulse was applied. A higher proportion of the pump pulse led to a larger area of peripheral damage, a larger number of incidental bubbles, and a slower rate in the decrease of the number of incidental bubbles. These incidental bubbles were likely seeded from the pre-existing dissolved sub-micron gas bubbles (samples could not be 100% degassed) or weak pockets. The application of histotripsy pulses firstly excited these weak nuclei at the periphery (where P– was below the intrinsic threshold) and then subsequently destabilized them, causing the incidental bubbles to disappear quickly. After that, the bubble clouds were preferentially generated at the location where the main lesion was forming. This "self-quenching" phenomenon limits the damage in the periphery, containing the lesion primarily to the volume where P– exceeds the intrinsic threshold.

Thus, "dual-beam histotripsy" can be quite beneficial in situations where precise treatment is required through a highly aberrative and attenuative medium. In the situation covered in this paper, the pump pulse is highly focused and can only cover a small region (–6dB beamwidths: 4.9 × 1.7 × 1.8 mm) or "target" for the probe pulse. In practice, it would be more ideal if the pump pulse could cover a larger ROI and the P– level could be raised uniformly across the volume. Therefore, we plan to investigate a lower-frequency pump with higher f-number (less focused) in the future. We also plan to study the feasibility of using commercial

imaging transducers for probe pulse generation. This could provide not only the steering capability for the probe pulse during treatment, but also the image guidance and feedback if it is used in conjunction with an imaging system. An imaging probe dual-beam histotripsy system could use available small windows, e.g., the transcostal region between ribs, to generate precise high frequency steerable pulses "enabled" by a much larger low-frequency pump transducer (e.g. , covering much of the rib cage). The use of a high frequency imaging transducer to generate precise lesions has many other interesting applications.

3.5 Conclusion

In this chapter, the capability of dual-beam histotripsy pulses for precise lesion formation is demonstrated both in RBC phantoms and *ex vivo* porcine tissues. Dual-beam histotripsy is accomplished by the application of a low frequency pump pulse that enables a high-frequency probe pulse to exceed the intrinsic cavitation threshold. With an adjustment in arrival times that allows constructive P− addition at the focus, sub-intrinsic-threshold pump and probe pulses can induce dense bubble cloud generation when P− summation exceeds the intrinsic cavitation threshold. The size of the smallest reproducible lesions decreases when the proportion of the high frequency probe pulse increases. Counter-propagation of the pump and probe pulse could foreshorten the lesion size in the axial direction. Dual-beam histotripsy can be useful in clinical applications in which precise tissue ablation is required with a longer propagation depth or through a highly attenuative or aberrative medium, such as transcranial therapy. This is particularly true if a small low-attenuation acoustic window is available for high frequency probe pulses.

3.6 References

[1] K.-W. Lin, A. P. Duryea, Y. Kim, T. L. Hall, Z. Xu, and C. A. Cain, "Dual-Beam Histotripsy: A Low-Frequency Pump Enabling a High-Frequency Probe for Precise Lesion Formation," *IEEE Trans Ultrason Ferroelectr Freq Control,* vol. 61, pp. 325-340, 2014.

[2] S.-i. Umemura, K.-i. Kawabata, and K. Sasaki, "In vitro and in vivo enhancement of sonodynamically active cavitation by second-harmonic superimposition," *J Acoust Soc Am,* vol. 101, pp. 569-577, 1997.

[3] S. Yoshizawa, J. Yasuda, and S.-i. Umemura, "High-speed observation of bubble cloud generation near a rigid wall by second-harmonic superimposed ultrasound," *J Acoust Soc Am,* vol. 134, pp. 1515-1520, 2013.

[4] J. Y. Chapelon, F. Dupenloup, H. Cohen, and P. Lenz, "Reduction of cavitation using pseudorandom signals [therapeutic US]," *Ultrasonics, Ferroelectrics and Frequency Control, IEEE Transactions on,* vol. 43, pp. 623-625, 1996.

[5] S. D. Sokka, T. P. Gauthier, and K. Hynynen, "Theoretical and experimental validation of a dual-frequency excitation method for spatial control of cavitation," *Physics in Medicine and Biology,* vol. 50, p. 2167, 2005.

[6] Y. Matsumoto, S. Yoshizawa, and T. Ikeda, "Dynamics of bubble cloud in focused ultrasound.," *Proc. 2nd ISTU, Seattle, USA,* pp. 290-299, 2002.

[7] T. Ikeda, M. Tosaki, Y. Matsumoto, N. Ohta, and T. Kitamura, "Renal stone comminution utilizing cloud cavitation erosion," *Proc. 3rd ISTU, Lyon, France,* pp. 49-55, 2003.

[8] T. Ikeda, S. Yoshizawa, M. Tosaki, J. S. Allen, S. Takagi, N. Ohta, T. Kitamura, and Y. Matsumoto, "Cloud cavitation control for lithotripsy using high intensity focused ultrasound," *Ultrasound in Medicine & Biology,* vol. 32, pp. 1383-1397, 2006.

[9] H.-L. Liu and C.-M. Hsieh, "Single-transducer dual-frequency ultrasound generation to enhance acoustic cavitation," *Ultrasonics Sonochemistry,* vol. 16, pp. 431-438, 2009.

[10] H. Hasanzadeh, M. Mokhtari-Dizaji, S. Zahra Bathaie, Z. M. Hassan, V. Nilchiani, and H. Goudarzi, "Enhancement and control of acoustic cavitation yield by low-level dual frequency sonication: A subharmonic analysis," *Ultrasonics Sonochemistry,* vol. 18, pp. 394-400, 2011.

[11] A. D. Maxwell, T.-Y. Wang, L. Yuan, A. P. Duryea, Z. Xu, and C. A. Cain, "A Tissue Phantom for Visualization and Measurement of Ultrasound-Induced Cavitation Damage," *Ultrasound in Medicine & Biology,* vol. 36, pp. 2132-2143, 2010.

[12] J. E. Parsons, C. A. Cain, and J. B. Fowlkes, "Cost-effective assembly of a basic fiber-optic hydrophone for measurement of high-amplitude therapeutic ultrasound fields," *J Acoust Soc Am,* vol. 119, pp. 1432-40, Mar 2006.

[13] A. D. Maxwell, C. A. Cain, T. L. Hall, J. B. Fowlkes, and Z. Xu, "Probability of Cavitation for Single Ultrasound Pulses Applied to Tissues and Tissue-Mimicking Materials," *Ultrasound Med Biol,* vol. 39, pp. 449-465, 2013.

[14] Z. Xu, A. Ludomirsky, L. Y. Eun, T. L. Hall, B. C. Tran, J. B. Fowlkes, and C. A. Cain, "Controlled ultrasound tissue erosion," *IEEE Trans Ultrason Ferroelectr Freq Control,* vol. 51, pp. 726-36, Jun 2004.

[15] W. W. Roberts, "Focused ultrasound ablation of renal and prostate cancer: current technology and future directions," *Urol Oncol,* vol. 23, pp. 367-71, Sep-Oct 2005.

[16] J. E. Parsons, C. A. Cain, G. D. Abrams, and J. B. Fowlkes, "Pulsed cavitational ultrasound therapy for controlled tissue homogenization," *Ultrasound Med Biol,* vol. 32, pp. 115-29, Jan 2006.

[17] A. M. Lake, T. L. Hall, K. Kieran, J. B. Fowlkes, C. A. Cain, and W. W. Roberts, "Histotripsy: Minimally Invasive Technology for Prostatic Tissue Ablation in an In Vivo Canine Model," *Urology,* vol. 72, pp. 682-686, 2008.

[18] Z. Xu, G. Owens, D. Gordon, C. Cain, and A. Ludomirsky, "Noninvasive creation of an atrial septal defect by histotripsy in a canine model," *Circulation,* vol. 121, pp. 742-9, Feb 16 2010.

[19] A. P. Duryea, T. L. Hall, A. D. Maxwell, Z. Xu, C. A. Cain, and W. W. Roberts, "Histotripsy erosion of model urinary calculi," *J Endourol,* vol. 25, pp. 341-4, Feb 2011.

[20] A. P. Duryea, A. D. Maxwell, W. W. Roberts, Z. Xu, T. L. Hall, and C. A. Cain, "In vitro comminution of model renal calculi using histotripsy," *IEEE Trans Ultrason Ferroelectr Freq Control,* vol. 58, pp. 971-80, May 2011.

[21] T. D. Mast, "Empirical relationships between acoustic parameters in human soft tissues," *Acoustics Research Letters Online,* vol. 1, pp. 37-42, 2000.

[22] T.-Y. Wang, Z. Xu, T. L. Hall, J. B. Fowlkes, and C. A. Cain, "An Efficient Treatment Strategy for Histotripsy by Removing Cavitation Memory," *Ultrasound in Medicine & Biology,* vol. 38, pp. 753-766, 2012.

[23] K.-W. Lin, Y. Kim, A. D. Maxwell, T.-Y. Wang, T. L. Hall, Z. Xu, J. B. Fowlkes, and C. A. Cain, "Histotripsy beyond the Intrinsic Cavitation Threshold using Very Short Ultrasound Pulses: Microtripsy," *IEEE Trans Ultrason Ferroelectr Freq Control,* vol. 61, pp. 251-265, 2014.

[24] D. Chen and R. J. McGough, "A 2D fast near-field method for calculating near-field pressures generated by apodized rectangular pistons," *J Acoust Soc Am,* vol. 124, pp. 1526-1537, 2008.

[25] J. F. Kelly and R. J. McGough, "Transient Fields Generated by Spherical Shells in Viscous Media," *AIP Conference Proceedings,* vol. 1113, pp. 210-214, 2009.

[26] J. F. Kelly and R. J. McGough, "A time-space decomposition method for calculating the nearfield pressure generated by a pulsed circular piston," *Ultrasonics, Ferroelectrics and Frequency Control, IEEE Transactions on,* vol. 53, pp. 1150-1159, 2006.

Chapter 4
Dual-Beam Histotripsy Using an Imaging Transducer

A majority component of this chapter is excerpted from a manuscript that has been submitted to *IEEE Transactions on Ultrasonics, Ferroelectric, and Frequency Control*. [1]

4.1 Introduction

The study in the previous chapter shows that a sub-threshold high-frequency probe pulse (< 2 cycles) can be enabled by a sub-threshold low-frequency pump pulse (< 2 cycles) to exceed the intrinsic threshold. This pump-probe method of controlling a supra-threshold volume is called "dual-beam histotripsy." In this chapter, we investigated the feasibility of using a diagnostic imaging transducer to provide the high-frequency probe pulse for dual-beam histotripsy. Using a diagnostic imaging transducer could provide not only the steering ability of the high-frequency pulse, thus making the resulting bubble clouds and lesions steerable, but also the image guidance and feedback during treatment if it is used in conjunction with an imaging system.

This dual-beam histotripsy using a diagnostic imaging transducer can have a number of applications. For example, a transcostal application (through ribs) of a low-frequency pump pulse can enable an imaging transducer pulse, which is applied between ribs, to perform noninvasive transcostal tissue ablation. A transperineal application of a low-frequency pump pulse can enable a transrectal imaging transducer pulse to perform prostatic tissue ablation. This

approach can also be useful in transcranial therapies wherein a low-frequency pump pulse is applied transcranially in conjunction with an imaging transducer pulse that is applied through a small surgically-removed skull opening.

Conventionally, the transmission pulse of a diagnostic ultrasound transducer is kept a significant low-intensity/low-pressure level to avoid inducing any bioeffects. Thermal index (TI) and mechanical index (MI) are the two primary metrics that the Food and Drug Administration (FDA) uses to regulate the acoustic output of a diagnostic ultrasound system. However, for therapeutic ultrasound system, these restrictions no longer apply, and some studies have investigated using diagnostic ultrasound transducer to perform therapy procedures. Specifically, Bailey *et al* utilized acoustic radiation forces generated by a diagnostic transducer and a Verasonics system to displace kidney stones in order to expel small stones or relocate an obstructing stone to a nonobstructing location [2-4].

In this chapter, a 20-element 345 kHz array transducer was used to provide the low-frequency pump pulses, while an ATL L7-4 imaging transducer (ATL/Philips Healthcare, Andover, MA, USA) pulsed by a Verasonics ultrasound system was used to generate the high-frequency probe pulses. The 345 kHz array transducer was driven by a custom high voltage pulser, controlled by a field-programmable gate array (FPGA) development board which maintained the synchronization of the delivery between pump and probe pulses. The feasibility of generating bubble clouds and lesions using this dual-beam histotripsy pulse approach with an imaging transducer was tested using red-blood-cell (RBC) tissue mimicking phantoms. The capability of steering bubble clouds and lesions by steering the imaging transducer was also investigated. Optical images were acquired by a high speed camera to visualize the bubble

clouds and lesions generated in RBC phantoms, and the acquired optical images were post-processed using MATLAB (MathWorks, Natick, MA, USA) for lesion analysis.

4.2 Methods

4.2.1 Sample Preparation

Experiments were performed on red-blood-cell (RBC) tissue-mimicking phantoms to investigate the treatment effect of the dual-beam histotripsy using imaging transducer. The procedures described in this study were approved by the University of Michigan's Committee on Use and Care of Animals.

The RBC tissue-mimicking phantoms can be used for the visualization and quantification of cavitation-induced damage [5]. In this study, fresh canine blood was obtained from adult research canine subjects in an unrelated study. An anticoagulant solution of citrate-phosphate-dextrose (CPD) (C7165, Sigma-Aldrich, St. Louis, MO, USA) was added to the blood with a CPD-to-blood ratio of 1:9 (v:v), and the blood was kept at 4℃ and used within 3 weeks. A low-melting-point agarose powder (AG-SP, LabScientific, Livingston, NJ, USA) was used along with the canine blood to prepare RBC phantoms following the protocol described in [5].

4.2.2 Histotripsy Pulse Generation and Calibration

Low-frequency pump pulses were generated by a custom, 20-element 345 kHz array transducer [Fig. 4.1(a)]. Each element consisted of two 690 kHz, 50-mm-diameter piezoceramic discs (SM111, Steiner and Martins, Miami, FL, USA) stacked together with epoxy, and individually mounted to a stereo-lithography-printed acoustic lens with a geometric focus of 150 mm (material: Accura® 60, 3D Systems, Rock Hill, SC, USA). The elements were confocally

aligned and arranged into two rings: 1) 1st ring – eight elements with a 38-degree tilt angle, and 2) 2nd ring – twelve elements with a 62-degree tilt angle. The corresponding f-number of the 345 kHz array transducer was 0.55. To generate short therapy pulses, a custom high voltage pulser developed in-house was used to drive the transducer. The pulser was connected to a field-programmable gated array (FPGA) development board (Altera DE1, Terasic Technology, Dover, DE, USA) specifically programmed for dual-beam histotripsy therapy pulsing.

A fiber-optic probe hydrophone (FOPH) [6] was used to measure the acoustic output pressure of the 345 kHz array transducer. The array transducer was positioned in a glass water tank filled with degassed water. Figures 4.1(b) – (f) shows the calibration results of the 345 kHz array transducer, including a representative focal pressure waveform at P– = 20MPa [Figure 4.1(b)], total focal P– as a function of peak-to-peak driving voltage [Figure 4.1(c)], and one-dimensional (1D) beam profiles in the lateral [Figure 4.1(d)], elevational [Figure 4.1(e)], and axial [Figure 4.1(f)] directions. The -6dB-beamwidths (calculated based on P–) were measured to be 2.9 (lateral), 3.1 (elevational) and 10.0 mm (axial). Pressure levels after inducing cavitation on the FOPH (P– > 20 MPa) were estimated by the summation of the output focal P– values from individual elements. In a previous study [7], this estimate had a good agreement with the P– measured directly in a higher cavitation threshold medium, 1,3 butanediol.

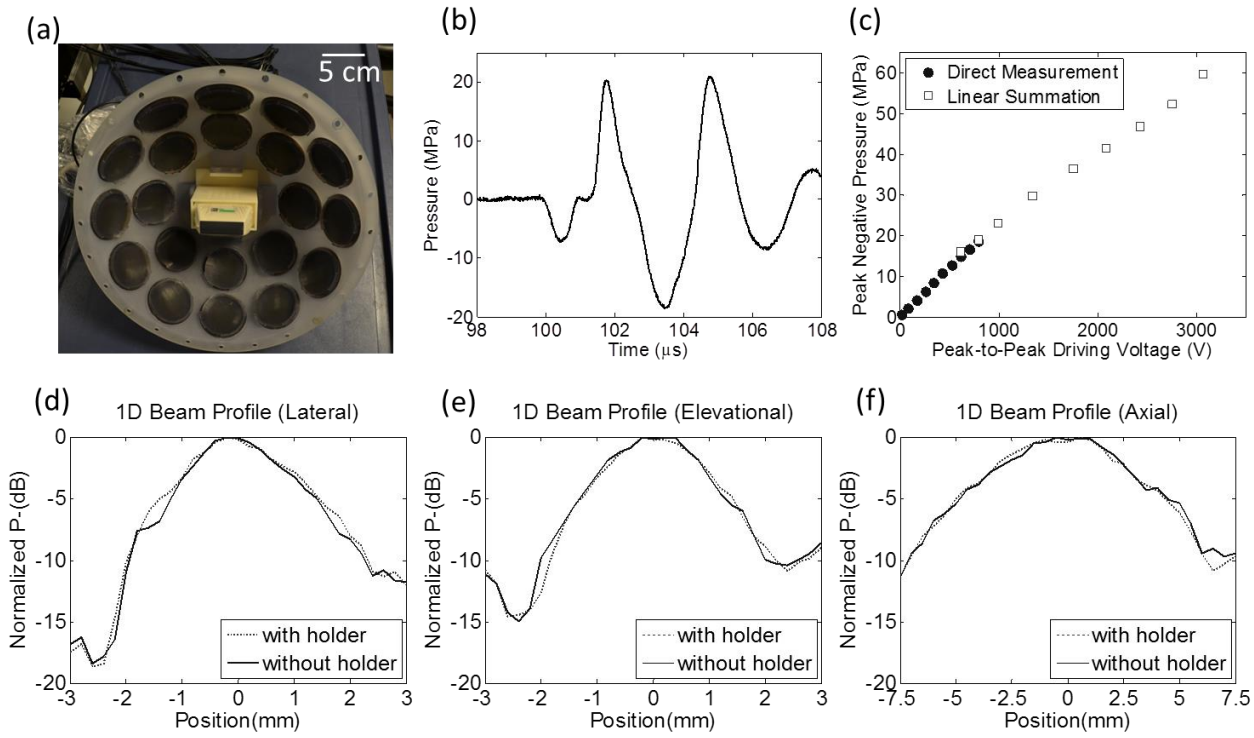

Figure 4.1 The 20-element 345 kHz array transducer and its calibration results. (a) A picture of the 345 kHz array transducer with the ATL L7-4 imaging transducer inserted into its center hole. (b) A representative focal acoustic waveform in the free-field. (c) Peak negative pressure as a function of peak-to-peak driving voltage. 1D beam profiles in the lateral (c), elevational (d), and axial (e) directions.

High-frequency probe pulses were generated by a commercial linear imaging transducer, ATL L7-4 (Advanced Technology Laboratories, Inc., Bothell, WA, USA, acquired by Philips Healthcare, Andover, MA, USA in 1998). This ATL L7-4 imaging transducer has 128 elements, a nominal bandwidth of 4.0 – 7.0 MHz, and a field of view of 38mm. The imaging transducer was mounted in the center hole of the 345 kHz array transducer with a custom stereo-lithography-printed acrylonitrile-butadiene-styrene (ABS) plastic adapter wherein the surface of the imaging transducer was 31 mm away from the focus of the 345 kHz array transducer. A Verasonics V-1 Data Acquisition System (Versonics, Redmond, WA, USA) was used to pulse the imaging transducer at 5 MHz and the imaging transducer was set to focus at a depth of 31

mm using conventional B-mode beamforming with all 128 elements transmitting (effective f-number in lateral direction = 0.82). Figure 4.2 shows the FOPH calibration results of the L7-4 imaging transducer, including a representative focal pressure waveform [Figure 4.2(a)], focal P– as a function of driving voltage setup on Verasonics [Figure 4.2(b)], and 1D beam profiles in the lateral [Figure 4.2(c)], elevational [Figure 4.2(d)], and axial [Figure 4.2(e)] directions. These beam profiles [Figures 4.2(c) – (e)] were measured at the highest driving voltage of Verasonics (50 V), and the measured –6dB-beamwidths were 0.4 (lateral), 2.2 (elevational), and 3.5 mm (axial). Figure 4.2(f) shows the FOPH-measured P– values at the steered locations when the imaging transducer was steered laterally (from -1.2 mm to 1.2 mm at 31 mm depth) and it demonstrates that there isn't significant decrease in P– in this steering range.

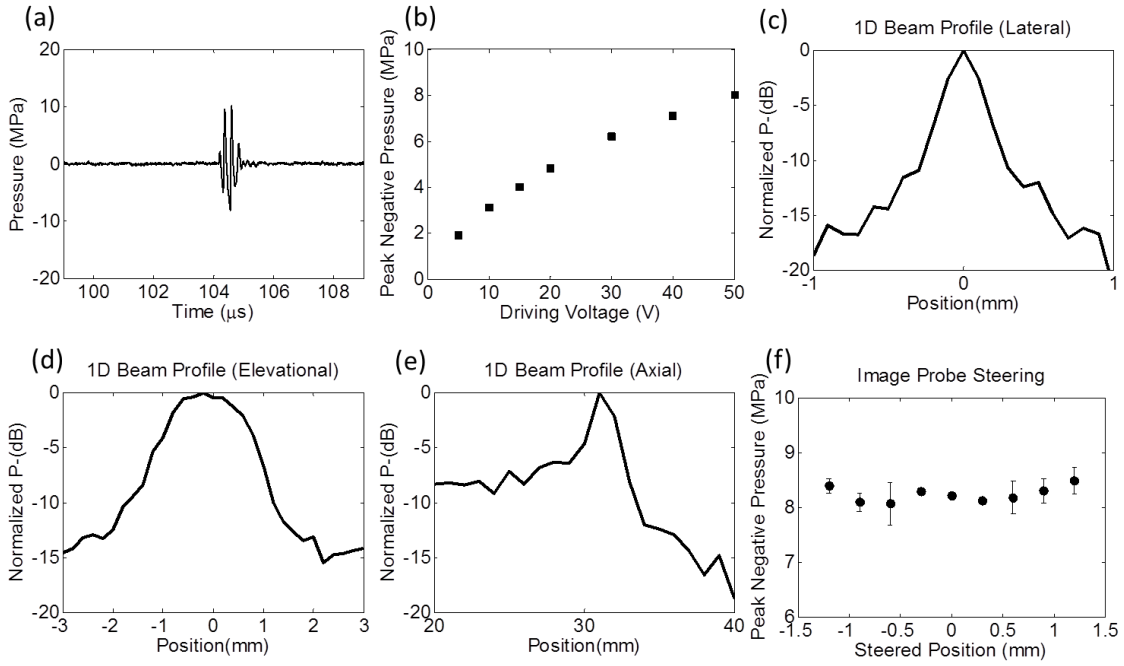

Figure 4.2 Calibration results of the ATL L7-4 imaging transducer pulsed by the Verasonics system. (a) A representative acoustic waveform in the free-field when the imaging transducer is focused at a depth of 31 mm and driven at 50 V by the Verasonics system. (b) Peak negative pressure as a function of the driving voltage in Verasonics system. 1D beam profiles in the lateral (c), elevational (d), and axial (e) directions. (f) Peak negative pressure at the steered location when the imaging transducer is steered laterally (N=2).

The Verasonics system received trigger signals from the FPGA board to maintain synchronization of low-frequency pump and high-frequency probe pulses. Figure 4.3 shows a representative waveform of the low-frequency pump pulse [Figure 4.3(a)], the high-frequency probe pulse [Figure 4.3(b)], and the combined pulse when both pulses fired concurrently [Figure 4.3(c)]. The pressure level in Figure 4.3 is lower than the pressure level applied in RBC phantom experiments, since the waveform at that pressure level couldn't be directly measured with the FOPH (inducing cavitation on the fiber tip).

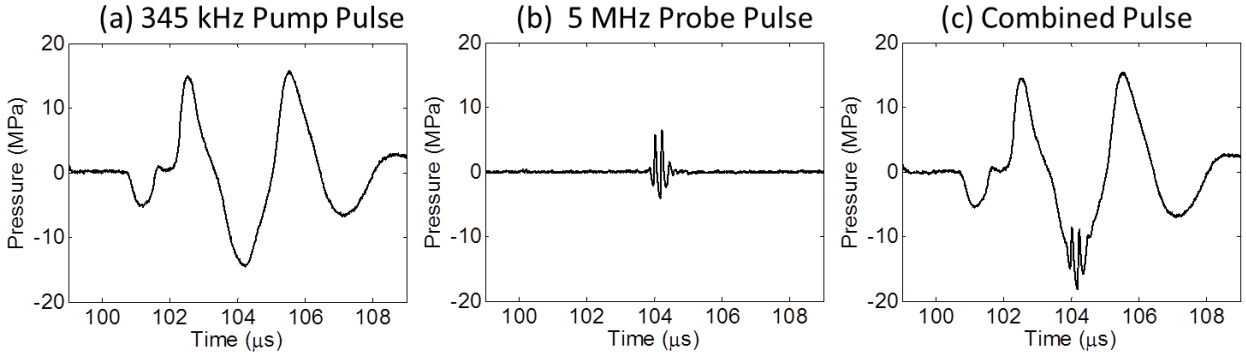

Figure 4.3 Representative FOPH-measured acoustic waveforms of (a) a 345 kHz pump pulse, (b) a 5 MHz probe pulse, and (c) a combined pulse when both the 345 kHz pump pulse and the 5 MHz probe pulse are firing (a direct measurement when both are transmitting).

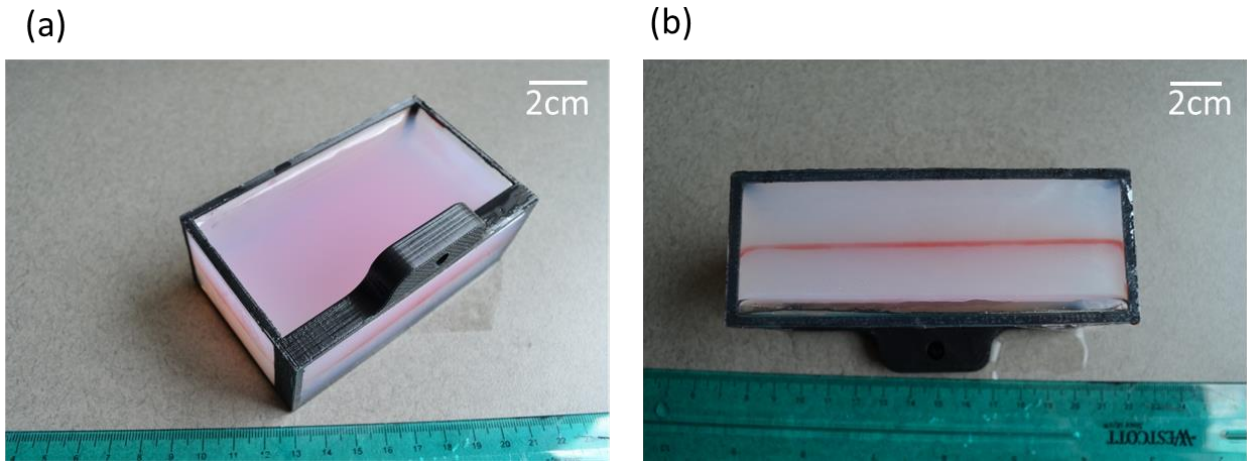

Figure 4.4 Pictures of a representative RBC phantom in a gel holder. (a) An angled view of the phantom. (b) A top-down view from the side facing the imaging transducer during experiments.

The RBC phantoms were prepared in custom rectangular gel holders (40 × 105 × 62.5 mm, shown in Figure 4.4) consisting of an acrylonitrile butadiene styrene (ABS) plastic supporting frame and thin polycarbonate membranes (254 μm thick) glued on four sides. A 3M Scotch® tape was attached to another side for holding liquid agarose gel during RBC phantom preparation process, and the tape was later removed for experiments. Based on the calibration with a representative gel holder in place, the P– for the 345 kHz array transducer was attenuated by 8.8%; however, the 1D beam profiles did not change significantly, as shown in Figures 4.1(d) – (f). The transmitted acoustic waves of the imaging transducer were not expected to be attenuated by the gel holders since 1) the side of the gel holders facing the imaging transducer had an ABS plastic frame much wider than the imaging transducer, and 2) the 3M Scotch® tape that attached to that side was removed before experiments.

4.2.3 Experiments in RBC Phantoms and Lesion Analysis

The experimental setup for the treatment in RBC phantoms is illustrated in Figure 4.5. The 345 kHz array transducer was submerged in a glass tank filled with degassed water, while the ATL L7-4 imaging transducer was inserted into its center hole. The RBC phantoms were mounted on a 3-axis motorized positioner (Velmex, Bloomfield, NY, USA) and submerged in the water tank with an orientation for the visualization of axial-lateral-plane lesions.

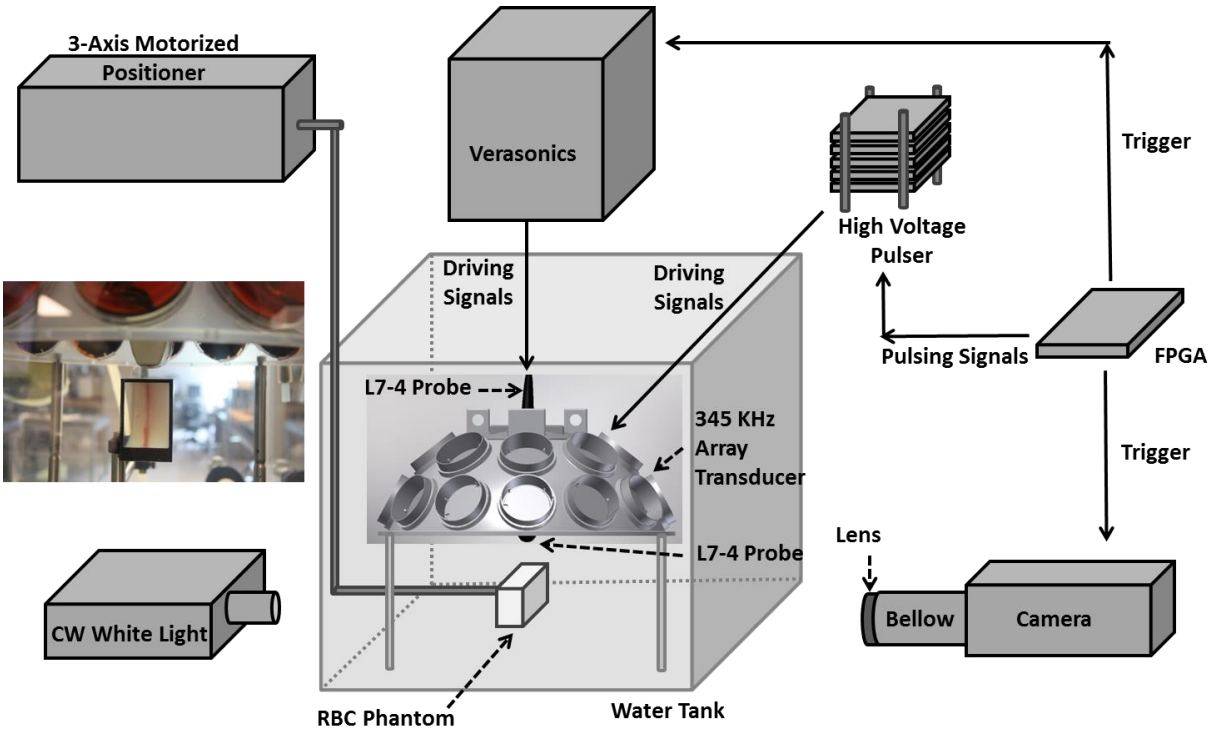

Figure 4.5 An illustration of the overall experimental setup in RBC phantom experiments.

Each intended treatment region in the RBC phantoms was exposed to 200 histotripsy pulses at a pulse repetition frequency of 1 Hz. Single-focal-point exposures were performed in each case and the applied pressure level is listed in Table 4.1. Two experimental sets were performed in this study to achieve the following two goals.

1) To investigate the feasibility of this dual-beam histotripsy using imaging transducer by comparing the lesions generated using three types of pulses: i) a sub-threshold low-frequency pump pulse, ii) a sub-threshold pump pulse enabling a sub-threshold imaging transducer pulse to exceed the intrinsic threshold, and iii) a supra-threshold low-frequency pump pulse.

2) To study lesion steering by laterally steering the pump-pulse-enabled imaging pulse using the Verasonics System.

A digital, 1-megapixel, CMOS, mono-color camera (Phantom V210, Vision Research, Inc., Wayne, NJ, USA) was used to visualize the cavitational bubble clouds and their resulting damages in RBC phantoms. With an additional magnifying lens (Tominon, 1:4.5, f = 135 mm) and optical bellow, the resolution of these captured images was approximately 13 μm per pixel. A continuous wave (CW) white light source was used to provide back-lit illumination for high speed photography. The camera received trigger signals from the FPGA board, which maintained the synchronization of image capturing and the delivery of histotripsy pulses. For every delivered histotripsy pulse, two images were acquired, one (bubble cloud image) at the 40 μs when the maximal spatial extent of the bubble cloud was observed, and the other (lesion image) at 500 ms after the arrival of the pulse, where only histotripsy-induced damage in the RBC phantom was observed. The exposure time was 2 μs for every captured image.

These optical images were then post-processed with MATLAB (R2011a, MathWorks, Natick, MA, USA) using a method similar to those described in previous papers [5, 8-10]. The bubble cloud and lesion images were separately converted to binary images using the threshold calculated based on the mean intensity of the bubble cloud and lesion, respectively. By counting the number of the pixels in the binary image and converting it to actual size with the help of a pre-captured scale image, the area, length, and width of the lesion were determined. In order to exclude noise in the camera sensor and pre-existing isolated small regions due to RBC layers being not 100% uniform, regions less than 30 μm in radius were excluded. During this analysis, the lesion was divided into two groups: 1) "main lesion," the center portion of the lesion which was induced by consistent bubble cloud presence, and 2) "peripheral damage," the damage zone outside of main lesion which was induced by incidental bubble presence. For experimental set 2, wherein the imaging probe was steered laterally, a cavitation probability was further calculated

based on the number of pulses with bubble cloud presence within the total delivered 200 pulses. The cavitation probabilities for bubble clouds generated in the main lesion and incidental bubbles generated in the peripheral region were quantified separately.

Table 4.1 Peak negative pressures used in the RBC phantom experiments of the dual-beam histotripsy study using an imaging transducer

Experimental Set	Case	345 kHZ			5MHz		
		Focal P– in Free-Field (MPa)*	Focal P– with Attenuation Correction (MPa)**	Proportion (%)	Focal P– in Free-Field (MPa)	Focal P– with Attenuation Correction (MPa)***	Proportion (%)
1	1	24.7	22.3	100	0	0	0
	2	24.7	22.3	76	8.0	7.0	24
	3	30.4	27.5	100	0	0	0
2	Every case	24.7	22.3	76	8.0	7.0	24

* The P– values were linearly interpolated using the linear summed P– values shown in Figure 4.1(c).
** The P– values for 345 kHz pulses were linearly corrected by the attenuation contributed by the plastic gel holder (using FOPH measurement) and agarose hydrogel (using previously reported attenuation coefficients [5, 7]).
*** The P– values for 5 MHz pulses were linearly corrected by the attenuation contributed by agarose hydrogel (using previously reported attenuation coefficients [5, 7]).

4.3 Results

4.3.1 Feasibility of Dual-Beam Histotripsy using An Imaging Transducer

A total of 21 lesions were generated in RBC phantoms with three types of histotripsy pulses listed in Experimental Set 1 of Table 4.1 (seven lesions for each case). These three types included 1) a sub-threshold 345 kHz pump pulse, 2) a sub-threshold 5 MHz probe pulse enabled by a sub-threshold 345 kHz pump pulse to exceed the intrinsic threshold, and 3) a supra-threshold 345 kHz pump pulse.

Figure 4.6 shows representative bubble cloud images at various stages (pulse # = 1, 31, 100, and 200) of the treatment, while Figure 4.7 shows representative lesion images at these stages of the treatment. As seen in the figures, all three cases had sparsely-distributed single cavitational bubbles generated at the first pulse (we called these “incidental bubbles” in the

previous paper [10]). After the 30th pulse, Case 1 pulses no longer produced incidental bubbles (see discussion in [10]), while Cases 2 and 3 pulses produced consistent dense bubble clouds. Moreover, the sizes of the bubble clouds in Case 2 were significantly smaller than those in Case 3, and the locations where the bubble clouds generated were more confined in Case 2. At the end of the treatment, Cases 2 and 3 had a confined central lesion (main lesion) induced by consistent bubble cloud generation along with some scattered peripheral damage induced by incidental bubbles generated at the beginning of the treatment. Case 1 only had scattered damage from incidental bubbles without a confined central lesion.

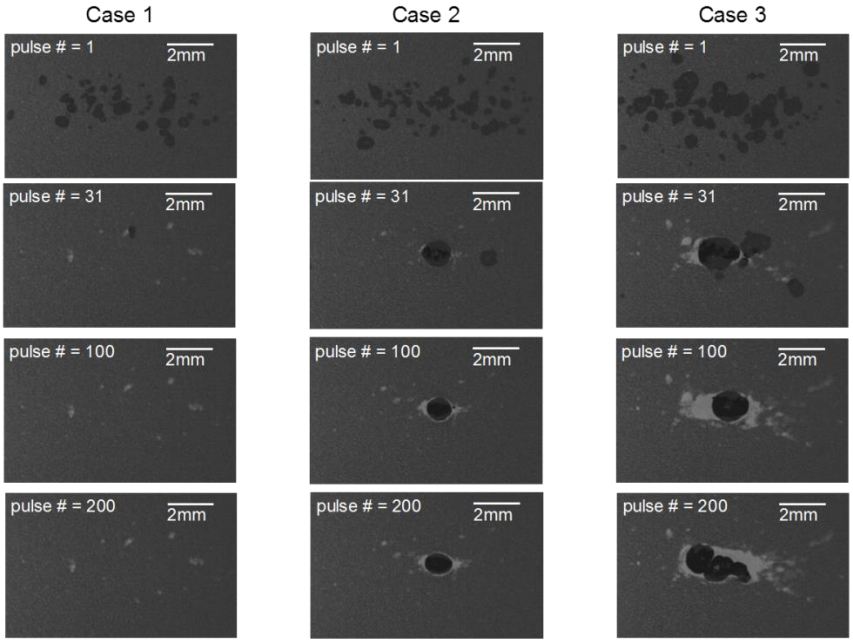

Figure 4.6 Representative bubble cloud images in the first set of the RBC phantom experiments. Dual-beam histotripsy pulses propagated from the left to the right of these images.

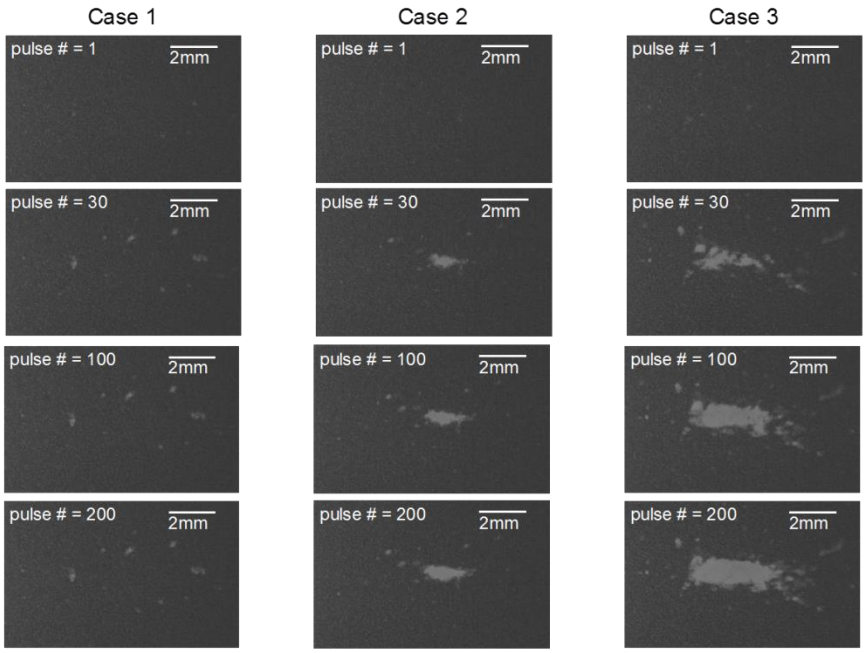

Figure 4.7 Representative lesion images in the first set of the RBC phantom experiments. Dual-beam histotripsy pulses propagated from the left to the right of these images.

Figure 4.8 summarizes the quantitative results from lesion analysis. As can be seen, when an imaging transducer pulse was applied together with a low-frequency pump pulse (Case 2), the size of the main lesion was significantly smaller than that for low-frequency pump pulse alone (Case 3). The size of the main lesion in Case 1 was almost 0. The areas of the peripheral damage for all three cases were in similar level, with Case 2 having the lowest average value.

.

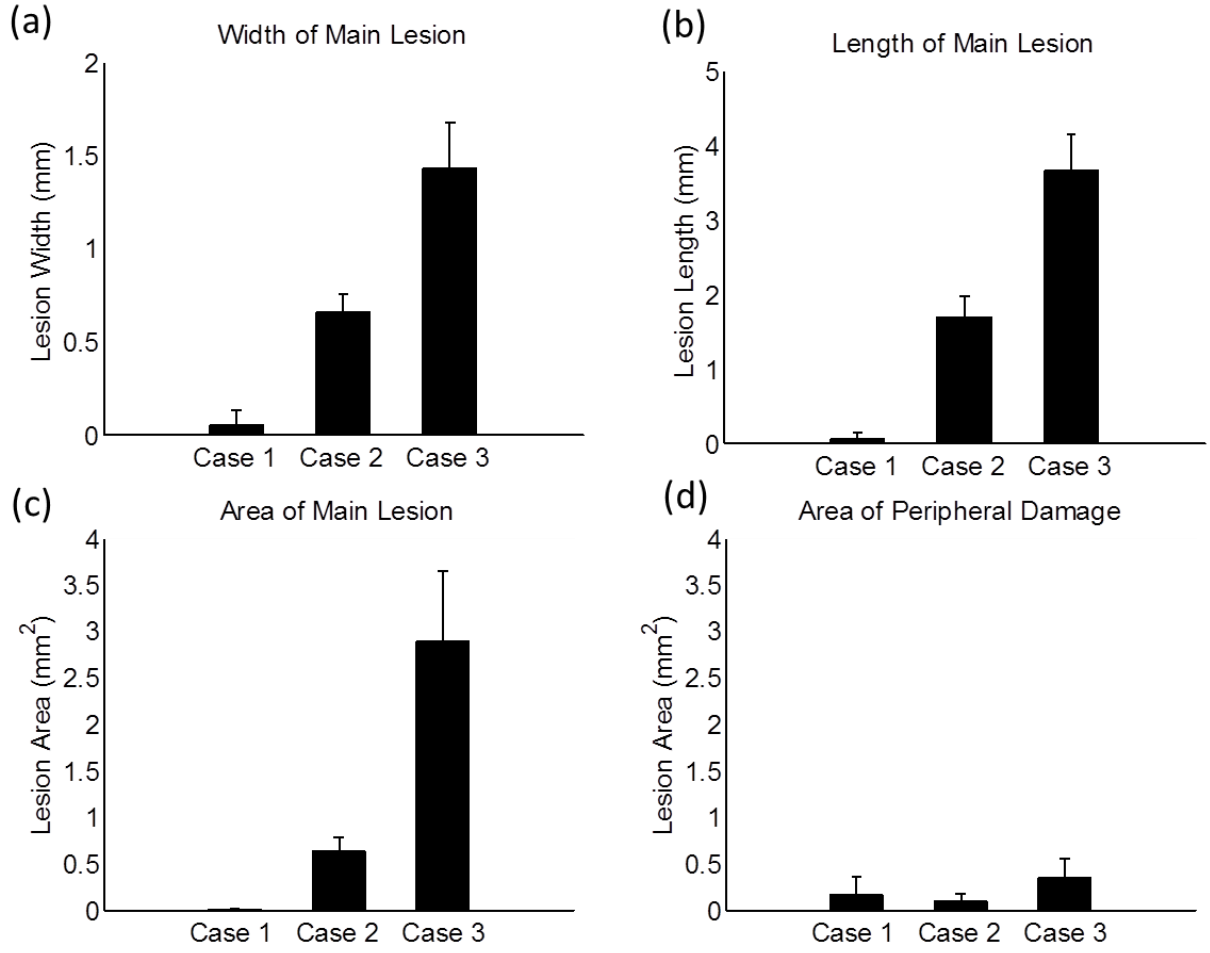

Figure 4.8 Quantitative results for the first set of the RBC phantom experiments. (a) Lesion width of the main lesion, (b) lesion length of the main lesion, (c) area of the main lesion, and (d) area of the peripheral damage.

4.3.2 Lesion Steering using Imaging Transducer

A total of 54 lesions were generated in RBC phantoms at nine imaging transducer steering distances (-1.2, -0.9, -0.6, -0.3, 0.0, 0.3, 0.6, 0.9, and 1.2 mm, six lesions for each case). Table 4.1 (Experimental Set 2) lists the applied pressures (P–) for the 345 kHz pump pulse and 5 MHz probe pulse. The applied focal P– (at 0.0 mm) of the 345 kHz pump pulse was kept the same for all cases and no steering was applied to the pump pulse. The driving voltage to the

imaging transducer was also kept the same and the measurement in Fig. 4.2(f) showed that there wasn't significant change in P– when the imaging transducer was steered from -1.2 to 1.2 mm.

Figure 4.9 shows representative bubble cloud and lesion images for these nine steering distances (to increase readability, only every other case is shown). As can be seen in the figure, when the imaging transducer was steered laterally, bubble clouds and lesions were also steered correspondingly. However, when the imaging transducer was steered farther than 0.6 mm, bubble clouds and lesions were no longer consistently generated, which could be an indication that the combined P– had decreased to below the intrinsic threshold. Since the P– for the imaging transducer remained at a similar level across different steering distances [shown in Fig. 4.2(f)], this decrease in combined P– was likely due to the P– for the 345 kHz pump pulse being lower at those locations (compared to 0.0 mm).

The quantitative results after lesion analysis (Figure 4.10) show that the size of the main lesion is at its maximum without any steering. It gradually decreases when the imaging transducer is steered laterally, and it approaches 0 when the imaging transducer is steered to ±1.2 mm. On the other hand, the area of the peripheral damage stays at a similar level across all steering distances, with 0 mm having the lowest average value.

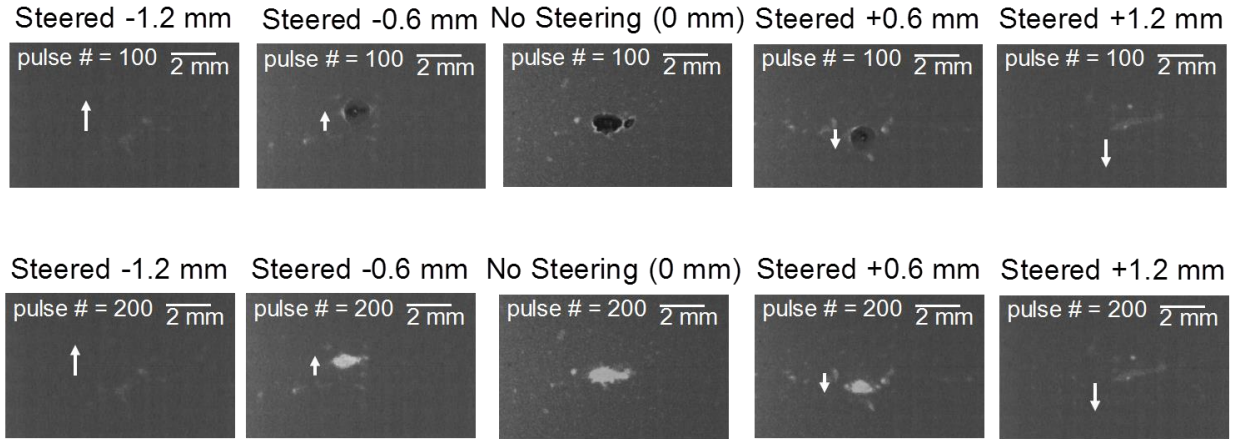

Figure 4.9 Representative bubble cloud (upper row) and lesion (lower row) images in the second set of the RBC phantom experiments wherein the imaging transducer was steered laterally. Only every other case (-1.2, -0.6, 0, +0.6, and +1.2 mm) is shown in order to increase readability. Dual-beam histotripsy pulses propagated from the left to the right of these images.

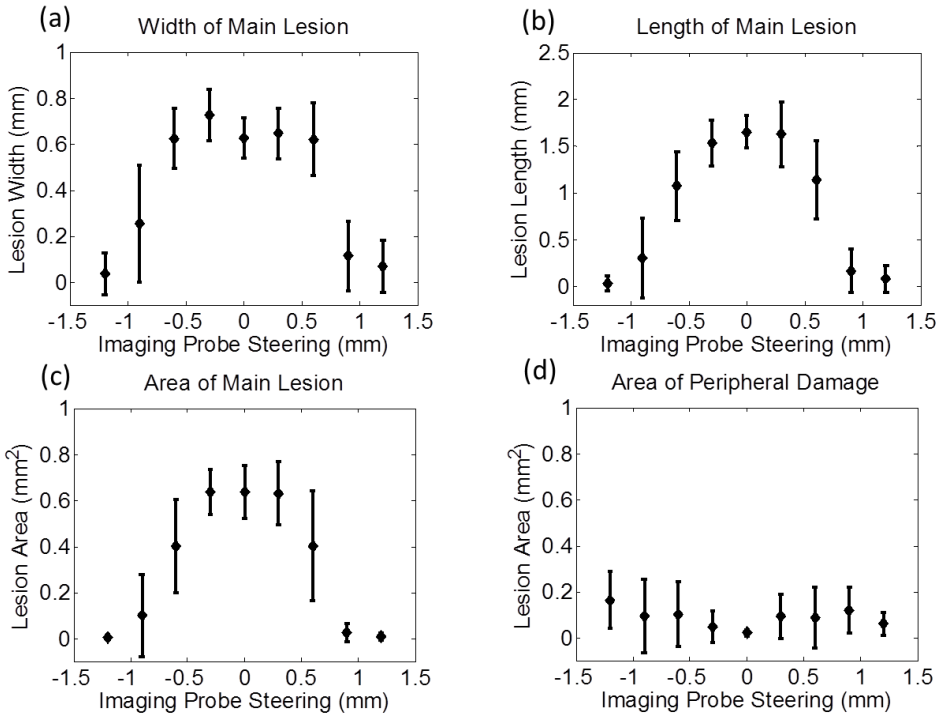

Figure 4.10 Quantitative results for the second set of the RBC phantom experiments wherein the imaging transducer was steered laterally. (a) Lesion width of the main lesion, (b) lesion length of the main lesion, (c) area of the main lesion, and (d) area of the peripheral damage.

Figure 4.11 shows the cavitation probability in the main lesion and periphery, quantified based on the number of pulses with bubble presence over the course of 200 applied pulses. As shown, the cavitation probability in the main lesion starts at almost 100% without any steering, it gradually decreases when the imaging transducer is steered laterally, and it finally approaches 0% when the imaging transducer is steered to ±1.2 mm. The cavitation probability in the periphery stays at a similar level across all steering distances.

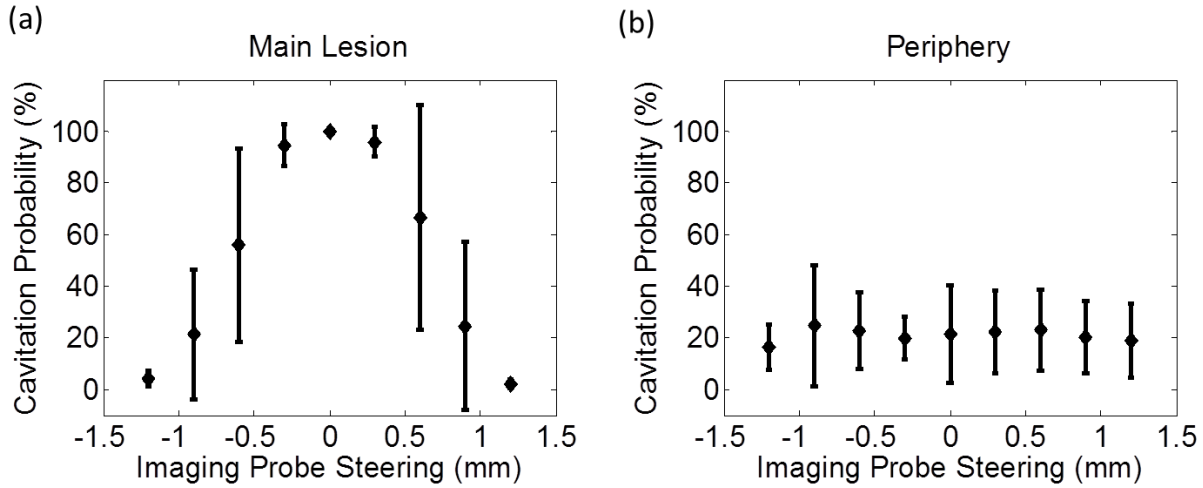

Figure 4.11 Cavitation probability in the (a) main lesion and (b) periphery as a function of the lateral steering distance of the imaging transducer.

4.4 Discussion

This chapter demonstrates that a sub-threshold high-frequency probe pulse provided by an imaging transducer can create lesion-producing bubble clouds when this probe pulse is "enabled" by a sub-threshold low-frequency pump pulse to exceed the intrinsic threshold (dual-beam histotripsy using an "imaging transducer"). The smallest reproducible lesion in this study (~ 0.7 × 1.7 mm) is somewhat larger than the smallest ones shown in our previous dual-beam histotripsy study [10] (~ 0.2 × 0.4 mm) where the probe pulse was 3 MHz. In the previous study, the probe pulse contributed ~ 60% of the combined P– whereas in this study the probe pulse only

contributes about 25 % of the combined P–. Thus, a higher proportion of the high-frequency probe pulse could lead to smaller lesions, which was also demonstrated in [10]. Additionally, the focal sizes of the pump and probe transducers in this study are much wider than the ones in [10], which could also increase the size of the smallest reproducible lesions. The –6 dB beamwidths of the transducers used in this study are 2.9 × 3.1 × 10.0 mm (345 kHz pump transducer) and 0.4 × 2.2 × 3.5 mm (5 MHz imaging transducer), while those in the previous study are 1.7 × 1.8 × 4.9 mm (500 kHz pump transducer) and 0.3 × 0.3 × 1.4 mm (3 MHz probe transducer).

Therefore, the current setup can be optimized in two ways in order to create a smaller and more precise lesion: 1) increase the contribution of high-frequency probe pulse and 2) use another high-frequency probe pulse with a narrower beamwidth. More specifically, using an imaging system with a higher power drive option can increase driving voltage to the imaging transducer, thus raising its focal pressure output. To provide a probe pulse with narrower beamwidth, we could select an imaging transducer with either higher frequency or larger profile (leading to a lower f-number). However, some trade-offs need to be considered since choosing a higher frequency imaging transducer would limit the penetration depth.

The results of the beam steering experiments showed that the bubble clouds and produced lesions could be steered by only steering the imaging transducer as long as the combined P– reached the intrinsic threshold (±0.6 mm steering capability in this current design). Since there were no significant changes in the output pressure of the imaging transducer when it was steered ±1.2 mm laterally [shown in Fig. 4.2(f)], the limitation in this steering range was solely contributed by the limited lateral beamwidth of the low-frequency pump transducer (*i.e.*, its P– dropped considerably at 1.2 mm away from the focus). This limitation can be improved by employing a pump transducer with a larger focal zone, which could be accomplished by a higher

f-number design with lower frequency elements. On the other hand, if the pump transducer has sufficient steering capability, we can also steer the low-frequency pump pulse along with the imaging transducer probe pulse.

As mentioned in the introduction, this dual-beam histotripsy using an imaging transducer can be useful in several situations, such as a transcostal application of pump pulses together with an intercostal application of imaging transducer pulses for transcostal tissue ablation, a transperineal application of pump pulses together with a transrectal application of imaging transducer pulses for prostatic tissue ablation, and a transcranial application of pump pulses together with an application of imaging transducer pulses through a small surgical opening for transcranial tissue ablation. However, when applying this technique to *in vivo* situations, two issues have to be considered: 1) a long propagation depth would still cause significant attenuation for the imaging transducer pulse even though it travels through a relatively low attenuation acoustic window and 2) the spatial and temporal alignment between the pump and probe pulses would need to be performed.

The attenuation probably would not significantly affect the transrectal application of the imaging transducer pulses since the anatomical distance between prostate and a transrectal imaging transducer in humans can be minimal. On the other hand, the propagation depths in transcranial and transcostal applications can be substantial enough to cause significant attenuation. For example, in transcostal liver ablation, the propagation depth averaged 4-6 cm for porcine subjects in one of our previous studies [11], and this could lead to an attenuation of about 76% for a 5MHz imaging transducer pulse (assuming linear attenuation using –0.5 dB/cm/MHz attenuation coefficient). The attenuation could be compensated by increasing the pressure output of the imaging transducer pulses by using an imaging system with a higher power drive option as

mentioned earlier in the discussion. Additionally, we can exchange precision in lesion formation for less attenuation by using a slightly lower-frequency imaging transducer. Another possible approach would be to use an endoscopic imaging probe for minimally invasive procedures.

For the alignment between pump and probe pulses, we can firstly perform the alignment in the free-field (water), and then apply corrections for *in vivo* situations. Using a large-focal-zone pump transducer would provide a larger target for imaging transducer alignment. Temporal corrections could be performed by surveying the thickness of the intervening tissue for the pump and imaging transducers separately and then compute the proper time delay between them. Additionally, the results in this study and the previous dual-beam histotripsy study [10] suggest that unpredictable focal damage due to temporal or spatial misalignment between pump and probe pules would be minimal since the intrinsic threshold would be obtained only through alignment.

4.5 Conclusion

An imaging transducer can create dense, lesion-producing bubble clouds when it is enhanced by a sub-threshold low-frequency pump pulse to exceed the intrinsic threshold (dual-beam histotripsy using an "imaging transducer"). Moreover, these lesion-producing bubble clouds could be steered by only steering the imaging transducer pulse, which could be realized using the beamformer of the ultrasound imaging system used to guide the therapy. This approach can be very useful in clinical applications where precise lesion formation is required through a highly attenuative and aberrative medium, especially when a small low-attenuation acoustic window is available for the imaging transducer.

4.6 References

[1] K.-W. Lin, T. L. Hall, Z. Xu, and C. A. Cain, "Histotripsy Lesion Formation with an Ultrasound Imaging Probe Enabled by a Low-Frequency Pump Transducer," *IEEE Trans Ultrason Ferroelectr Freq Control,* submitted Feb. 2014.

[2] M. R. Bailey, Y.-N. Wang, J. Simon, B. Cunitz, J. Harper, R. Hsi, F. Starr, M. Paun, O. Sapozhnikov, B. Dunmire, L. Crum, and M. Sorensen, "Acoustic radiation force to reposition kidney stones," *Proceedings of Meetings on Acoustics,* vol. 19, pp. -, 2013.

[3] M. D. Sorensen, M. R. Bailey, R. S. Hsi, B. W. Cunitz, J. C. Simon, Y. N. Wang, B. L. Dunmire, M. Paun, F. Starr, W. Lu, A. P. Evan, and J. D. Harper, "Focused ultrasonic propulsion of kidney stones: review and update of preclinical technology," *J Endourol,* vol. 27, pp. 1183-6, Oct 2013.

[4] J. D. Harper, M. D. Sorensen, B. W. Cunitz, Y.-N. Wang, J. C. Simon, F. Starr, M. Paun, B. Dunmire, H. D. Liggitt, A. P. Evan, J. A. McAteer, R. S. Hsi, and M. R. Bailey, "Focused Ultrasound to Expel Calculi from the Kidney: Safety and Efficacy of a Clinical Prototype Device," *The Journal of Urology,* vol. 190, pp. 1090-1095, 2013.

[5] A. D. Maxwell, T.-Y. Wang, L. Yuan, A. P. Duryea, Z. Xu, and C. A. Cain, "A Tissue Phantom for Visualization and Measurement of Ultrasound-Induced Cavitation Damage," *Ultrasound in Medicine & Biology,* vol. 36, pp. 2132-2143, 2010.

[6] J. E. Parsons, C. A. Cain, and J. B. Fowlkes, "Cost-effective assembly of a basic fiber-optic hydrophone for measurement of high-amplitude therapeutic ultrasound fields," *J Acoust Soc Am,* vol. 119, pp. 1432-40, Mar 2006.

[7] A. D. Maxwell, C. A. Cain, T. L. Hall, J. B. Fowlkes, and Z. Xu, "Probability of Cavitation for Single Ultrasound Pulses Applied to Tissues and Tissue-Mimicking Materials," *Ultrasound Med Biol,* vol. 39, pp. 449-465, 2013.

[8] T.-Y. Wang, Z. Xu, T. L. Hall, J. B. Fowlkes, and C. A. Cain, "An Efficient Treatment Strategy for Histotripsy by Removing Cavitation Memory," *Ultrasound in Medicine & Biology,* vol. 38, pp. 753-766, 2012.

[9] K.-W. Lin, Y. Kim, A. D. Maxwell, T.-Y. Wang, T. L. Hall, Z. Xu, J. B. Fowlkes, and C. A. Cain, "Histotripsy beyond the Intrinsic Cavitation Threshold using Very Short Ultrasound Pulses: Microtripsy," *IEEE Trans Ultrason Ferroelectr Freq Control,* vol. 61, pp. 251-265, 2014.

[10] K.-W. Lin, A. P. Duryea, Y. Kim, T. L. Hall, Z. Xu, and C. A. Cain, "Dual-Beam Histotripsy: A Low-Frequency Pump Enabling a High-Frequency Probe for Precise Lesion Formation," *IEEE Trans Ultrason Ferroelectr Freq Control,* vol. 61, pp. 325-340, 2014.

[11] E. Vlaisavljevich, Y. Kim, S. Allen, G. Owens, S. Pelletier, C. Cain, K. Ives, and Z. Xu, "Image-Guided Non-Invasive Ultrasound Liver Ablation Using Histotripsy: Feasibility Study in an In Vivo Porcine Model," *Ultrasound in Medicine & Biology*, vol. 39, pp. 1398-1409, 2013.

Chapter 5
Frequency Compounding: Synthesis of Monopolar Pulses

A majority component of this chapter is excerpted from a manuscript that has been accepted by *IEEE Transactions on Ultrasonics, Ferroelectric, and Frequency Control*. [1]

5.1 Introduction

In diagnostic ultrasound, broadband transducers capable of short acoustic pulse emission and reception are favorable since they can improve the axial resolution of the image and provide sufficient bandwidth for harmonic imaging and multi-frequency excitation [2]. The introduction of broadband transducers was made possible by engineering advances in ultrasound technology, including new piezoelectric materials with lower acoustic impedances and greater electromechanical coupling coefficients, as well as the construction of absorbing backing layers and optimized impedance matching layers [2, 3].

Short acoustic pulses have also demonstrated their advantages in histotripsy, a noninvasive, cavitation-based therapy which uses very short, high-pressure ultrasound pulses to generate a dense, energetic, lesion-producing bubble cloud [4-7]. Maxwell *et al* [8] showed that, when ultrasound pulses less than 2 cycles in length were applied, wherein shock scattering [9] was minimized, the generation of a dense bubble cloud only depended on some part of the negative pressure phase of the applied ultrasound pulses exceeding an "intrinsic threshold" of the medium (~26 – 30 MPa in most soft tissues). In chapter 3, we show that, using this intrinsic

threshold mechanism, the spatial extent of the produced lesions is well-defined and more predictable, and sub-wavelength reproducible lesions as small as half of the –6 dB beamwidth of the transducer could be generated ("microtripsy").

In this chapter, we propose a novel technique to synthesize extremely short, nearly "monopolar" (half-cycle) pulses using a transducer made from an array of broadband elements each operating at a distinct resonant frequency. The resultant acoustic pulse is synthesized by "frequency compounding," which combines the outputs of all the elements constructively in the target volume. In this transducer, each individual element is capable of generating short acoustic pulses (~1.5 cycles), at its own frequency, using a custom high voltage pulser. By adjusting time delays of individual frequency components to allow their principal peak negative pressures (P–) to align temporally, high peak negative pulses are generated by constructive addition, or compounding. Destructive interference occurs outside the peak-negative-overlapped temporal window, resulting in a good approximation of a monopolar (half-cycle) pulse with a "sharp" high-amplitude negative phase and low-amplitude "smeared out" positive phases preceding and following the negative phase (a "negative-polarity" pulse). A similar monopolar pulse with a sharp dominant positive phase (a "positive-polarity" pulse) can be generated in a similar way by constructive compounding of all principal peak positive pressures (P+) from all the elements.

The term, "frequency compounding," has been used for a technique in diagnostic ultrasound wherein speckle noise is reduced by averaging multiple images created from signals filtered at different center frequencies and bandwidths [10-15]. Acoustical speckle, which appears as a random mottled granular pattern, arises from the coherent interference of multiple echoes from small scatterers within a resolution volume of the imaging system [16, 17]. This speckle noise reduces the perceived resolution and degrades minimum detectable contrast level

[12]; moreover, it is time-independent so that the speckle noise cannot be reduced by temporal averaging [16]. Two major approaches, spatial compounding and frequency compounding, have been investigated to "smear out" the speckle effect, allowing the speckle noise to be averaged and minimized. Spatial compounding translates an imaging transducer and creates images from several angular views [18, 19], while frequency compounding uses images created at different center frequencies and bandwidths as discussed earlier. Although the frequency compounding technique proposed in this chapter shares the same name as the one for speckle noise reduction, their implementations are fundamentally different. Instead of averaging images created at various frequency bands, this proposed technique is implemented at the level of pulse generation wherein short acoustic pulses with various frequencies are concurrently launched and temporally aligned to approximate monopolar pulses.

Additionally, this proposed frequency compounding technique is different from some previous studies [20, 21] wherein ultrasound waves with 2^{nd}- harmonic superimposition onto the fundamental frequency is applied to enhance cavitation effects. The ultrasound waves used in these previous studies were either continuous waves or long pulses, and only two frequencies were used in the compounding process. In contrast, the technique proposed in this paper utilizes short acoustic pulses with a wide variety of frequencies to approximate extremely short monopolar pulses.

These monopolar pulses can be applicable in both therapeutic and diagnostic ultrasound. For histotripsy therapy, using monopolar pulses with a dominant negative phase can eliminate the shock-scattering effect because no high peak positive shock fronts develop. As a result, the generation of a dense bubble cloud will solely depend on the applied negative half cycle

exceeding the intrinsic threshold, making produced lesions even more controllable, predictable, and small by using the microtripsy approach [22].

In diagnostic ultrasound, using these monopolar waveforms as the transmit pulses could enhance axial resolution of the imaging due to the reduced pulse length (approximately half cycle). These monopolar pulses would also decrease and minimize speckle noise since these pulses have minimal oscillatory components, leading to less coherent constructive/destructive interference patterns in the image. These monopolar pulses will also be useful in pulse inversion contrast imaging. In pulse inversion imaging [23, 24], a sequence of two ultrasound pulses is transmitted with a proper time delay between the two, and the second pulse is an inverted copy of the first one. For a linear medium, the response to the second pulse will be an inverted copy of the response to the first one, and the summation of the two responses will become zero. For a nonlinear target, the response to the second pulse will not be the exact opposite of the response to the first pulse, leading to a non-zero summation. The produced pulse inversion image will then be a map of the nonlinearity of the imaged medium. The proposed monopolar pulses should amplify the difference between object responses when it is exposed to a negative-polarity pulse (mostly rarefactional) and a positive-polarity pulse (mostly compressional), thus increasing the sensitivity of the pulse inversion imaging.

In this chapter, a transducer consisting of 23 piezoceramic elements with various resonant frequencies (0.5, 1, 1.5, 2, and 3 MHz) was designed and assembled to investigate this frequency compounding technique for monopolar pulse generation. A fiber-optic probe hydrophone (FOPH) was used to measure the generated frequency-compounded pulses, and the ratios of P– to P+ for these pulses were then computed. A linear transient simulation using the Fast Object-Oriented C++ Ultrasound Simulator (FOCUS, developed by McGough et al. [25-29]) was also performed

to compare the FOPH-measured results with the simulation. The feasibility of applying these monopolar pulses in histotripsy was studied using red-blood-cell (RBC) tissue-mimicking phantoms. In this set of experiments, RBC phantoms were exposed to negative-polarity and positive-polarity pulses separately at various pressure levels. A total of 200 pulses were applied to each intended treatment location at a pulse repetition frequency (PRF) of 1 Hz.

5.2 Methods

5.2.1 Frequency-Compounding Transducer and Monopolar Pulse Generation

The frequency-compounding transducer (Figure 5.1) is composed of 23 elements with various resonant frequencies, 500 kHz (five elements), 1 MHz (four elements), 1.5 MHz (four elements), 2 MHz (three elements), and 3 MHz (seven elements). Each 500 kHz element consists of two 1 MHz, 20-mm-diameter, piezoceramic discs (PZ36, Ferroperm, Kvistgaard, Denmark) stacked together with epoxy. Each 1 MHz element consists of a single 1 MHz, 20-mm-diameter, piezoceramic disc (PZ36, Ferroperm). Each 1.5 MHz element consists of a single 1.5 MHz, 14 × 14 mm, rectangular piezoceramic plate (SM111, equivalent to modified PZT-4, Steiner and Martins, Miami, FL, USA). Each 2 MHz element consists of a single 2 MHz, 19-mm-diameter, piezoceramic disc (SM112, Steiner and Martins). Each 3 MHz element consists of a single 3MHz, 20-mm-diameter, piezoceramic disc (SM111, Steiner and Martins). The selection of these transducer elements was based on the availability of commercial piezoceramic elements, and during the selection process, the availability of particular frequencies had a higher priority than the shapes and sizes of the elements. Therefore, there is considerable room for optimization of any design for particular applications.

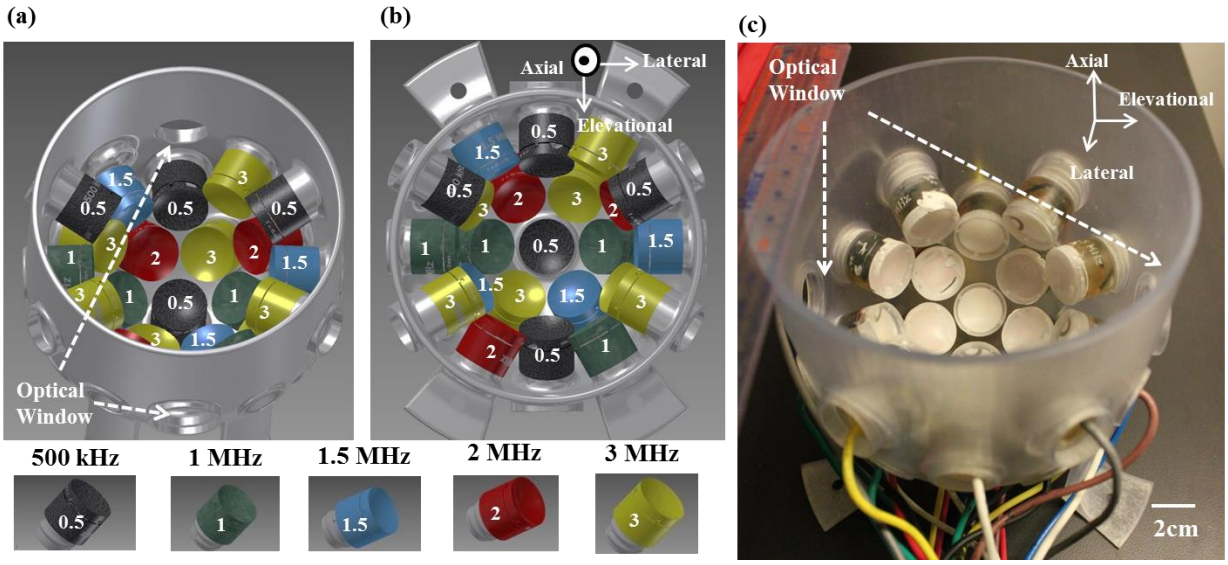

Figure 5.1 Illustrations of the frequency-compounding transducer. (a) and (b) are the drawings of the fully populated frequency-compounding transducer with elements color-coded for different frequencies. Besides color codes, individual elements are also labelled with the number showing its center frequency. (c) is a picture of the fully populated frequency-compounding transducer.

Each element was assembled in a plastic housing with a stereo-lithography-printed acoustic focusing lens of a geometric focal length of 40 mm (material: Accura® 60, 3D Systems, Rock Hill, SC, USA) and backed with slow-curing marine epoxy (A-side Resin 314 + B-side Slow Hardener 143, TAP Plastics, Inc., San Leandro, CA, USA). Elements across different frequencies had the same acoustic focusing lens and backing material, while their matching layers varied and are listed in the following: 1) 500 kHz and 1 MHz elements: no matching layer (PZ36 elements have a relatively low acoustic impedance) and 2) 1.5, 2, and 3 MHz elements: a mixture of Hysol® epoxy (1C-LV, Loctite® , Westlake, OH, USA) and copper wire cloth (80 × 80 mesh size for 1.5 MHz, 100 × 100 mesh size for 2 MHz, 200 × 200 mesh size for 3 MHz, McMaster-Carr, Aurora, OH, USA). These elements were then confocally aligned and had a common geometric focus at 40 mm. The scaffold had 23 threaded receptacles and they were arranged as follows: 1) one bottom receptacle with 0 degrees tilt angle, 2) one (the first) ring of 6

receptacles with 37 degrees tilt angle, 3) another (the second) ring of 6 receptacles with 64 degrees tilt angle, 4) another (the third) ring of 6 receptacle with 85 degrees tilt angle, and 5) another (the fourth) ring of 4 receptacle with 103 degrees tilt angle. A specific order for populating these elements was adopted to ensure that adjacent elements did not have the same frequency. This was done to reduce nonlinear propagation effects that occur when acoustic waves of the same frequency propagate closely in space and interfere constructively. Additionally, the frequency-compounding transducer has two diametrically opposed optical windows located at a similar height of the third ring to allow for optical imaging at the geometric focus. The overall frequency-compounding transducer is approximately hemispherical (the fourth ring had 103 degrees tilt angle), and it has an aperture size (diameter) of 65 mm, a focal length of 40 mm, and an approximate packing density of 54%.

A custom high voltage pulser with 23 parallel channels was used to drive the frequency-compounding transducer. The pulser was connected to a field-programmable gated array (FPGA) development board (Altera DE1, Terasic Technology, Dover, DE, USA) specifically programmed for frequency compounding pulse generation. This setup allowed each element to individually output short pulses (1.5 cycles, with only one large negative phase) with desired amplitudes and time delays. A fiber-optic probe hydrophone (FOPH) [30] was used to calibrate and measure acoustic output of the frequency-compounding transducer.

The generation of monopolar pulses with a dominant negative phase (negative-polarity pulses) was achieved by adjusting the arrival times of individual frequency components to allow their principal negative phase peaks to arrive at the focus of the transducer concurrently. In this situation, destructive interference occurs elsewhere in space and time, leading to a diminution of the peak positive pressure of the combined ultrasound pulse. For the generation of monopolar

pulses with a dominant positive phase (positive-polarity pulses), driver pulses for the individual elements were inverted, resulting in ultrasound pulses with a single principal positive phase from each element. The arrival times of individual frequency components were then adjusted to allow their principal positive phase peaks to arrive at the focus concurrently.

5.2.2 Linear Transient Simulation with the Fast Object-Oriented C++ Ultrasound Simulator (FOCUS)

A linear transient simulation for the temporal acoustic waveform and the two-dimensional (2D) spatial pressure fields of this frequency-compounding transducer was performed using the Fast Object-Oriented C++ Ultrasound Simulator (FOCUS, developed by McGough *et al* [25-29]). FOCUS is a cross-platform (Windows, Linux, and Mac OS X) "free-ware" and consists of MATLAB (MathWorks, Natick, MA, USA) user interface and object-oriented C++ computation core. The simulation in this paper was performed with Version 0.760 of FOCUS on version R2011a of MATLAB. In the simulation, "spherical shells" with a diameter of 20 mm and a focal length of 40 mm were selected to represent all of elements in the frequency-compounding transducer. In order to emulate actual temporal focal waveforms better, two-cycle, "Hanning-weighted tone-burst pulses" were chosen as the excitation pulses, together with desired frequencies and amplitudes. Specific time delays were selected to allow the peaks of their negative phases to arrive at the focus concurrently. The sampling frequencies in time and space domain were chosen to be 4×10^7 samples / second (40 MHz) and 5×10^4 samples / meter, respectively. The FOCUS function "transient_pressure" was used to calculate the transient pressure field using the fast near-field method and time-space decomposition [25-29]. The returned result was a four-dimensional (4D) matrix with three dimensions in space and one

dimension in time. With proper indexing of the returned 4D matrix, temporal waveforms at the focus and 2D peak negative and positive pressure fields were readily obtained.

5.2.3 Experiments in red-blood-cell (RBC) Phantoms and Lesion Analysis

Experiments were performed on RBC tissue-mimicking phantoms to investigate the feasibility of these frequency-compounded monopolar pulses in histotripsy therapy. Two experimental configurations were evaluated, where one demonstrated an exposure to negative-polarity pulses and the other showed an exposure to positive-polarity pulses. Each intended treatment region was exposed with 200 pulses at a PRF of 1 Hz, and a single-focal-point exposure was performed. Applied pressure levels are listed in Table 5.1. The procedures described in this study were approved by the University of Michigan's Committee on Use and Care of Animals.

Table 5.1 Peak negative pressures and time delays for capturing bubble cloud images in the RBC phantom experiments of the frequency compounding study

Experimental Set	Case	Individual Focal P– with Attenuation Correction* (MPa)					Focal P– of Linearly Summed Signal with Attenuation Correction** (MPa)	Time Delay For Capturing Bubble Cloud Images (μs)
		500 kHz	1 MHz	1.5 MHz	2 MHz	3 MHz		
1	1	7.4	5.4	4.9	3.8	8.8	27.6	4
	2	8.9	6.7	6.1	4.6	10.4	33.2	6
	3	10.2	8.0	7.2	5.2	11.9	39.0	9
	4	12.0	9.4	8.2	5.8	13.4	44.3	12
	5	13.7	10.5	9.1	6.2	14.7	48.9	17
Experimental Set	Case	Individual Focal P+ with Attenuation Correction* (MPa)					Focal P+ of Linearly Summed Signal with Attenuation Correction** (MPa)	Time Delay For Capturing Bubble Cloud Images (μs)
		500 kHz	1 MHz	1.5 MHz	2 MHz	3 MHz		
2	1	7.5	5.2	5.9	5.5	11.9	30.4	4
	2	9.9	7.1	8.4	7.1	15.0	36.8	6
	3	11.8	9.1	11.3	8.4	17.5	42.3	9
	4	14.0	11.5	14.0	9.8	21.2	48.0	12

* The pressure levels were corrected by the attenuation contributed by the plastic gel holders and agarose hydrogels. The attenuation contributed by the plastic gel holders was measured using the FOPH. The attenuation contributed by agarose hydrogels was calculated using a reported attenuation coefficient [31] and assuming linear propagation.
** The P– here was not directly measured, and it was the P– of the linearly summed signal. The attenuation correction here was the same as the ones in *.

The RBC tissue-mimicking phantom can be used for the visualization and quantification of cavitation-induced damage [31]. In this study, fresh canine blood was obtained from adult research canine subjects in an unrelated study. An anticoagulant solution of citrate-phosphate-dextrose (CPD) (C7165, Sigma-Aldrich, St. Louis, MO, USA) was added to the blood with a CPD-to-blood ratio of 1:9 (v:v), and the blood was kept at 4℃ and used within 3 weeks. The agarose-saline mixture consists of low-melting-point agarose powder (AG-SP, LabScientific, Livingston, NJ, USA) and 0.9% saline at an agarose-to-saline ratio of 1:100 (w:v). In this study, in order to make phantoms with a thinner central RBC layer, the preparation for this layer differed slightly from the protocol described in a previous paper [31]. During the solidification process of the central layer, the gel holder was mounted vertically such that the agarose-saline-RBC mixture trickled down the previous agarose-saline-only casting while solidifying into a very thin central layer (~ 60 – 100 μm). Additionally, the ratio of RBCs to agarose-saline mixture was increased to 33:67 from 5:95 (v:v) in order to provide sufficient image contrast between treated and untreated regions.

The experimental setup for RBC experiments is illustrated in Figure 5.2. The frequency-compounding transducer was placed in a glass tank (40.6 × 20.3 ×25.4 cm) filled with degassed water. For the visualization of the generated bubble clouds and their resulting damages in RBC phantoms, a digital, 1.3-megapixel, CMOS, mono-color camera (PN: FL3-U3-13Y3M-C, Flea® 3, PointGrey, Richmond, BC, Canada) was positioned perpendicularly to the frequency-compounding transducer facing one of its optical windows. A Nikon 4X microscope objective with extension tubes was attached to the camera to provide additional image magnification, giving the captured images a resolution of approximately 4.1 μm per pixel. For back-lit

illumination, a pulsed white-light LED was placed on the opposing optical window of the transducer. In order to maintain the synchronization of image capturing and the delivery of the frequency-compounded pulses, the camera and the LED light source received trigger signals from the FPGA board. Two images were acquired for every delivered frequency-compounded pulse, one (bubble cloud image) at the time when the maximal spatial extent of the bubble cloud was observed (see Table 5.1 for exact timing), and the other (lesion image) at 500 ms after the arrival of the pulse, where only cavitation-induced damage in the RBC phantom was observed. The exposure time was set at 2 μs for every captured image. The RBC phantoms were mounted on a 3-axis motorized positioner (Griffin Motion, Holly Springs, NC, USA) and submerged in the frequency-compounding transducer with an orientation for axial-lateral-plane treatments.

The captured optical images were post-processed with MATLAB using a method similar to those described in previous papers [31, 32]. The lesion image was firstly converted to a gray-scale image, and then converted to a binary image using a threshold calculated based on the mean intensity of the lesion. The regions with brightness exceeded the threshold would become "1 (white)" in the binary image and be considered "damaged;" whereas, the regions with brightness below the threshold would become "0 (black)" and be considered "intact." In order to exclude noise in the camera sensor and pre-existing isolated small white regions due to RBC layers being not 100% uniform, white regions that were smaller than 120 pixels (corresponding to regions less than 25 μm in radius) were excluded from the damage zone. By counting the number of the white pixels in the binary image and converting it to actual size with the help of a pre-captured scale image, lesion sizes in the axial (lesion length) and lateral (lesion width) directions were determined.

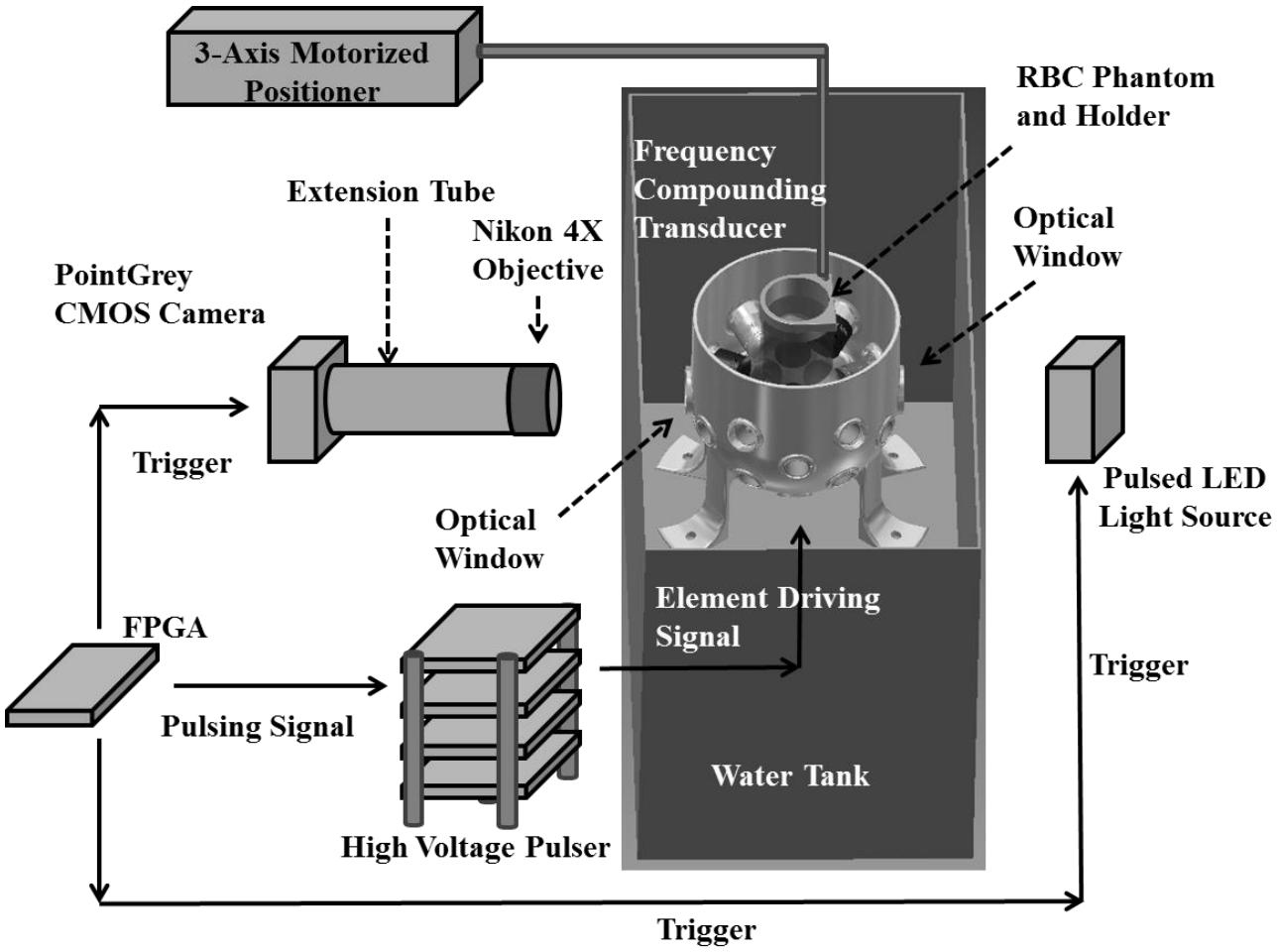

Figure 5.2 An illustration of the overall experimental setup in RBC phantom experiments.

5.3 Results

5.3.1 The Generation of "Negative-Polarity" Pulses

Representative measured and simulated temporal focal waveforms in the free-field for each frequency component are plotted in Figure 5.3 (the results from the FOPH measurement and the FOCUS simulation are both plotted). As can be seen from the FOPH-measured waveforms [Figure 5.3(a1) – (a5)], the FPGA-controlled high voltage pulser enabled individual frequency components to output short acoustic pulses with only one principal negative phase. Note that the actual waveforms were slightly longer than the simulated waveforms.

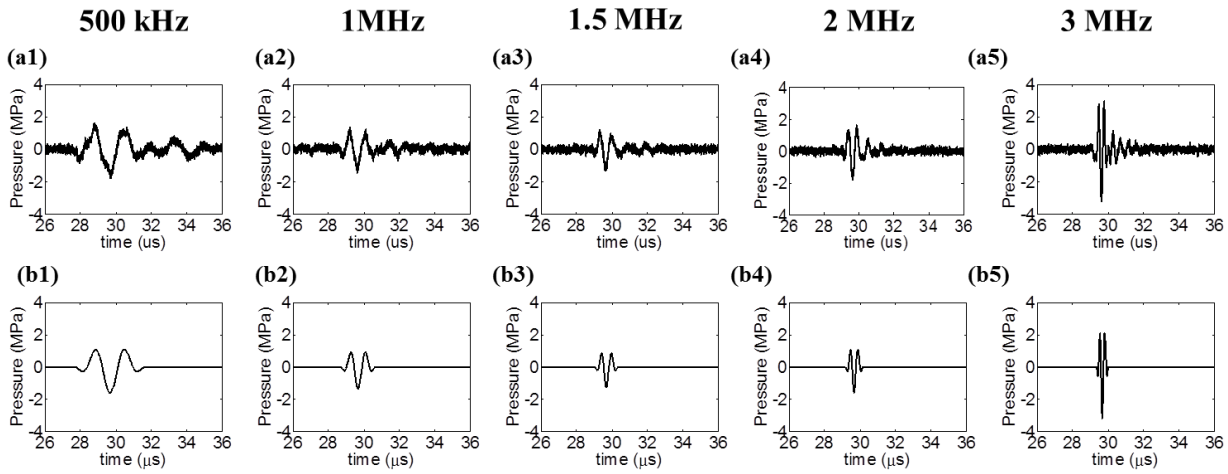

Figure 5.3 Representative temporal focal waveforms for individual frequency components of the frequency-compounding transducer. (a1) – (a5) are waveforms measured directly with the FOPH in the free-field. (b1) – (b5) are simulated waveforms using the FOCUS simulation tool. In the simulation, the amplitudes of the source excitation pulses were adjusted to approximately match the focal pressures of the FOPH-measured waveforms.

The generation of negative-polarity pulses was investigated by adjusting the arrival times of individual frequency components to allow their peaks of principal negative phases to arrive at the focus concurrently. Figure 5.4 plots representative free-filed waveforms of a negative-polarity pulse, including a waveform directly measured using the FOPH with all frequency components firing simultaneously [Figure 5.4(a)], a frequency spectrum of the directly-measured waveform [Figure 5.4(b)], a linearly summed waveform using FOPH-measured waveforms of individual frequency components [Figure 5. 4(c)], and a simulated waveform using the FOCUS simulation tool [Figure 5. 4(d)]. These pulses were generated using the same amplitudes for individual frequency components as those in Figure 5.3. As can be seen in Figure 5.4, an approximately monopolar pulse with a dominant negative phase was generated, and the ratio of P– to P+ was 4.68 for the directly measured waveform (3.52 for the linearly summed waveform and 9.16 for the simulated waveform). The temporal full-width-half-maximum (FWHM) of the

negative phase of the directly measured waveform was 0.17 µs, which was in between FWHMs of the principal negative phases of the 2MHz (0.19 µs) and 3MHz (0.11 µs) components.

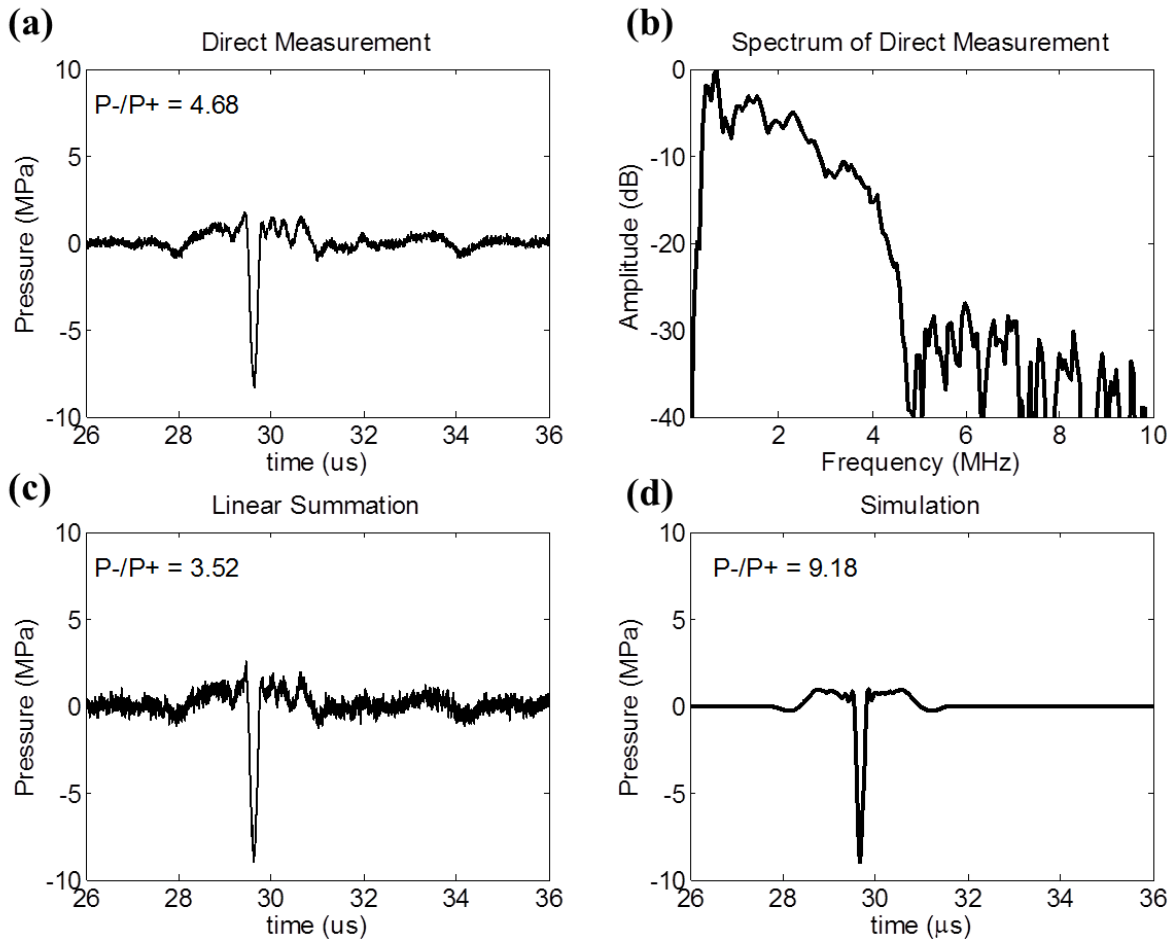

Figure 5.4 Representative waveforms of a frequency-compounded pulse with a dominant negative phase (a "negative-polarity" pulse). (a) The temporal focal waveform in the free-field that was directly measured using the FOPH. (b) The frequency spectrum of the directly measured waveform. (c) The temporal focal waveform in the free-field that was linearly summed using individual FOPH-measured waveforms of different frequency components [the same as the ones in Figures 5.3(a1) – (a5)]. (d) A temporal focal waveform that was obtained from linear simulation using the FOCUS with the same excitation amplitudes as those in Figures 5.3(b1) – 3(b5).

Figure 5.5 shows representative 2D spatial pressure fields for a negative-polarity pulse, including pressure fields directly measured using the FOPH with all frequency components firing simultaneously [Figures 5.5(a1) – (a4)] and pressure fields simulated using the FOCUS

simulation tool [Figures 5.5(b1) – (b4)]. In this 2D pressure field measurement, the negative-polarity pulse had a P– of 18.1 MPa at the focus, and the 2D pressure fields for P– and P+ were both normalized to the absolute value of the P– at the focus. The relative amplitudes of individual frequency components were the same as the ones used in Figures 5.3 and 5.4. As can be seen in Figure 5.5, the FOPH-measured 2D P– pressure fields show a good agreement with the FOCUS-simulated 2D P– pressure fields, in both the axial-lateral and transverse planes. The 2D P+ pressure fields had a slight variation between FOPH-measured ones and FOCUS-simulated ones, possibly due to the limitation in sensitivity of the FOPH (predominantly noise signal at low pressure level) or the actual pulses not being ideally short as the pulses used in the simulation (as seen in Figure 5.3).

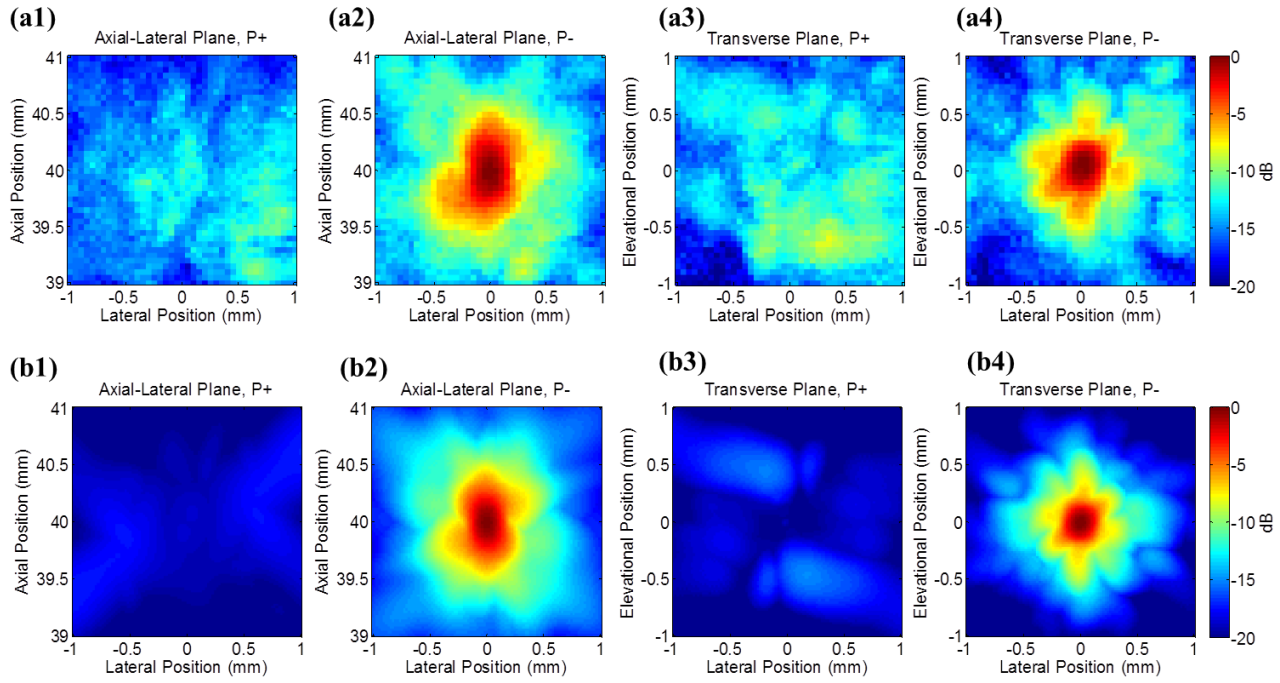

Figure 5.5 Representative 2D spatial pressure fields for a negative-polarity pulse. (a1) – (a4) are directly measured 2D pressure fields using the FOPH. (b1) – (b4) are simulated 2D pressure fields using the FOCUS. The sub-figures in the 1st and 2nd columns plot 2D pressure fields of P+ and P– in the axial-lateral plane, respectively. The sub-figures in the 3rd and 4th columns plot 2D pressure fields of P+ and P– in the transverse plane, respectively. All of the sub-figures were normalized to the spatially-maximal P–, and displayed in dB scale.

5.3.2 The Generation of "Positive-Polarity" Pulses

In this section, all driving signals were inverted, resulting in an inversion of the output focal waveforms. Figure 5.6 plots representative FOPH-measured and simulated temporal focal waveforms for individual frequency components. Here, inverting the output of the FPGA-controlled high voltage pulser enabled each frequency component to output short acoustic pulses with only one principal positive phase. The arrival times of each frequency component were than adjusted to allow their positive phase peaks to arrive at the focus simultaneously. This resulted in a nearly monopolar pulse with a dominant positive phase (a positive-polarity pulse), shown in Figure 5.7, and the ratio of P+ to P– was 4.74 for the directly measured waveform.

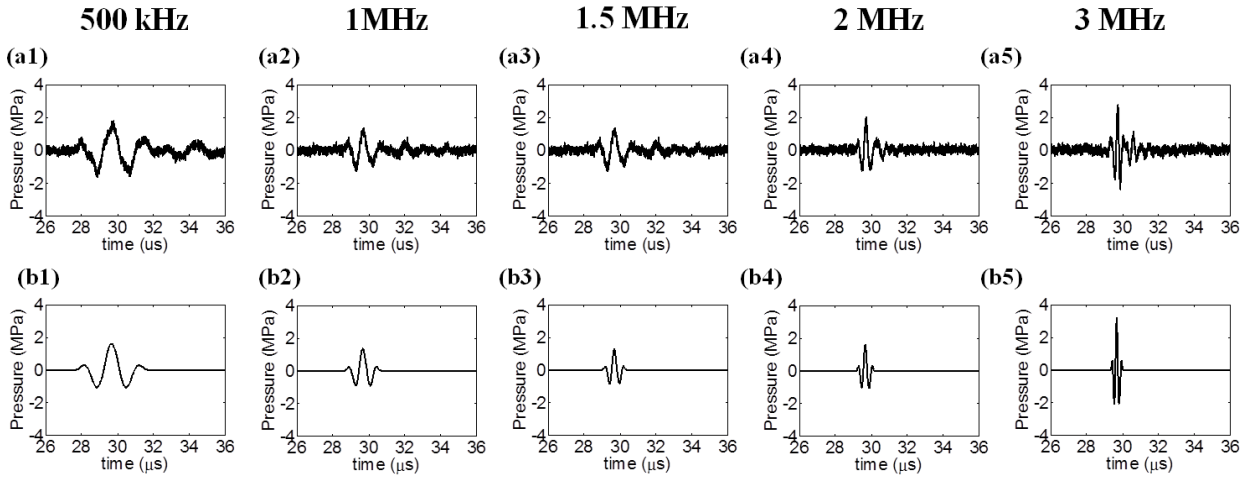

Figure 5.6 Representative temporal focal waveforms for individual frequency components when driving signals are inverted. (a1) – (a5) are waveforms measured directly with the FOPH in the free-field. (b1) – (b5) are simulated waveforms using the FOCUS simulation tool. In the simulation, the amplitudes of the source excitation pulses were adjusted to approximately match the focal pressures of the FOPH-measured waveforms.

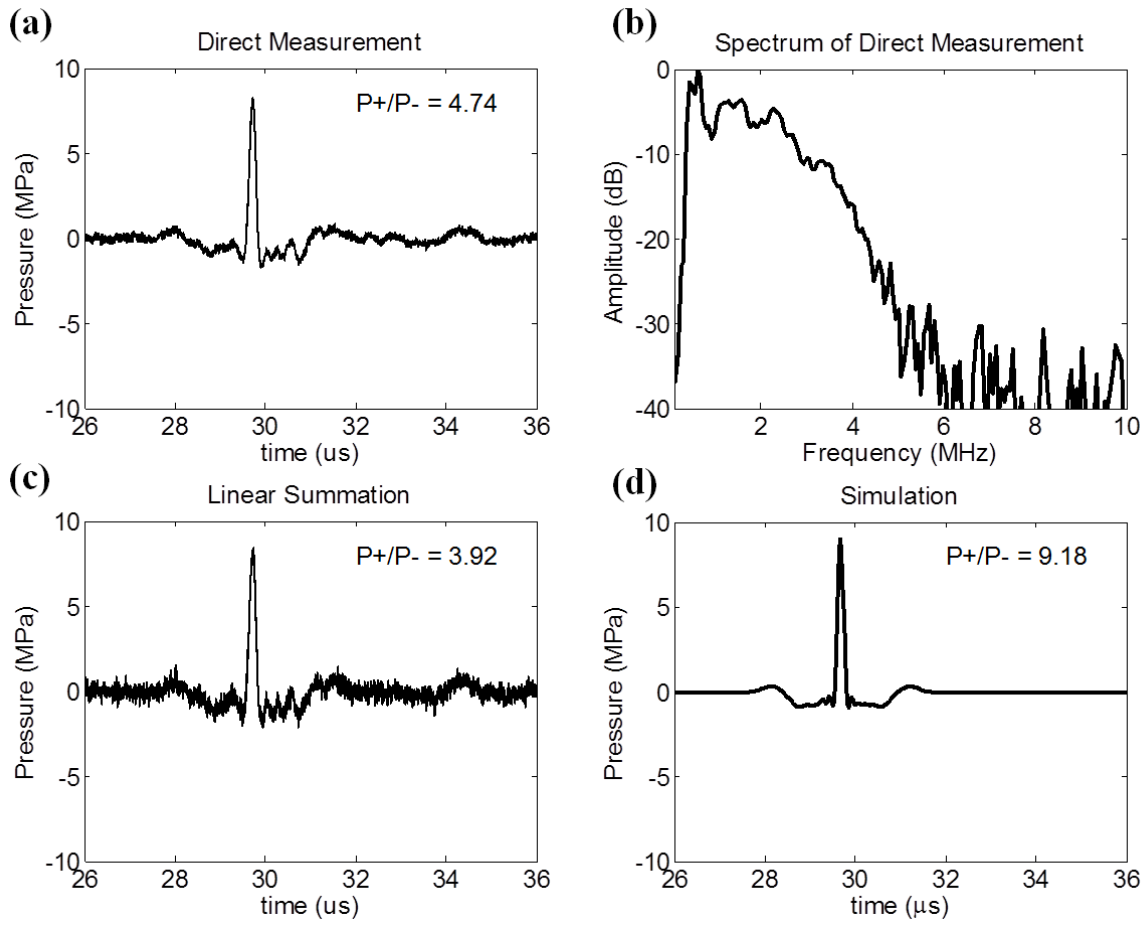

Figure 5.7 Representative waveforms of a frequency-compounded pulse with a dominant positive phase (a "positive-polarity" pulse). (a) The temporal focal waveform in the free-field that was directly measured using the FOPH. (b) The frequency spectrum of the directly measured waveform. (c) The temporal focal waveform in the free-field that was linearly summed using individual FOPH-measured waveforms of different frequency components [the same as the ones in Figures 5.6(a1) – (a5)]. (d) A temporal focal waveform that was obtained from linear simulation using the FOCUS with the same excitation amplitudes as those in Figures 5.6(b1) – (b5).

5.3.3 Negative-Polarity and Positive-Polarity Pulses at Various Pressure Levels

Figures 5.8(a) and (b) plot the ratio of P– to P+ as a function of applied pressure level (P–) for negative-polarity pulses and a representative temporal focal waveform at P– = 20 MPa, respectively. Figures 5.8(c) and (d) plot the ratio of P+ to P– as a function of applied pressure level (P+) for positive-polarity pulses and a representative temporal focal waveform at P+ = 23

MPa, respectively. As can be seen in Figures 5.8(a) and (c), when the pressure levels increased, the ratio of P– to P+ for the negative-polarity pulses decreased slightly, while the ratio of P+ to P– for the positive-polarity pulses increased slightly. This was possibility due to an increase in nonlinear propagation effects at higher pressure levels. In Figures 5.8(b) and (d), the directly measured waveforms had a good agreement with the linearly summed waveforms at a higher pressure level for both negative-polarity and positive-polarity pulse cases, and the shapes of these directly measured waveforms did not significantly deviate from the ones measured at a lower pressure level [Figures 5.4(a) and 5.7(a)]. Figures 5.9 shows the individual temporal focal waveforms for each frequency component at the pressure level used in Figures 5.8(b) and (d). Their shapes were similar to those at a lower pressure level shown in Figures 5.3(a1) – (a5) and Figures 5.6(a1) – (a5).

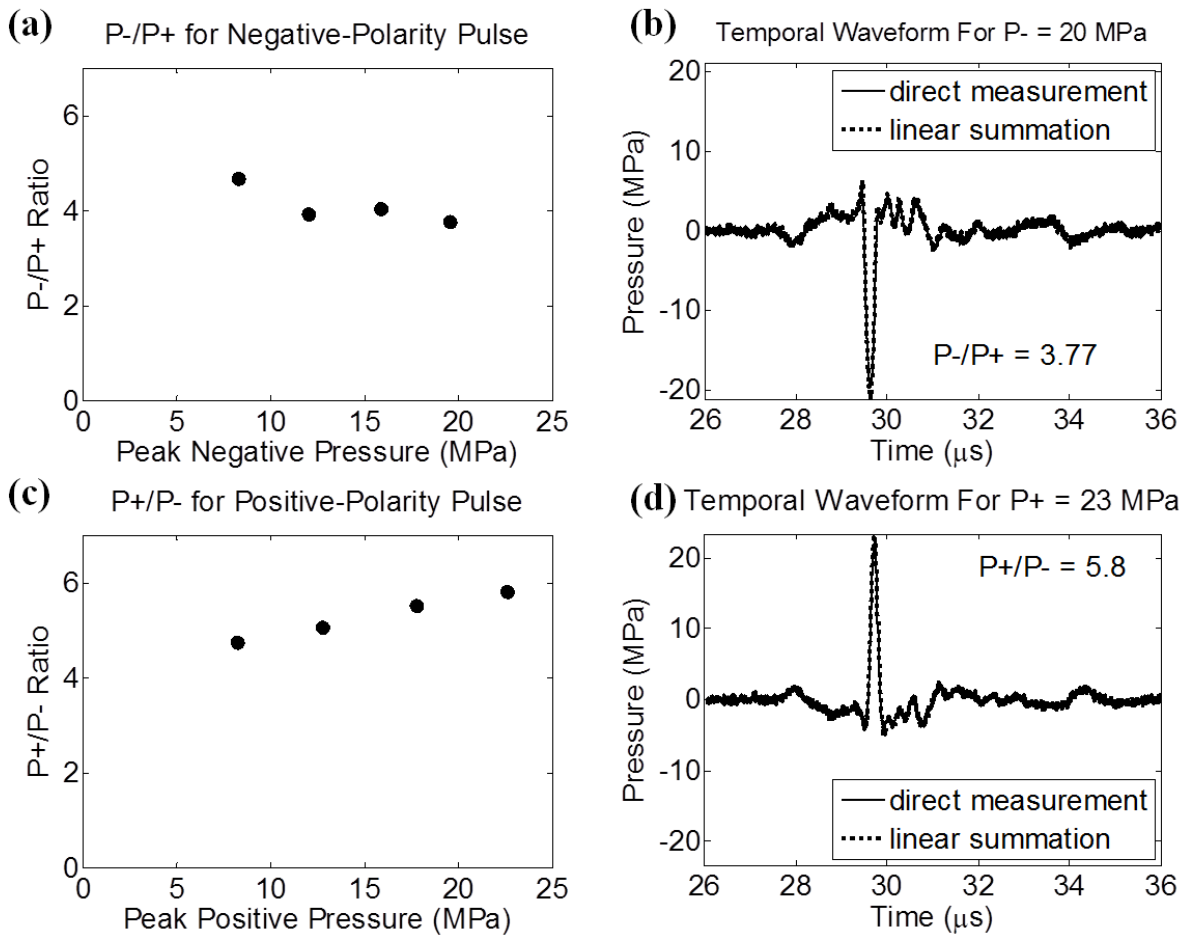

Figure 5.8 (a) The ratio of P– to P+ as a function P– in the negative-polarity pulse case. (b) Representative temporal waveforms for the negative-polarity pulse at P– = 20 MPa, measured by the FOPH in the free-field. (c) The ratio of P+ to P– as a function P+ in the positive-polarity pulse case. (d) Representative temporal waveforms for the positive-polarity pulse at P+ = 23 MPa, measured by the FOPH in the free-field.

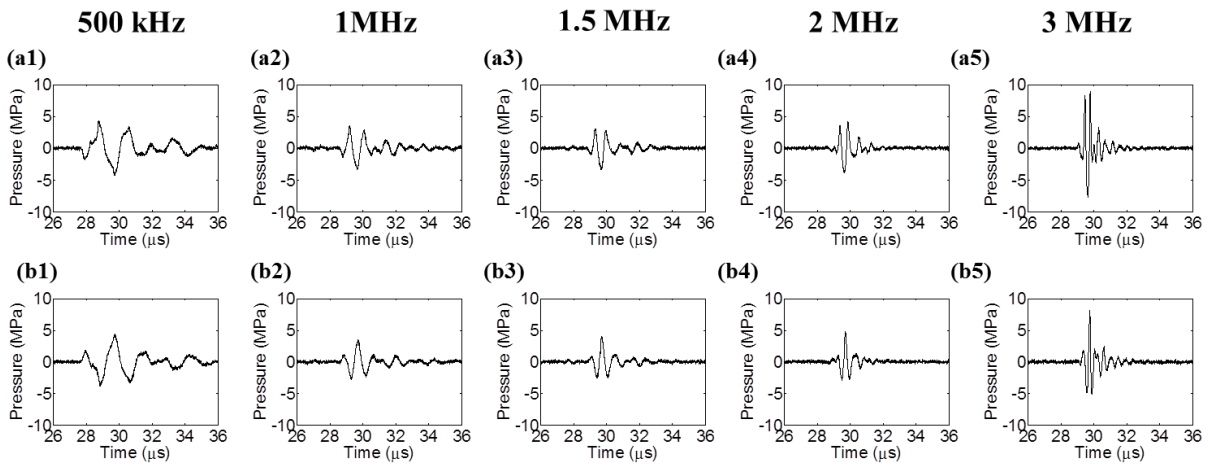

Figure 5.9 Representative temporal focal waveforms (directly measured by FOPH) for individual frequency components at the highest pressure used in Figure 5.8 (b) and (d). (a1) – (a5) are the individual waveforms used for the synthesis of the negative-polarity pulse in Figure 5.8(b). (b1) – (b5) are the individual waveforms used for the synthesis of the positive-polarity pulse in Figure 5.8(d).

5.3.4 RBC Phantom Experiments

A total of 30 lesions in RBC phantoms were generated using negative-polarity pulses (six for each pressure level listed in Table 5.1), and their representative lesion and bubble cloud images are shown in Figure 5.10. Their quantified lesion sizes in the lateral and axial directions are plotted in Figures 5.11(a) and (b), respectively. As can be seen from Figures 5.10 and 5.11, cavitation-induced lesions were observed in RBC phantoms using negative-polarity pulses with P– exceeding the intrinsic threshold, and the sizes of the generated lesions and the bubble clouds increased as the applied P– increased.

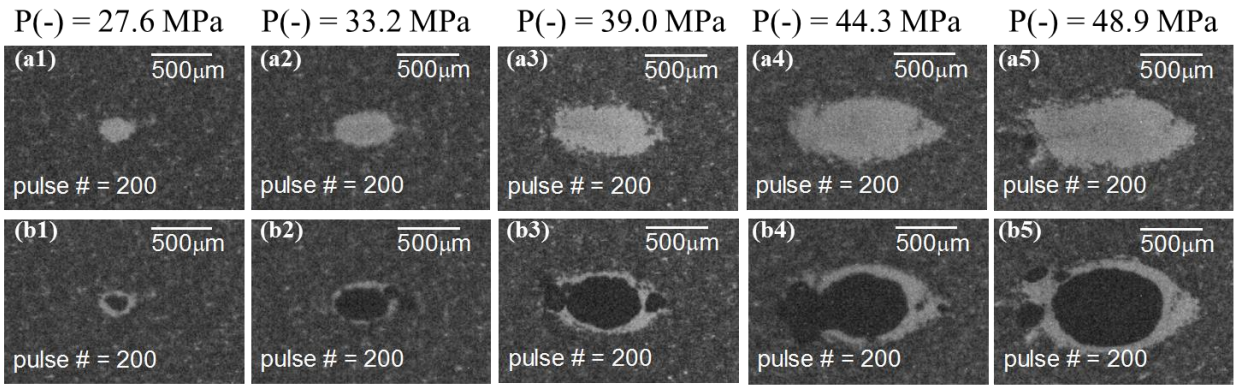

Figure 5.10 Representative lesion [(a1) – (a5)] and bubble cloud [(b1) – (b5)] images in the RBC phantom experiments that used negative-polarity pulses. All the images were taken in the axial-lateral plane of the transducer and the pulses propagated from left to the right.

A total of 20 locations in RBC phantoms were exposed to positive-polarity pulses (five for each pressure level listed in Table 5.1), and their representative lesion and bubble cloud images are shown in Figure 5.12. As can be seen, neither lesions nor bubble clouds were generated using positive-polarity pulses with P+ ranging from 30 to 50 MPa. No further quantitative lesion analysis was performed for the positive-polarity pulse case.

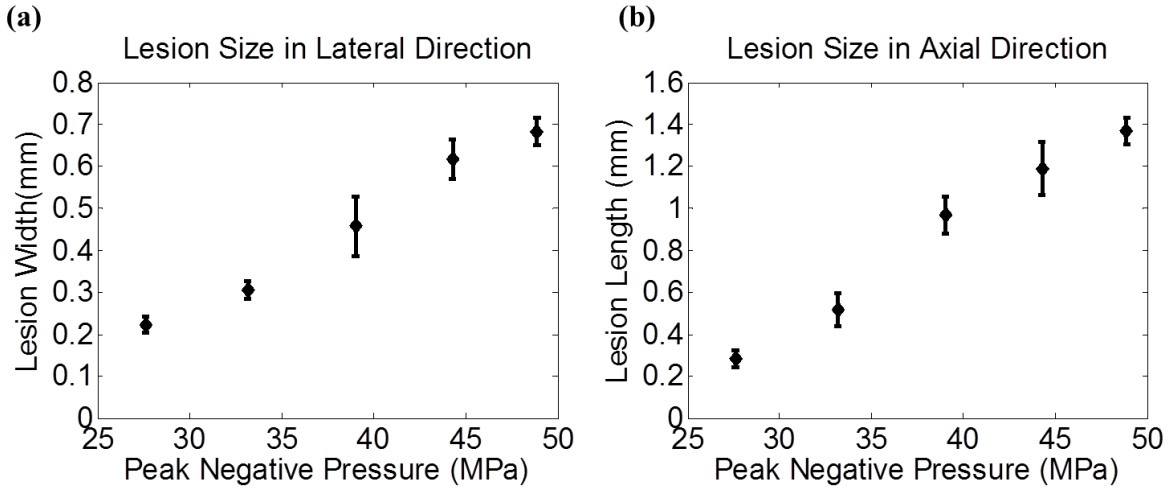

Figure 5.11 Quantitative results for the RBC phantom experiments that used negative-polarity pulses. (a) Quantified lesion size in the lateral direction (b) Quantified lesion size in the axial direction.

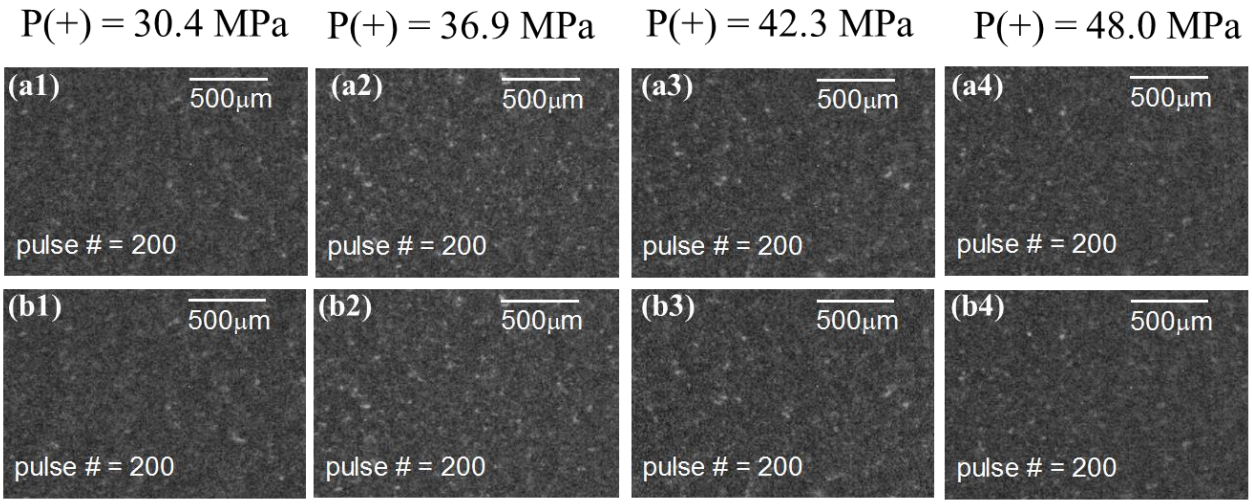

Figure 5.12 Representative lesion [(a1) – (a4)] and bubble cloud [(b1) – (b4)] images in the RBC phantom experiments that used positive-polarity pulses. No bubble clouds were observed and no lesions were formed for the positive-polarity pulse configuration. All of the images were taken in the axial-lateral plane of the transducer and the pulses propagated from left to the right.

5.4 Discussion

In this paper, the synthesis of approximately "monopolar" pulses was demonstrated using a frequency-compounding transducer consisting of elements with five different resonant frequencies, 0.5, 1, 1.5, 2, and 3 MHz. By properly adjusting time delays for individual frequency components, monopolar pulses could be generated. The temporal FWHM of the generated negative-polarity pulse was between the temporal FWHMs of the negative phases of the 2MHz and 3MHz components. This shows that the frequency of the combined monopolar pulses lies within the frequency span of the individual frequency components. The frequency components (500 kHz to 3 MHz) in this particular frequency-compounding transducer were selected since these frequency components are the ones commonly used in histotripsy therapy, although this selection could be optimized for different applications. For example, for imaging or therapy at deeper targets with highly attenuative and aberrative intervening tissue, lower

frequency components could be chosen to generate lower-frequency monopolar pulses. On the other hand, for superficial and microscopic targets, higher frequency components could be applied to generate higher-frequency monopolar pluses.

Moreover, the generation of monopolar pulses was limited to the focus of the frequency-compounding transducer, which was less than 1 × 1 × 2 mm (lateral × elevational × axial) in the present design. The design of this highly focused transducer (with an f-number of close to 0.5, hemispherical) was chosen to allow the transducer to provide sufficient output pressure for histotripsy therapy (this current transducer is capable of generating a combined P– of 100 MPa, estimated by linear summation). In diagnostic ultrasound, this level of output pressure would be prohibited due to safety concerns; therefore, a different approach could be adopted when designing a frequency-compounding transducer for imaging purposes. This new design will favor a higher f-number configuration in order to cover an imaging plane more uniformly. For some applications, an ideal array transducer would emit an approximate plane wave consisting of a frequency-compounded monopolar pulse. This could be a linear array with subsets of modules wherein each module alone can generate monopolar pulses with a desired frequency. Some recent advances in transducer array manufacturing [33-35] involving microfabrication of piezoceramic components using microstereolithography could benefit the development of frequency-compounding transducers consisting of microelements with various resonant frequencies.

Figures 5.4 and 5.7 show that the ratio of P– and P+ varied among directly measured, linearly summed, and FOCUS simulated pulses (FOCUS simulated >> directly measured > linearly summed). The variation between simulation and the actual pulses measured by the FOPH is likely because the pulses used in the simulation (2-cycle hanning-weighted tone bursts)

do not exactly match the actual output pulses of the transducer elements. However, the waveform shapes and 2D field patterns from simulation were in general agreement with the FOPH measurements. Therefore, simulations provide useful information for future transducer design, e.g. choosing optimal transducer geometry and element frequencies.

As shown in Figure 5.8, when the combined pressure level increased from ~8 MPa to ~23 MPa, the ratio of P– to P+ for negative-polarity pulses slightly decreased and the ratio of P+ to P– for positive-polarity pulses slightly increased. This slight change in P– and P+ ratios is likely due to nonlinear propagation. However, this nonlinear effect was minimal at the highest pressure level shown in Figure 5.8, since the changes in the ratios of P– and P+ values were minimal and the shapes of the focal pressure waveforms did not deviate significantly from those at the lower pressure level shown in Figures 5.4(a) and 5.7(a). By comparing individual waveforms at this higher pressure level (Figure 5.9) to those at the lower pressure level [Figures 5.3(a1) – (a5) and 5.6(a1) – (a5)], we could also infer that nonlinear effects were minimal at the combined pressure level of ~23 MPa. Separating elements with the same resonant frequency in the current transducer arrangement likely contributes to this minimal development of nonlinearity.

Some high f-number transducers are limited in peak amplitude by "nonlinear saturation" wherein higher order harmonics are attenuated rapidly as driving signals increase. Frequency-compounding arrays result in minimal constructive interference outside the focal zone, thus reducing nonlinear saturation effects. This could be very important in some therapy systems where anatomy limits aperture size.

In this study, the time delays and excitation amplitudes for each element were specifically selected to generate monopolar pulses; however, a different set of time delays and excitation amplitudes could be chosen to synthesize different types of waveforms. Figure 5.13 demonstrates

some example waveforms that can be generated by the current 23-element frequency-compounding transducer. Figure 5.13(a) shows an FOPH-measured bi-phasic pulse with a negative-polarity pulse followed by a positive-polarity pulse (an "NP" pulse), and Figure 5.13(b) shows an FOPH-measured bi-phasic pulse with a positive-polarity pulse followed by a negative-polarity pulse (a "PN" pulse). Figure 5.13(c) shows an FOPH-measured "square" pulse, and Figure 5.13(d) is a simulation for Figure 5.13(c) using the FOCUS simulation tool. Although this "square" pulse generated by the current transducer does not resemble an ideal square pulse, the shape would improve considerably with a transducer using a large number of elements consisting of a much wider variety of frequencies.

As demonstrated in Figure 5.13, this frequency compounding technique for monopolar pulse generation can be generalized to a broader concept, namely, "waveform synthesis" using frequency compounding. We hypothesize that, with a sufficient number of elements and a wide variety of frequencies, a frequency-compounding transducer can potentially become an arbitrary waveform synthesizer by appropriately adjusting time delays and excitation amplitudes to individual elements. Moreover, optimization algorithms would allow more precise choice of time delays, frequencies, and array geometries for synthesis of waveforms needed for unique applications. We plan to conduct further studies, simulations, and analytical approaches to test this hypothesis.

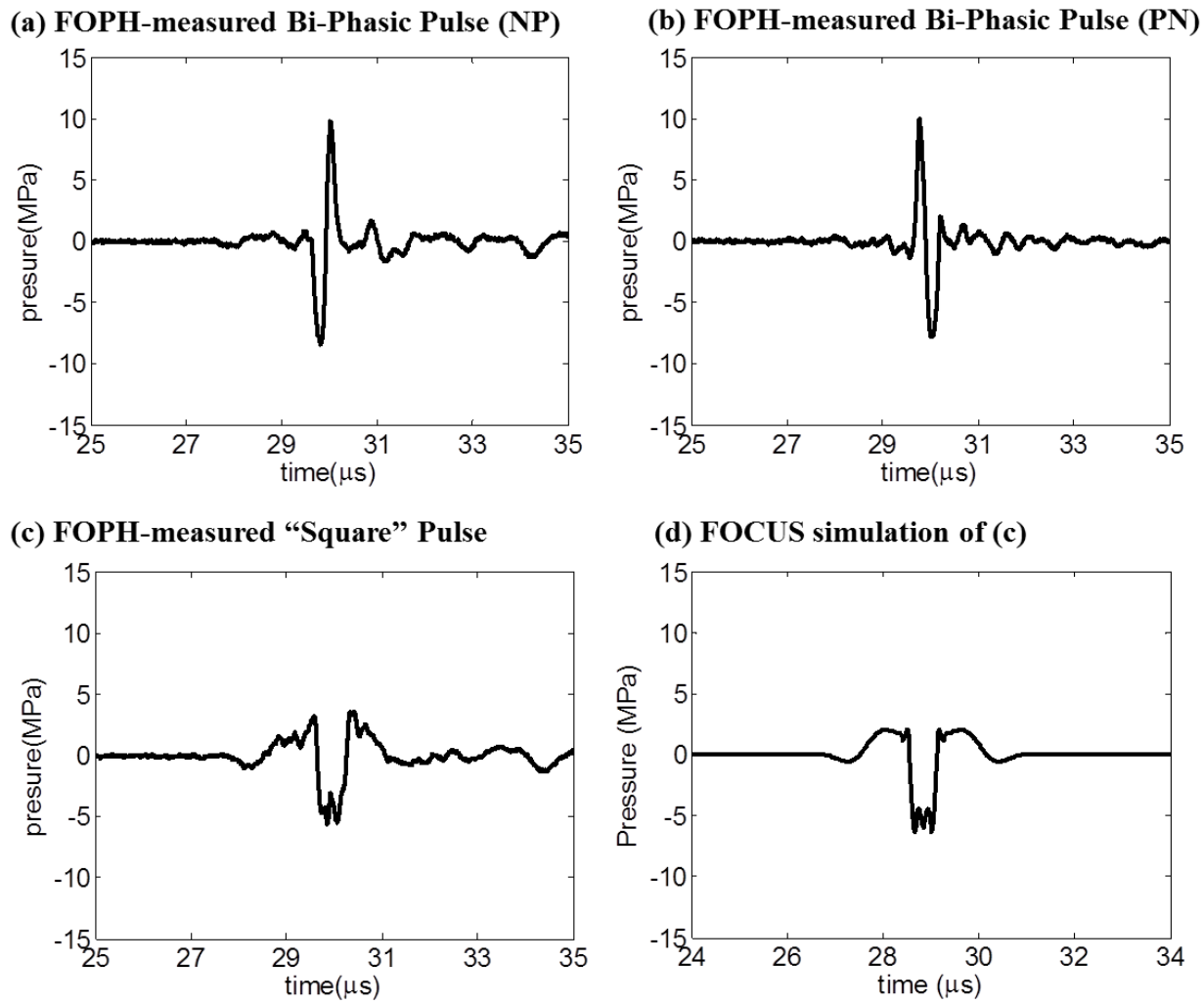

Figure 5.13 Example waveforms that can be synthesized by the current frequency-compounding transducer. (a) A bi-phasic pulse which has a negative-polarity pulse followed by a positive-polarity pulse (an "NP pulse"). (b) A bi-phasic pulse which has a positive-polarity pulse followed by a negative-polarity pulse (a "PN pulse"). (c) A "square" pulse which temporally stacks three negative-polarity pulses together with 180 ns delay in between. (d) A FOCUS-simulated pulse for the case of (c).

5.5 Conclusion

This chapter demonstrated the feasibility of generating (nearly) monopolar pulses using a frequency-compounding transducer. By adjusting time delays for individual frequency components and allowing their principal peak negatives to arrive at the focus of the transducer

concurrently, monopolar pulses with a dominant negative phase (negative-polarity pulses) can be generated. By inverting the excitation pulses to individual elements, monopolar pulses with a dominant positive phase (positive-polarity pulses) can also be generated. Negative-polarity pulses with combined P– higher than the intrinsic threshold were capable of creating cavitational lesion-producing bubble clouds, and the size of corresponding lesions in RBC phantoms increased with increased combined P–. Neither cavitational bubble clouds nor lesions were generated in RBC phantoms using positive-polarity pulses with combined P+ similar to the level of the combined P– used in the RBC phantom experiments with negative-polarity pulses. Therefore, Frequency Compounding allows the generation of highly functional histotripsy pulses with no extraneous complicating features.

These frequency-compounded monopolar pulses can have many applications in both ultrasonic imaging and therapy. Non-coherent excitation pulses, for example, would minimize speckle in ultrasound images. Moreover, a frequency-compounding transducer can potentially become an arbitrary waveform synthesizer given that the transducer has a sufficient number of elements with a wide range of resonant frequencies.

5.6 References

[1] K.-W. Lin, T. L. Hall, R. J. McGough, Z. Xu, and C. A. Cain, "Synthesis of Monopolar Ultrasound Pulses for Therapy: The Frequency-Compounding Transducer," *IEEE Trans Ultrason Ferroelectr Freq Control,* accepted Jan. 2014.

[2] T. A. Whittingham, "Broadband transducers," *European Radiology,* vol. 9, pp. S298-S303, 1999/11/01 1999.

[3] M. Claudon, F. Tranquart, D. Evans, F. Lefèvre, and J. Correas, "Advances in ultrasound," *European Radiology,* vol. 12, pp. 7-18, 2002/01/01 2002.

[4] Z. Xu, A. Ludomirsky, L. Y. Eun, T. L. Hall, B. C. Tran, J. B. Fowlkes, and C. A. Cain, "Controlled ultrasound tissue erosion," *IEEE Trans Ultrason Ferroelectr Freq Control,* vol. 51, pp. 726-36, Jun 2004.

[5] J. E. Parsons, C. A. Cain, G. D. Abrams, and J. B. Fowlkes, "Pulsed cavitational ultrasound therapy for controlled tissue homogenization," *Ultrasound Med Biol,* vol. 32, pp. 115-29, Jan 2006.

[6] W. W. Roberts, "Focused ultrasound ablation of renal and prostate cancer: current technology and future directions," *Urol Oncol,* vol. 23, pp. 367-71, Sep-Oct 2005.

[7] A. P. Duryea, A. D. Maxwell, W. W. Roberts, Z. Xu, T. L. Hall, and C. A. Cain, "In vitro comminution of model renal calculi using histotripsy," *IEEE Trans Ultrason Ferroelectr Freq Control,* vol. 58, pp. 971-80, May 2011.

[8] A. D. Maxwell, C. A. Cain, T. L. Hall, J. B. Fowlkes, and Z. Xu, "Probability of Cavitation for Single Ultrasound Pulses Applied to Tissues and Tissue-Mimicking Materials," *Ultrasound Med Biol,* vol. 39, pp. 449-465, 2013.

[9] A. D. Maxwell, T. Y. Wang, C. A. Cain, J. B. Fowlkes, O. A. Sapozhnikov, M. R. Bailey, and Z. Xu, "Cavitation clouds created by shock scattering from bubbles during histotripsy," *J Acoust Soc Am,* vol. 130, pp. 1888-98, Oct 2011.

[10] P. A. Magnin, O. T. von Ramm, and F. L. Thurstone, "Frequency compounding for speckle contrast reduction in phased array images," *Ultrasonic Imaging,* vol. 4, pp. 267-281, 1982.

[11] H. E. Melton, Jr. and P. A. Magnin, "A-mode speckle reduction with compound frequencies and compound bandwidths," *Ultrasonic Imaging,* vol. 6, pp. 159-173, 1984.

[12] G. E. Traney, J. W. Allison, S. W. Smith, and O. T. von Ramm, "A quantitative approach to speckle reduction via frequency compounding," *Ultrasonic Imaging,* vol. 8, pp. 151-164, 1986.

[13] G. E. Trahey, J. W. Allison, S. W. Smith, and O. T. Von Ramm, "Speckle Pattern Changes with Varying Acoustic Frequency: Experimental Measurement and Implications for Frequency Compounding," in *IEEE 1986 Ultrasonics Symposium*, 1986, pp. 815-818.

[14] G. Cincotti, L. Giovanna, and M. Pappalardo, "Frequency decomposition and compounding of ultrasound medical images with wavelet packets," *Medical Imaging, IEEE Transactions on,* vol. 20, pp. 764-771, 2001.

[15] J. R. Sanchez and M. Oelze, "An ultrasonic imaging speckle-suppression and contrast-enhancement technique by means of frequency compounding and coded excitation," *Ultrasonics, Ferroelectrics and Frequency Control, IEEE Transactions on,* vol. 56, pp. 1327-1339, 2009.

[16] P. N. T. Wells and M. Halliwell, "Speckle in ultrasonic imaging," *Ultrasonics,* vol. 19, pp. 225-229, 1981.

[17] J. M. Thijssen and B. J. Oosterveld, "Speckle and Texture in Echography: Artifact or Information?," in *IEEE 1986 Ultrasonics Symposium*, 1986, pp. 803-810.

[18] G. E. Trahey, S. W. Smith, and O. T. von Ramm, "Speckle Pattern Correlation with Lateral Aperture Translation: Experimental Results and Implications for Spatial Compounding," *Ultrasonics, Ferroelectrics and Frequency Control, IEEE Transactions on,* vol. 33, pp. 257-264, 1986.

[19] R. Entrekin, J. Jago, and S. Kofoed, "Real-Time Spatial Compound Imaging: Technical Performance in Vascular Applications," in *Acoustical Imaging*. vol. 25, M. Halliwell and P. T. Wells, Eds., ed: Springer US, 2002, pp. 331-342.

[20] S.-i. Umemura, K.-i. Kawabata, and K. Sasaki, "In vitro and in vivo enhancement of sonodynamically active cavitation by second-harmonic superimposition," *J Acoust Soc Am,* vol. 101, pp. 569-577, 1997.

[21] S. Yoshizawa, J. Yasuda, and S.-i. Umemura, "High-speed observation of bubble cloud generation near a rigid wall by second-harmonic superimposed ultrasound," *J Acoust Soc Am,* vol. 134, pp. 1515-1520, 2013.

[22] K.-W. Lin, Y. Kim, A. D. Maxwell, T.-Y. Wang, T. L. Hall, Z. Xu, J. B. Fowlkes, and C. A. Cain, "Histotripsy beyond the Intrinsic Cavitation Threshold using Very Short Ultrasound Pulses: Microtripsy," *IEEE Trans Ultrason Ferroelectr Freq Control,* vol. 61, pp. 251-265, 2014.

[23] D. H. Simpson, C. Chien Ting, and P. N. Burns, "Pulse inversion Doppler: a new method for detecting nonlinear echoes from microbubble contrast agents," *Ultrasonics, Ferroelectrics and Frequency Control, IEEE Transactions on,* vol. 46, pp. 372-382, 1999.

[24] P. J. A. Frinking, A. Bouakaz, J. Kirkhorn, F. J. Ten Cate, and N. de Jong, "Ultrasound contrast imaging: current and new potential methods," *Ultrasound Med Biol,* vol. 26, pp. 965-975, 2000.

[25] J. F. Kelly and R. J. McGough, "A time-space decomposition method for calculating the nearfield pressure generated by a pulsed circular piston," *Ultrasonics, Ferroelectrics and Frequency Control, IEEE Transactions on,* vol. 53, pp. 1150-1159, 2006.

[26] D. Chen and R. J. McGough, "A 2D fast near-field method for calculating near-field pressures generated by apodized rectangular pistons," *J Acoust Soc Am,* vol. 124, pp. 1526-1537, 2008.

[27] J. F. Kelly and R. J. McGough, "Transient Fields Generated by Spherical Shells in Viscous Media," *AIP Conference Proceedings,* vol. 1113, pp. 210-214, 2009.

[28] R. J. McGough, "Rapid calculations of time-harmonic nearfield pressures produced by rectangular pistons," *J Acoust Soc Am,* vol. 115, pp. 1934-1941, 2004.

[29] R. J. McGough, T. V. Samulski, and J. F. Kelly, "An efficient grid sectoring method for calculations of the near-field pressure generated by a circular piston," *J Acoust Soc Am,* vol. 115, pp. 1942-1954, 2004.

[30] J. E. Parsons, C. A. Cain, and J. B. Fowlkes, "Cost-effective assembly of a basic fiber-optic hydrophone for measurement of high-amplitude therapeutic ultrasound fields," *J Acoust Soc Am,* vol. 119, pp. 1432-40, Mar 2006.

[31] A. D. Maxwell, T.-Y. Wang, L. Yuan, A. P. Duryea, Z. Xu, and C. A. Cain, "A Tissue Phantom for Visualization and Measurement of Ultrasound-Induced Cavitation Damage," *Ultrasound in Medicine & Biology,* vol. 36, pp. 2132-2143, 2010.

[32] T.-Y. Wang, Z. Xu, T. L. Hall, J. B. Fowlkes, and C. A. Cain, "An Efficient Treatment Strategy for Histotripsy by Removing Cavitation Memory," *Ultrasound in Medicine & Biology,* vol. 38, pp. 753-766, 2012.

[33] A. Bertsch, S. Jiguet, and P. Renaud, "Microfabrication of ceramic components by microstereolithography," *Journal of Micromechanics and Microengineering,* vol. 14, p. 197, 2004.

[34] H. R. Chabok, Z. Chi, S. Alagha, C. Yong, Z. Qifa, and K. K. Shung, "Development of a digital micro-manufacturing process for high frequency ultrasound transducers," in *Ultrasonics Symposium (IUS), 2010 IEEE*, 2010, pp. 666-669.

[35] P. Singh, L. S. Smith, M. Bezdecny, M. Cheverton, J. A. Brewer, and V. Venkataramani, "Additive manufacturing of PZT-5H piezoceramic for ultrasound transducers," in *Ultrasonics Symposium (IUS), 2011 IEEE International*, 2011, pp. 1111-1114.

Chapter 6
Applications in Metastatic Lymph Node Ablation

6.1 Introduction

This chapter studies the application of precise lesion formation in metastatic lymph node ablation. Lymph nodes are small oval-shaped organs that serve as filters or traps for foreign particles within the lymphatic system. They are tightly packed by lymphocytes and macrophages with a supporting meshwork that consists of several types of fibrous tissue. When a local malignant tumor starts metastasizing, the lymphatic system is believed to be the most common route. If a patient has a tumor that is diagnosed to be possibly metastatic, a surgical removal of the regional nodal system will be performed followed by a pathological examination for cancer staging [1-4]. For example, axillary lymph node dissection (ALND) was once considered to be a standard procedure for invasive breast cancer [1, 5]. However, this lymph node removal procedure is often accompanied by substantial side effects, such as lymphedema (lymph fluid build-up) [6] and an increased risk of infection and inflammation.

Among the various regional nodal systems, sentinel lymph nodes (SLNs) are the hypothetical lymph nodes or groups of lymph nodes that first receive the drainage from the primary metastatic tumors. During the last two decades, sentinel lymph node biopsy (SLNB), in which only the sentinel lymph nodes are removed and examined for cancer staging, has been studied and demonstrated to achieve the same therapeutic outcome as conventional lymph node dissection while decreasing its side effects for early stage breast cancer patients [7-10]. In a five

year study with 936 female breast cancer patients [9, 10], the prevalence of lymphedema was reported as 5% (objective measurement) or 3% (patient perception) for patients who had SLNB alone versus 16% (objective measurement) or 27% (patient perception) of patients who had both SLNB and ALND. In order to successfully conduct SLNB, several techniques have been used and developed for the detection of SLNs: 1) the injection of vital blue dyes that provide visual identification of draining lymphatic channels as well as SLNs during surgery, 2) lymphoscintigraphy, the injection of radioactive particles that can be detected either prior to surgery by a gamma camera or intraoperatively with gamma sensor probes [11-14], and 3) lymphosonography, the injection of ultrasound contrast agents that can be detected by contrast-enhanced ultrasound imaging [15, 16].

In this chapter, we extend the less-invasive nature of the SLNB and propose histotripsy tissue fractionation as a noninvasive approach for metastatic SLN ablation, which could potentially lead to decreased number of lymphedemas and fewer other complications. Since lymph nodes are small (size: 5 – 40 mm, average 11 mm in porcine models) and very shallow (depth: 5 – 40 mm in porcine models), the precise lesion formation techniques developed in this dissertation can benefit treatment precision and efficiency in lymph node tissue ablation. In particular, the microtripsy approach using the intrinsic threshold mechanism could limit shock scattering process and restrict lesions in the supra-intrinsic-threshold regions (smaller than the diffraction limit), thus limiting prefocal cavitation that often occurs with conventional histotripsy using shock scattering. Additionally, the dual-beam histotripsy approach can further decrease the size of the supra-intrinsic-threshold regions and the frequency compounding approach can further minimize positive pressures and the corresponding shock scattering, both leading to more precise and controlled lesion formation.

In the following, we investigated the capability of lymph node ablation (both *in vivo* and *ex vivo*) using histotripsy generated by the 1) shock scattering mechanism and the 2) intrinsic threshold mechanism (microtripsy approach).

6.2 Methods

6.2.1 Animal/Tissue Preparation

All procedures associated with this animal study have been approved by the University Committee on Use and Care of Animals (UCUCA) of the University of Michigan. The *in vivo* experiments were performed on six mixed-breed pigs, four females and two males, ranging from 31 to 50 kg in weight and 11 to15 weeks old in age. Prior to treatment, porcine subjects were anesthetized with an intramuscular (IM) injection of Telazol (6 mg/kg) combined with Xylazine (2.2 mg/kg). An intravenous catheter was placed in the auricular vein of each porcine subject. Each porcine subject underwent endotracheal intubation and was maintained on isoflurane gas (1-3.5%) throughout the surgical procedure. The heart rate, oxygen saturation, body temperature, and respiration rate were continuously monitored.

For the *ex vivo* experiments, seven lymph nodes were collected from three porcine subjects from an unrelated study, kept in 0.9% saline at 4℃, and used within 36 hours. Before the experiments, the lymph nodes and surrounding tissues were submerged in degassed 0.9% saline and placed in a chamber under partial vacuum (~33 kPa, absolute) at room temperature for 1 – 2 hours. The tissues were then embedded in a 1% agarose hydrogel that consisted of agarose and 0.9% saline. In two selected lymph nodes, methylene blue dye was administered through an injection using a 25-gauge needle. In another two selected lymph nodes, methylene blue dye and ultrasound contrast agents were administered through an injection using a 25-gauge needle.

6.2.2 Experimental Setup and Histotripsy Therapy Apparatus

Figure 6.1 illustrates the experimental setup for the *in vivo* and *ex vivo* experiments. For the *in vivo* experiments, the porcine subjects were placed on an operational table in supine position after anesthesia. To ensure ultrasonic propagation to the targeted lymph node, a heated degassed water bolus was placed on the skin immediately above the intended target, with a thin plastic membrane and ultrasound gel coupled to the skin. The histotripsy treatment was applied to the targeted lymph node using a 1 MHz, 10-element therapeutic ultrasound transducer that was submerged in the water bolus. The therapeutic ultrasound transducer was attached to a computer-controlled 3-axis motorized positioning system (Parker Hannafin, Rohnert Park, CA, USA). The treatment was guided by ultrasound B-mode imaging using a clinical ultrasound imaging probe, ATL CL15-7 (Advanced Technology Laboratories, Inc., Bothell, WA, USA), in combination with a commercial ultrasound system, ATL HDI 5000. In one selected porcine subjects, a 1.5 MHz, 6-element therapeutic ultrasound transducer was used for lymph node treatment, and the treatment was guided by an ATL L12-5 imaging probe in combination with the ATL HDI 5000 ultrasound system.

For the *ex vivo* experiments, dissected lymph nodes were embedded in agarose hydrogel, attached to a 3-axis motorized positioning system, submerged in a degassed water tank, and sonicated by the 1.5 MHz, 6-element ultrasound transducer. The treatment is guided by the ATL L12-5 imaging probe along with the ATL HDI 5000 ultrasound system.

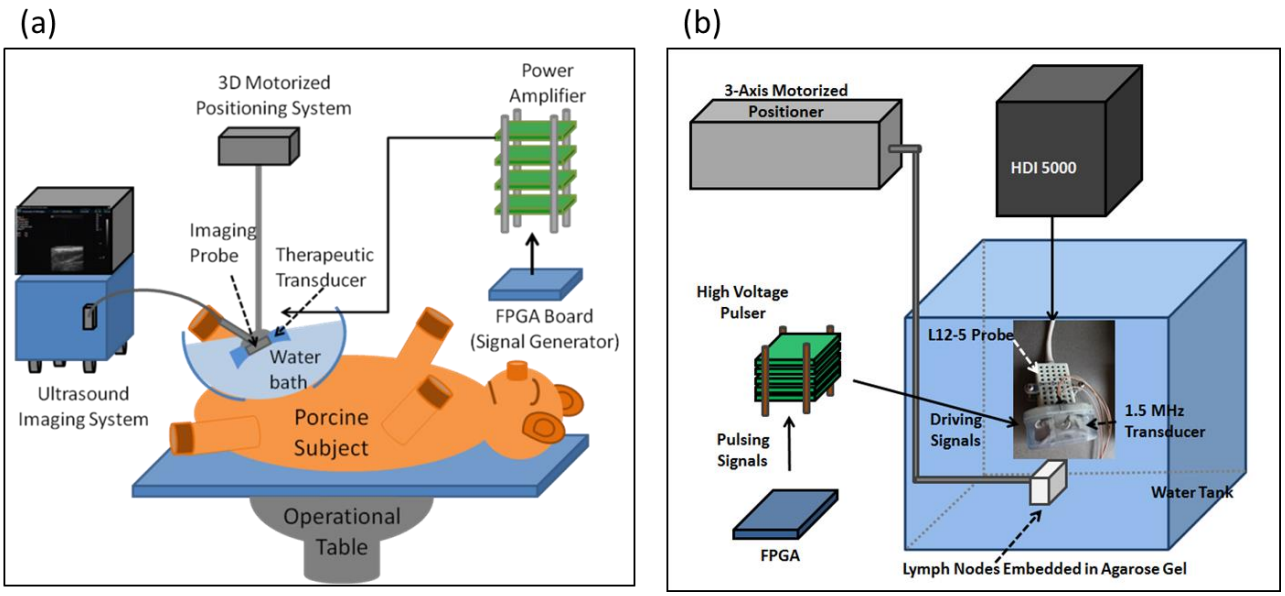

Figure 6.1 Experimental setup for the *in vivo* (a) and *ex vivo* (b) experiments.

The 10-element, 1 MHz therapeutic transducer was made from ten piezoceramic 20-mm-diameter disks (SM111, Steiner & Martins, Inc., Miami, FL, USA) and had a custom center hole to accommodate the imaging probe, ATL CL 15-7, as shown in Figure 6.2(a). This transducer has effective f-numbers of 0.8 in the elevational direction and 0.6 in the lateral direction and a focal length of 52 mm. This transducer was driven by custom class-D power amplifiers that were connected to a field-programmable gate array (FPGA) development board (Altera DE1, Terasic Technology, Dover, Delaware, USA) in order to control ultrasound pulsing sequences. The 6-element, 1.5 MHz therapeutic transducer consisted of six piezoceramic, square, 22.5 × 22.5 mm plates (SM111, Steiner and Martins) and has a custom center hole to accommodate the imaging probe, ATL L12-5, as shown in Figure 6.2(c). This transducer has effective f-numbers of 0.7 in the elevational direction and 0.8 in the lateral direction and a focal length of 55 mm. This transducer was driven by a custom high voltage pulser that allowed the transducer to generate

1.5-cycle pulses. The pulser was connected to another FPGA development board (Altera DE1, Terasic Technology) for ultrasound pulsing sequence control.

A fiber-optic probe hydrophone (FOPH) built in-house [17] was used to measure acoustic output pressures of these two therapeutic transducers. Figure 6.2(b) shows the free-field acoustic waveform of a typical 5-cycle pulse generated by the 10-element, 1 MHz therapeutic transducer (driving center frequency = 1.22 MHz), which has measured peak compressional and rarefactional pressures (P+ and P-) of 66 MPa and 23 MPa, respectively. Figure 6.2(d) shows the free-field acoustic waveform of a typical 1.5-cycle pulse generated by the 6-element, 1.5 MHz transducer, which has a measured P+ of 50 MPa and a measured P– of 22 MPa. The actual acoustic pressures used in the experiments for these transducers were higher than the prior measurements, but they were not able to be measured due to instantaneous cavitation on the fiber tip. The 6-dB beam-widths (calculated based on P–) of the 10-element, 1MHz transducer, driven at 1.22 MHz and 5 cycles, were measured to be 0.6 (lateral), 0.7 (elevational), and 4.0 mm (axial). The 6-dB beam-widths (based on P–) for the 6-element, 1.5 MHz transducer were measured to be 1.5 (lateral), 1.9 (elevational), and 4.2 (axial) mm.

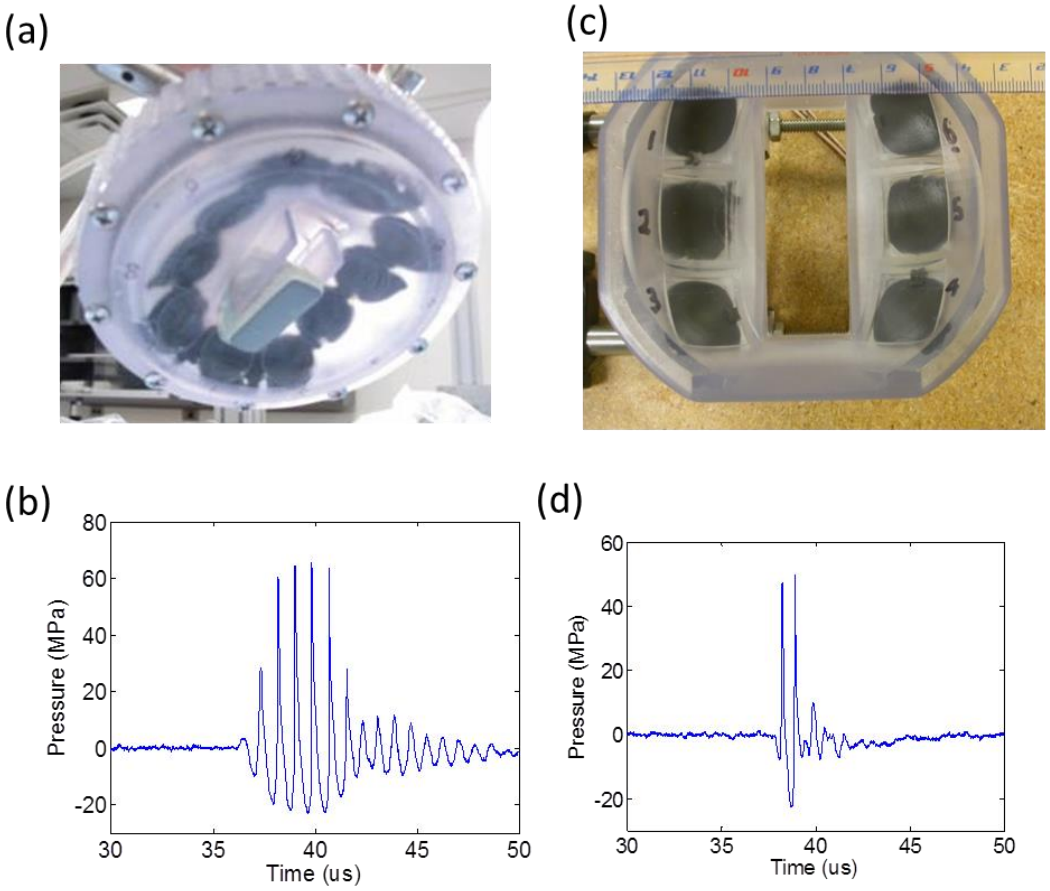

Figure 6.2 (a) 10-element 1 MHz therapeutic transducer with the ATL CL15-7 imaging probe inserted into its center hole. (b) A representative free-field 5-cycle acoustic waveform for the 10-element 1 MHz therapeutic transducer at a lower pressure level than that used in actual treatments. (c) 6-element 1.5 MHz therapeutic transducer. (d) A representative free-field 1.5-cycle acoustic waveform for the 6-element 1.5 MHz therapeutic transducer at a lower pressure level than that used in actual treatments.

6.2.3 Treatment Procedures

For the *in vivo* experiments, prior to treatment, superficial inguinal lymph nodes (mammary for female and scrotal for male) near the lower abdominal area were surveyed using ultrasound imaging, in which lymph nodes appear hypoechoic [Figure 6.3(a)]. Afterwards, the focal point of the therapeutic transducer was identified by firing the transducer above cavitation threshold in degassed water and using ultrasound imaging to track its focal point. The targeted

superficial inguinal lymph nodes were then treated by the 10-element, 1MHz therapeutic transducer with the guidance of ultrasound B-mode imaging, as shown in Figure 6.3(b). The parameters for histotripsy treatment used in this study were a driving center frequency of 1.22 MHz, a pulse repetition frequency (PRF) of 50Hz, a pulse duration of 5 cycles, a P+ of above 66MPa, and a P– of above 23 MPa, and a total of 20000 – 40000 pulses at each treatment location. In one selected case, the lymph node was treated by 6-element, 1.5 MHz transducer with a PRF of 50 Hz, a pulse duration of 1.5 cycles, a P+ of above 61 MPa, a P– of above 26 MPa, and a total of 2000 pulses at each treatment location.

For the *ex vivo* experiments, a similar approach was used, including surveying lymph nodes with ultrasound B-mode imaging, identifying transducer focus by generating bubble cloud in degassed water, and then applying histotripsy treatment at the targeted locations within lymph nodes. In these *ex vivo* experiments, all the lymph nodes were treated by the 6-element, 1.5 MHz transducer with a PRF of 50 – 200 Hz, a pulse duration of 1.5 cycles, a P+ of above 61 MPa, a P– of above 26 MPa, and a total of 2000 – 4000 pulses at each treatment location.

6.2.4 Post Treatment Process and Histological Evaluation

After histotripsy treatment, the porcine subjects in the *in vivo* experiments were euthanized with an intravenous (IV) injection of sodium pentobarbital (140-160 mg/kg). The treated lymph nodes and surrounding tissue were dissected out, and the treated samples were fixed with 10% phosphate buffered formalin (Fisher Scientific, Fair Lawn, NJ) and further processed into histological sections with hematoxylin and eosin (H&E) staining to determine the treatment effect. Lymph nodes in the *ex vivo* experiments were directly removed from agarose

hydrogel, fixed with 10% phosphate buffered formalin, and further processed into histological sections with H&E staining.

6.3 Results

6.3.1 Cases with 5-cycle Pulses (Histotripsy using the Shock-Scattering Mechanism)

A total of seven lymph nodes from five porcine subjects were sonicated *in vivo* by 5-cycles pulses generated by the 10-element 1 MHz transducer. No significant vital sign change occurred during the treatments, and the porcine subjects remained stable from the beginning of anesthesia through euthanasia. The depths from the skin surface to the top of the lymph node (calculated based on ultrasound B-mode images) averaged 3.7 mm, ranging from 2.5 to 6 mm. Histotripsy-generated cavitational bubble clouds were visualized and monitored using B-mode ultrasound imaging, as shown in Figure 6.3. Among all subjects in this case, consistent cavitational bubble clouds were generated in five lymph nodes from four porcine subjects, whereas only intermittent cavitational bubble clouds were generated in two lymph nodes from one porcine subject, possibly due to the preferential surface cavitation on the plastic membrane coupled with skin.

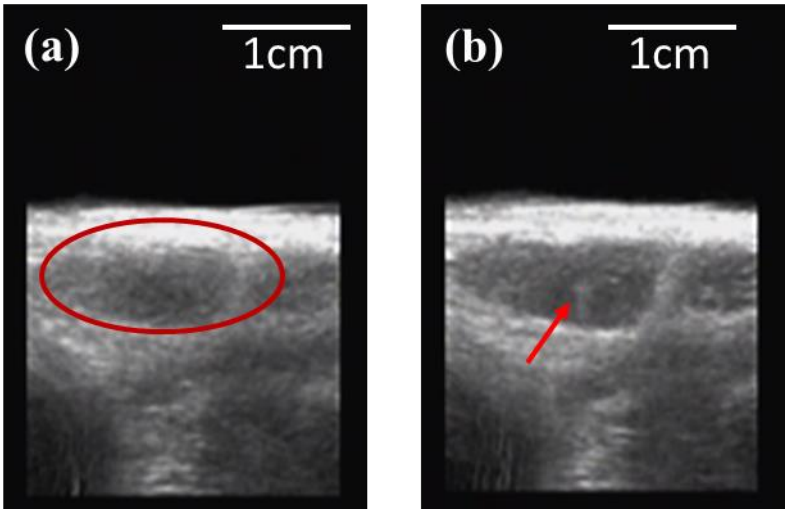

Figure 6.3 Representative ultrasound B-mode images for the lymph nodes treated with histotripsy using shock-scattering mechanism (5-cycle pulses). (a) A B-mode image before treatment. The red ellipse indicates the targeted lymph node, which appears hypoechoic. (b) A B-mode image during treatment. The hyperechoic region indicated by the red arrow is the generated cavitational bubble cloud.

Treatment outcome was evaluated by the gross appearance of the dissected, fixed lymph nodes and their histological sections. Figure 6.4 shows representative results of one lymph node wherein consistent cavitational bubble clouds were generated. Three treatment locations with 1 mm lateral separation were performed within the lymph node and each location was treated for ~ 20,000 pulses at a PRF of 50 Hz. As seen in Figure 6.4(a), after formalin fixation, the treated regions appear dark brown instead of the light yellow that appears in the surrounding untreated region. The histological results [Figures 6.4(b), (c), and (d)] show that only the targeted lymph node is affected by histotripsy treatment and this lymph node has a well-demarcated focus of necrosis (cell death) with minimal damage to the adjacent tissue. In the affected area, the cortical and medullary architectures are disrupted by eosinophilic granular-to-fibrillar cellular debris. In contrast, the adjacent tissue within the targeted lymph node has normal architecture, and adjacent lymph nodes are unaffected.

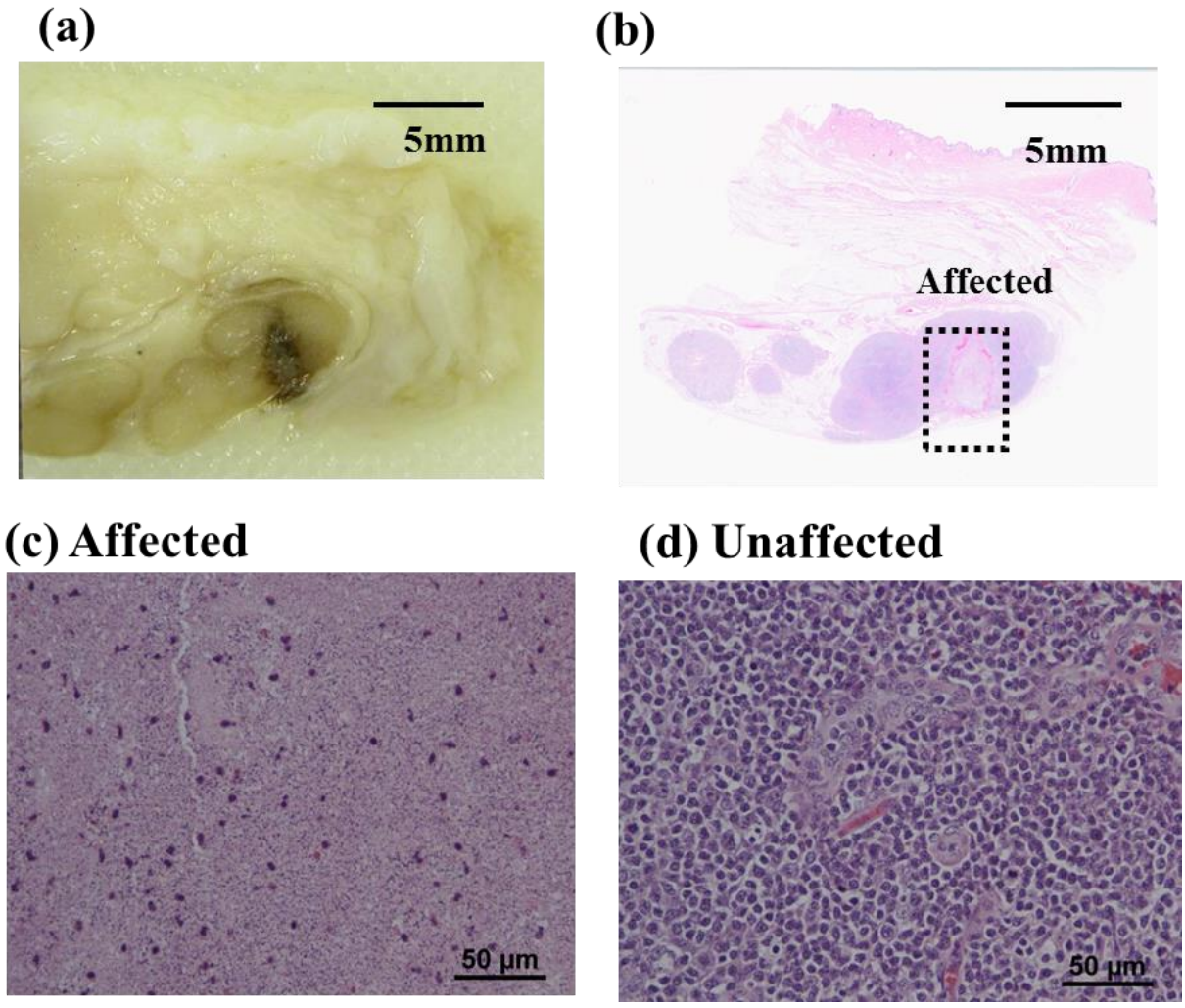

Figure 6.4 Representative lymph node treatment outcome wherein consistent bubble clouds were generated. (a) The treated lymph node after dissection and formalin fixation (b) The histological section of the lymph node and its surrounding tissue. (c) A magnified (400X) image of the affected region within the treated lymph node. (d) A magnified (400X) image of the unaffected region within the treated lymph node.

Additionally, in Figure 6.4, there are varying degrees of hemorrhage and inflammatory response – particularly by eosinophils. Although these are present at the periphery of the lesion in each lymph node, there are also numerous degenerate eosinophils present within the lesion itself. The predominance of eosinophils over neutrophils in this acute inflammatory response is likely a species-specific characteristic since pigs normally have relatively numerous tissue

eosinophils in many peripheral organs (including lymph node) and these are frequently part of the acute inflammatory response in this species. [18].

Figure 6.5 shows the histological result of the lymph node treatment wherein only intermittent cavitational bubble clouds were generated during treatment. The treatment location was manually moved within the lymph node and the total number of treatment pulses was ~ 24,000, pulsing at a PRF of 50 Hz. As can be seen, in the treated regions, the cortical and medullary architectures are partially disrupted, and the regions appear as mixtures of complete obliteration, incomplete obliteration, and hemorrhaging zones. The adjacent tissue within the targeted lymph nodes has normal architecture, and no apparent damage is observed.

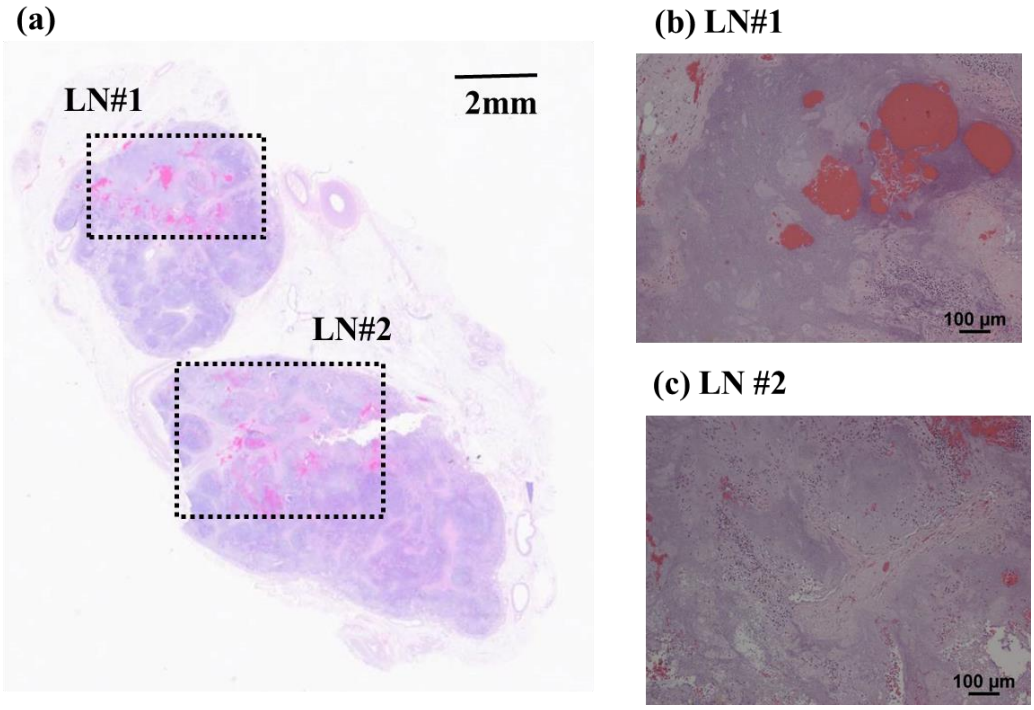

Figure 6.5 Representative lymph node treatment wherein only intermittent cavitational bubble clouds were generated. (a) The histological section of the affected lymph nodes, LN#1 and LN#2. (b) A magnified (100X) image of the affected region in LN#1, in which a mixture of complete obliteration, incomplete obliteration and hemorrhaging regions can be observed. (c) A magnified (100X) image of the affected region in LN#2, in which a qualitatively similar focus of necrosis can be observed.

6.3.2 Case with 1.5-cycle Pulses (Histotripsy using the Intrinsic Threshold Mechanism)

For the cases sonicated with 1.5-cycle pulses generated by 6-element 1.5 MHz transducer, a total of one lymph node from one porcine subject was treated *in vivo* and a total of seven lymph nodes from three porcine subjects were treated *ex vivo*. For the *in vivo* treatment, no significant vital sign change occurred during the treatments, the porcine subjects remained stable from the beginning of anesthesia through euthanasia, and the depth from the skin surface to the top of the lymph node was approximately 3 mm. Among all lymph nodes, consistent bubble clouds were generated, and no significant prefocal cavitation was observed. Figure 6.6 shows the representative B-mode images during (a) and after (b) the histotripsy treatment for the *in vivo* experiment (treatment parameters: a PRF of 50 Hz, a total of 2000 pulses at each treatment location, and a total of 35 treatment locations which covered 4 × 6 mm treatment region). Its corresponding histology section is shown in Figure 6.7. As can be seen in the histology, the lymph node has a well-demarcated focus of necrosis (cell death) with minimal damage to the adjacent tissue.

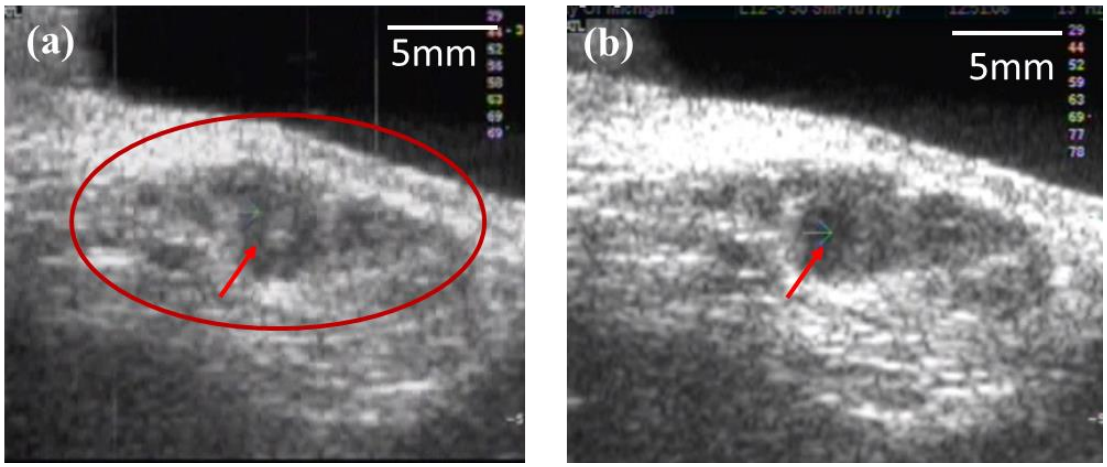

Figure 6.6 Representative ultrasound B-mode imaging for the *in vivo* lymph nodes treatment using 1.5-cycle histotripsy pulses (intrinsic threshold mechanism). (a) A B-mode image during treatment. The red ellipse indicates the targeted lymph node, which appears hypoechoic, and the red arrow indicates the generated bubble cloud, which appears hyperechoic. (b) A B-mode image after treatment. The hypoechoic region indicated by the red arrow is the treated region.

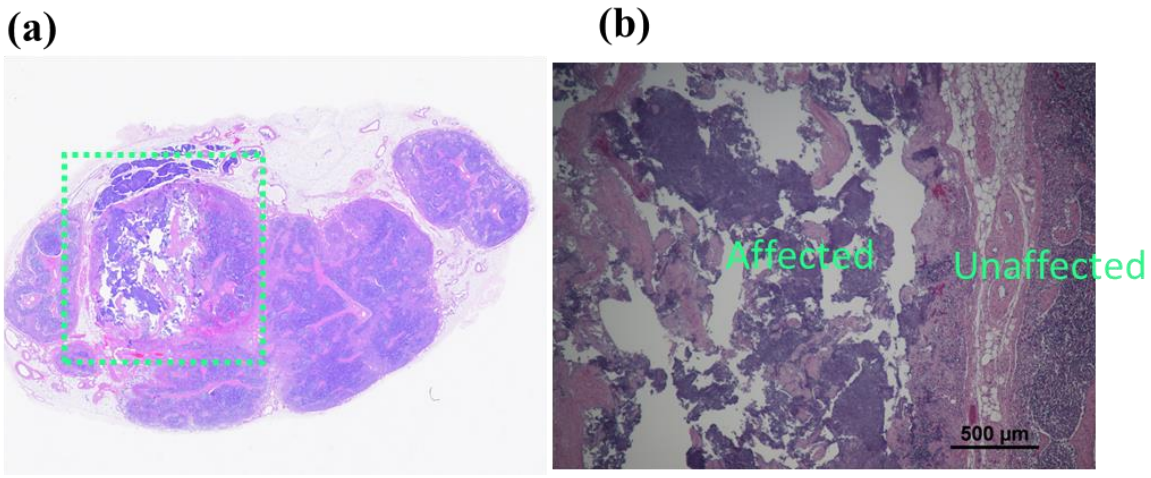

Figure 6.7 Histological sections of the lymph node treated *in vivo* using 1.5-cycle histotripsy pulses (intrinsic threshold mechanism). (a) An overall view of the lymph node. (b) A magnified view at the boundary between the affected and unaffected regions.

Representative results for the *ex vivo* experiments without contrast agents are shown in Figure 6.8. (Treatment parameters: a PRF of 200 Hz, a total of 4000 pulses at each treatment location, and a total of 65 treatment locations which covered 4 × 6 mm treatment region) As can be seen in Figures 6.8(a) and (b), the backscatter intensity of the treated region decreased slightly, and the histology sections in Figures 6.8 (c) – (e) shows that the treated lymph nodes had well-demarcated foci of necrosis with minimal damage to adjacent tissue. For the lymph nodes with microbubble injection, the histological sections appeared similar to the ones without contrast agents. No microbubbles were observed in the histology section, in which micorbubbles were possibly disrupted by either the histotripsy treatment or the histology preparation process (e.g. formalin fixation).

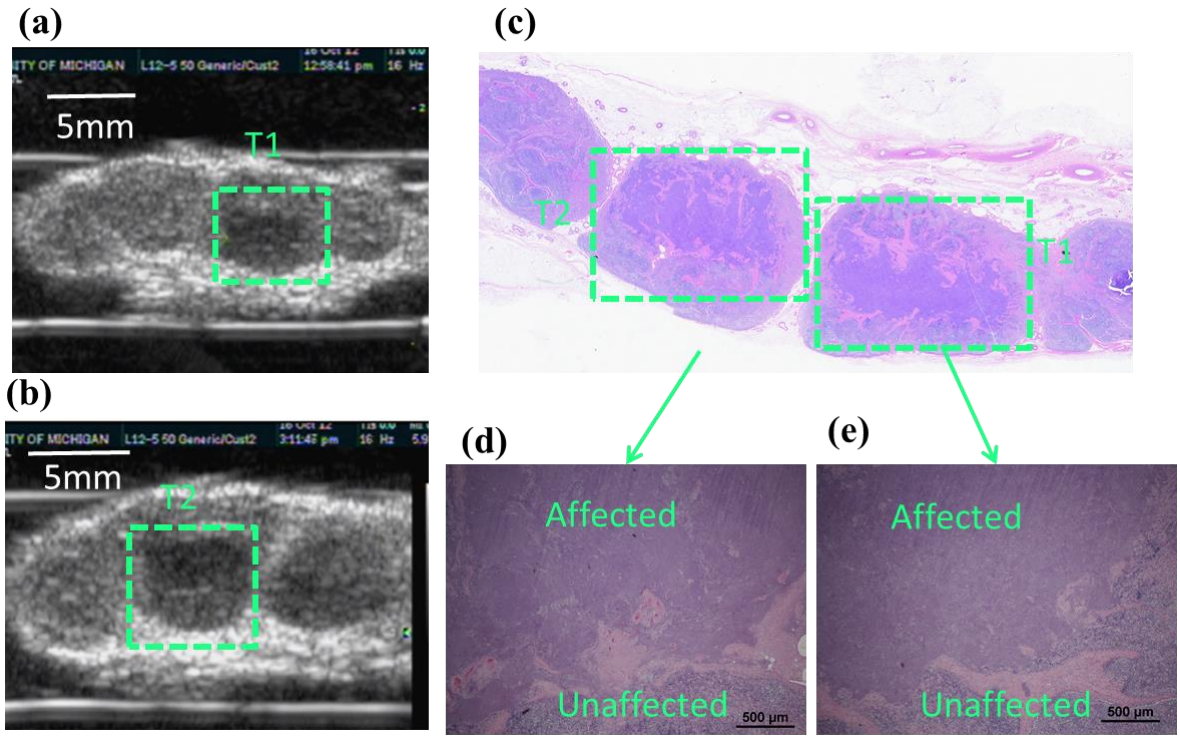

Figure 6.8 Representative results for *ex vivo* experiments using 1.5-cycle histotripsy pulses (intrinsic threshold mechanism). (a) A B-mode image for the first treatment location (T1) (b) A B-mode image for the second treatment location (T2) (c) The overall histological section which includes both T1 and T2 treatments. (d) A magnified view of the histological section of the T2 treatment (e) A magnified view of the histological section of the T1 treatment.

6.4 Discussion

This chapter demonstrates the capability of histotripsy to noninvasively generate well-demarcated tissue fractionation within the targeted superficial lymph nodes. This noninvasive lymph node ablation could potentially reduce the side effects, such as lymphedema, that are associated with conventional lymph node dissection [9].

When lymph nodes were exposed to 5-cycle histotripsy pulses, most of the cases had consistent cavitational bubble clouds generated, though, in a small number of cases, only intermittent bubble clouds generated. This is possibly due to the shielding effect generated by the preferential surface cavitation on the skin surface, and this often happens when the lymph node is

too superficial and histotripsy with pulses longer than 3 cycles are applied. The previous paper [19] showed that, when histotripsy pulses longer than 3 cycles were applied, the latter acoustic shockwave cycles would be backscattered by pre-existing bubbles that were initiated from initial cycles, thus leading to the growth of bubble clouds along the acoustic axis, opposite the direction of the ultrasound propagation (shock-scattering).

On the other hand, when lymph nodes were exposed to supra-intrinsic-threshold 1.5-cycle histotripsy pulses, consistent cavitational bubble clouds were generated in all cases. Though only one porcine subject was treated *in vivo*, the results from both *in vivo* and *ex vivo* experiments showed that histotripsy using the intrinsic threshold mechanism could potentially lower the probability of prefocal cavitation, thus increasing the consistency of bubble cloud generation at the focus and the treatment efficiency.

In the experiment that combined histotripsy with microbubbles, the result showed that the injection of the microbubbles did not impede the formation of cavitational bubble clouds, and a well-demarcated tissue fractionation region was observed after histotripsy treatment. In fact, several other studies [20-22] have shown that stabilized microbubbles can serve as nuclei for cavitation, thus leading to the reduction of the cavitation threshold and the enhancement of the cavitation therapy. Therefore, introducing contrast-specific ultrasound imaging for SLN detection (lymphosonography) should not decrease the efficiency of the histotripsy treatment.

In some applications, histotripsy-treated regions have decreased backscatter intensity under B-mode imaging [23, 24], which can be used as a real-time image feedback and guidance for the treatment. In this lymph node ablation application, though we observed backscatter intensity reduction in the cases with a larger treated volume, this backscattered intensity reduction was not as pronounced as the other tissue types studied in [23, 24], possibly due to the

low echogenicity nature of lymph nodes. A possible alternative for providing real-time image feedback for histotripsy lymph node ablation is ultrasound elasticity imaging. This imaging modality has demonstrated its capability of differentiating benign and malignant masses in lymph nodes [25, 26]. Additionally, it has been shown (in [27, 28]) that it can provide image feedback for histotripsy, wherein tissue elasticity decreases due to the fractionation process generated by histotripsy.

6.5 Conclusion

A noninvasive lymph node ablation approach that uses histotripsy tissue fractionation was proposed and investigated in this study. With the application of histotripsy pulses, cavitational bubble clouds were successfully generated within the targeted lymph nodes, especially with the supra-intrinsic-threshold 1.5-cycle pulses. Porcine subjects did not experience any significant vital sign change during and after histotripsy treatment. Histological results showed that the targeted regions within the targeted lymph nodes had well-demarcated foci of necrosis with minimal damage to the adjacent tissue. Furthermore, the intervening skin and fat tissue and the non-targeted lymph nodes remained unaffected after the treatment. These results demonstrate the feasibility of histotripsy tissue fractionation in noninvasive lymph node ablation.

6.6 References

[1] A. Recht and M. J. Houlihan, "Axillary lymph nodes and breast cancer: a review," *Cancer,* vol. 76, pp. 1491-512, Nov 1 1995.

[2] C. F. Mountain and C. M. Dresler, "Regional lymph node classification for lung cancer staging," *Chest,* vol. 111, pp. 1718-23, Jun 1997.

[3] J. J. Bonenkamp, J. Hermans, M. Sasako, C. J. van de Velde, K. Welvaart, I. Songun, S. Meyer, J. T. Plukker, P. Van Elk, H. Obertop, D. J. Gouma, J. J. van Lanschot, C. W.

Taat, P. W. de Graaf, M. F. von Meyenfeldt, and H. Tilanus, "Extended lymph-node dissection for gastric cancer," *N Engl J Med*, vol. 340, pp. 908-14, Mar 25 1999.

[4] A. Briganti, M. L. Blute, J. H. Eastham, M. Graefen, A. Heidenreich, J. R. Karnes, F. Montorsi, and U. E. Studer, "Pelvic lymph node dissection in prostate cancer," *Eur Urol*, vol. 55, pp. 1251-65, Jun 2009.

[5] B. Cady, "The need to reexamine axillary lymph node dissection in invasive breast cancer," *Cancer*, vol. 73, pp. 505-8, Feb 1 1994.

[6] E. D. Paskett and N. Stark, "Lymphedema: Knowledge, Treatment, and Impact Among Breast Cancer Survivors," *The Breast Journal*, vol. 6, pp. 373-378, 2000.

[7] D. N. Krag, D. L. Weaver, J. C. Alex, and J. T. Fairbank, "Surgical resection and radiolocalization of the sentinel lymph node in breast cancer using a gamma probe," *Surg Oncol*, vol. 2, pp. 335-9; discussion 340, Dec 1993.

[8] D. N. Krag, S. J. Anderson, T. B. Julian, A. M. Brown, S. P. Harlow, J. P. Costantino, T. Ashikaga, D. L. Weaver, E. P. Mamounas, L. M. Jalovec, T. G. Frazier, R. D. Noyes, A. Robidoux, H. M. Scarth, and N. Wolmark, "Sentinel-lymph-node resection compared with conventional axillary-lymph-node dissection in clinically node-negative patients with breast cancer: overall survival findings from the NSABP B-32 randomised phase 3 trial," *Lancet Oncol*, vol. 11, pp. 927-33, Oct 2010.

[9] S. A. McLaughlin, M. J. Wright, K. T. Morris, G. L. Giron, M. R. Sampson, J. P. Brockway, K. E. Hurley, E. R. Riedel, and K. J. Van Zee, "Prevalence of lymphedema in women with breast cancer 5 years after sentinel lymph node biopsy or axillary dissection: objective measurements," *J Clin Oncol*, vol. 26, pp. 5213-9, Nov 10 2008.

[10] S. A. McLaughlin, M. J. Wright, K. T. Morris, M. R. Sampson, J. P. Brockway, K. E. Hurley, E. R. Riedel, and K. J. Van Zee, "Prevalence of lymphedema in women with breast cancer 5 years after sentinel lymph node biopsy or axillary dissection: patient perceptions and precautionary behaviors," *J Clin Oncol*, vol. 26, pp. 5220-6, Nov 10 2008.

[11] A. Mudun, D. R. Murray, S. C. Herda, D. Eshima, L. A. Shattuck, J. P. Vansant, A. T. Taylor, and N. P. Alazraki, "Early stage melanoma: lymphoscintigraphy, reproducibility of sentinel node detection, and effectiveness of the intraoperative gamma probe," vol. 199, ed, 1996, pp. 171-175.

[12] A. P. Yudd, J. S. Kempf, J. S. Goydos, T. J. Stahl, and R. S. Feinstein, "Use of Sentinel Node Lymphoscintigraphy in Malignant Melanoma," vol. 19, ed, 1999, pp. 343-356.

[13] P. J. Borgstein, R. Pijpers, E. F. Comans, P. J. van Diest, R. P. Boom, and S. Meijer, "Sentinel lymph node biopsy in breast cancer: guidelines and pitfalls of lymphoscintigraphy and gamma probe detection," *J Am Coll Surg*, vol. 186, pp. 275-83, Mar 1998.

[14] J. E. Gershenwald, M. I. Colome, J. E. Lee, P. F. Mansfield, C. Tseng, J. J. Lee, C. M. Balch, and M. I. Ross, "Patterns of recurrence following a negative sentinel lymph node biopsy in 243 patients with stage I or II melanoma," *Journal of Clinical Oncology,* vol. 16, pp. 2253-60, June 1, 1998 1998.

[15] F. Forsberg, R. J. Ro, T. B. Fox, J. B. Liu, S. Y. Chiou, M. Potoczek, and B. B. Goldberg, "Contrast enhanced maximum intensity projection ultrasound imaging for assessing angiogenesis in murine glioma and breast tumor models: A comparative study," *Ultrasonics,* vol. 51, pp. 382-9, Apr 2011.

[16] B. B. Goldberg, D. A. Merton, J. B. Liu, F. Forsberg, K. Zhang, M. Thakur, S. Schulz, R. Schanche, G. F. Murphy, and S. A. Waldman, "Contrast-enhanced ultrasound imaging of sentinel lymph nodes after peritumoral administration of Sonazoid in a melanoma tumor animal model," *J Ultrasound Med,* vol. 30, pp. 441-53, Apr 2011.

[17] J. E. Parsons, C. A. Cain, and J. B. Fowlkes, "Cost-effective assembly of a basic fiber-optic hydrophone for measurement of high-amplitude therapeutic ultrasound fields," *J Acoust Soc Am,* vol. 119, pp. 1432-40, Mar 2006.

[18] J. A. Vilpo, M. J. Harkonen, and H. Teir, "Distribution of tissue eosinophil granulocytes in cow and pig organs," *Scand J Haematol,* vol. 7, pp. 217-21, 1970.

[19] A. D. Maxwell, T. Y. Wang, C. A. Cain, J. B. Fowlkes, O. A. Sapozhnikov, M. R. Bailey, and Z. Xu, "Cavitation clouds created by shock scattering from bubbles during histotripsy," *J Acoust Soc Am,* vol. 130, pp. 1888-98, Oct 2011.

[20] E. C. Unger, T. O. Matsunaga, T. McCreery, P. Schumann, R. Sweitzer, and R. Quigley, "Therapeutic applications of microbubbles," *European journal of radiology,* vol. 42, pp. 160-168, 2002.

[21] B. C. Tran, S. Jongbum, T. L. Hall, J. B. Fowlkes, and C. A. Cain, "Microbubble-enhanced cavitation for noninvasive ultrasound surgery," *Ultrasonics, Ferroelectrics and Frequency Control, IEEE Transactions on,* vol. 50, pp. 1296-1304, 2003.

[22] D. L. Miller and R. M. Thomas, "Ultrasound contrast agents nucleate inertial cavitation in vitro," *Ultrasound in medicine & biology,* vol. 21, pp. 1059-1065, 1995.

[23] T. L. Hall, J. B. Fowlkes, and C. A. Cain, "A real-time measure of cavitation induced tissue disruption by ultrasound imaging backscatter reduction," *IEEE Trans Ultrason Ferroelectr Freq Control,* vol. 54, pp. 569-75, Mar 2007.

[24] T. Y. Wang, Z. Xu, F. Winterroth, T. L. Hall, J. B. Fowlkes, E. D. Rothman, W. W. Roberts, and C. A. Cain, "Quantitative ultrasound backscatter for pulsed cavitational ultrasound therapy- histotripsy," *IEEE Trans Ultrason Ferroelectr Freq Control,* vol. 56, pp. 995-1005, May 2009.

[25] M. Giovannini, L. C. Hookey, E. Bories, C. Pesenti, G. Monges, and J. R. Delpero, "Endoscopic ultrasound elastography: the first step towards virtual biopsy? Preliminary results in 49 patients," *Endoscopy*, vol. 38, pp. 344-8, Apr 2006.

[26] A. Saftoiu, P. Vilmann, T. Ciurea, G. L. Popescu, A. Iordache, H. Hassan, F. Gorunescu, and S. Iordache, "Dynamic analysis of EUS used for the differentiation of benign and malignant lymph nodes," *Gastrointestinal Endoscopy*, vol. 66, pp. 291-300, 2007.

[27] T. Y. Wang, T. L. Hall, Z. Xu, J. B. Fowlkes, and C. A. Cain, "Imaging feedback of histotripsy treatments using ultrasound shear wave elastography," *Ultrasonics, Ferroelectrics and Frequency Control, IEEE Transactions on*, vol. 59, pp. 1167-1181, 2012.

[28] R. M. Miller, A. D. Maxwell, T.-Y. Wang, J. B. Fowlkes, C. A. Cain, and X. Zhen, "Real-time elastography-based monitoring of histotripsy tissue fractionation using color Doppler," in *Ultrasonics Symposium (IUS), 2012 IEEE International*, 2012, pp. 196-199.

Chapter 7
Summary and Future Work

7.1 Summary

This dissertation demonstrates that histotripsy, a noninvasive, cavitation-based ultrasound therapy, can create highly precise lesions using strategic pulsing methods proposed herein. More specifically, three approaches for precise lesion formation are developed and investigated in this dissertation including microtripsy using intrinsic threshold mechanism, dual-beam histotripsy, and near monopolar pulse generation using frequency compounding.

1) Microtripsy using intrinsic threshold mechanism: With ultrasound pulses shorter than 3 cycles, the generation of a dense bubble cloud only depends on one or two negative half cycles exceeding an intrinsic threshold of the medium. In fact, a single almost monopolar negative pulse can generate lesion-forming bubble cloud [1]. This intrinsic threshold is highly repeatable and has a very sharp transition zone. With a P– not significantly higher than the threshold, precise and sub-wavelength lesions can be produced; hence we called it "microtripsy". The sizes of the smallest reproducible lesions in the lateral direction were even smaller than the diffraction limited –6dB focal pressure, $\lambda/2$. Additionally, the sizes of the lesions corresponded well to the dimensions of the focal beam profile estimated to be beyond the intrinsic threshold, although there was a discrepancy at higher applied pressure levels ($P- > 35$ MPa).

This is most likely accounted for by an increase in the size of the P– focal zone as a result of nonlinear propagation processes [2].

2) Dual-beam histotripsy: A low-frequency pump pulse is applied to enable a high-frequency probe pulse for precise lesion formation. This lesion formation only occurred when the pump and probe pulses constructively interfered and the combined P– exceeded the intrinsic threshold. With a higher proportion of the high-frequency probe pulse, a smaller lesion could be generated. The shape and size of the lesion could further be altered by changing the relative propagation direction between the pump and probe pulses [3]. Additionally, an imaging transducer could provide the high-frequency probe pulse for dual-beam histotripsy wherein the lesion could be easily controlled and steered using the imaging transducer in conjunction with a programmable ultrasound imaging system [4]. This dual-beam histotripsy can be useful in clinical applications in which precise tissue ablation is required with a longer propagation depth or through a highly attenuative or aberrative medium, especially if a small low-attenuation acoustic window is available for high frequency probe pulses (which can be provided by an imaging probe).
3) Near monopolar pulses generated by frequency compounding: Using an array transducer composed of elements with various resonant frequencies, a near monopolar negative-polarity pulse could be generated by constructively combining their negative peaks at the focus. A near monopolar positive-polarity pulse could be generated in a similar way by constructively combining their positive peaks. Using negative-polarity monopolar pulses can potentially result in more precise lesion formation in histotripsy as the shock scattering process is completely eliminated.

These monopolar pulses may have many interesting applications in ultrasound diagnostic imaging, for example, pulse inversion contrast imaging. [1]

The first two pulsing methods for histotripsy have been examined and validated in both RBC tissue-mimicking phantoms and *ex vivo* tissues. The third pulsing method has been validated in RBC tissue-mimicking phantoms.

Lastly, an application of precise lesion formation in metastatic lymph node ablation is investigated using bubble cloud generated by single-frequency supra-intrinsic-threshold histotripsy pulses. Lymph nodes are generally small (5 – 40 mm) and shallow (5 – 50 mm), which require precise lesion formation at a superficial location. Both *in vivo* and *ex vivo* experiments demonstrated that supra-intrinsic-threshold histotripsy pulses (microtripsy approach) are capable of producing controlled and precise tissue fractionation in superficial lymph nodes. Bubble clouds generated by the shock scattering mechanism were also investigated in *in vivo* models.

7.2 Future Work

7.2.1 *In Vivo* Validation for Precise Lesion Formation Pulsing Methods

The pulsing methods for precise lesion formation developed in this dissertation have demonstrated their feasibility in RBC tissue-mimicking phantoms and *ex vivo* tissues, and should be further validated in *in vivo* settings.

The study in metastatic lymph node ablation (Chapter 6) demonstrated the capability of supra-intrinsic-threshold pulses in treating *in vivo* porcine lymph node wherein prefocal cavitation was minimized. However, the sample size was only one porcine object. Further *in vivo* studies need to be performed with a larger sample size to demonstrate that supra-intrinsic-

threshold pulses can produce precise lesion formation *in vivo* without causing significant prefocal cavitation. This often happens at boundaries near the focus (like the skin surface) when superficial targets are treated using bubble clouds generated by the shock scattering mechanism.

Additionally, the feasibility of dual-beam histotripsy and frequency-compounded monopolar pulses needs to be investigated with *in vivo* animal studies. As mentioned in the discussion of the Chapter 4, two issues might occur when applying multi-frequency pulses to *in vivo* cases: (1) higher frequency components may suffer significantly more attenuation compared to lower frequency components such that the combined pulses will get distorted, and (2) spatial and temporal alignment between different frequency components may deteriorate due to various attenuation and aberration. Though possible solutions has been proposed in the same discussion section, such as amplitude compensation that increases the output pressure of higher frequency components or increases the number of higher frequency elements of the array, *in vivo* studies needs to be conducted to examine the significance of these issues in *in vivo* cases and the efficiency of the proposed solutions in addressing these issues.

7.2.2 Imaging Applications for Frequency Compounding

Chapter 5 demonstrates the feasibility of using frequency-compounded monopolar pulses for histotripsy treatment, and discusses their potential applications in diagnostic ultrasound imaging.

Pulse inversion contrast imaging should be investigated. Conventional pulse inversion imaging transmits two short acoustic (several cycles) pulses with inverted polarity and creates an image that sums the two received signals. Any object that responds to these two pulses non-linearly (i.e. not exactly inverted) will result in a significant signal in the summed image. This

contrast can potentially be amplified when using negative-polarity and positive-polarity monopolar pulses, wherein the negative pulse primarily expands the medium and the positive pulse mainly compresses the medium. If contrast agents are introduced in the imaging region, this contrast could be significantly amplified in the pulse inversion imaging.

The second application is to replace imaging pulses with frequency-compounded monopolar pulses in conventional ultrasound imaging, e.g. plane wave imaging or b-mode imaging. As mentioned in the introduction of Chapter 5, monopolar pulses with minimal oscillatory components could lead to less coherent constructive/destructive interference patterns in the image, thus decreasing its speckle noise (frequency dependence of the speckle noise can also explain why these broadband pulses can reduce speckle noise). However, the current low f-number frequency compounding transducer in Chapter 5 produces monopolar pulses limited to its focal zone, and an ideal array transducer for imaging purposes will need to have a large "monopolar" zone across the imaging plane. This transducer could be a linear array with subsets of modules wherein each module alone can generate monopolar pulses consistently along the propagation axis. Figures 7.1 and 7.2 demonstrate an example design of a module that can create a consistent monopolar zone along the propagation axis. As shown in Figure 7.1(a), five elements with a size of 0.3 × 1.0 mm and various resonant frequencies (0.5, 1.0, 1.5, 2.0, and 3.0 MHz) are arranged linearly and have a total size of 0.3 × 5.0 mm. A simulation using FOCUS software is performed with results shown in Figures 7.1(b) – (g) and 7.2. The individual time delays are chosen to allow their peaks of negative pressures to align at a depth of 15 mm (in the far field of the individual elements). The simulated 2D pressure fields in Figures 7.1(b) – (g) shows that this module with this specific time delay set can lead to a plane of monopolar region (i.e. large P–/P+ ratio). This region is narrow in the lateral direction, and very wide in the

elevational and axial directions. Figure 7.2 shows representative frequency-compounded temporal signals at 10, 15, 20, 30, 40, and 50 mm away from the surface of the center element.

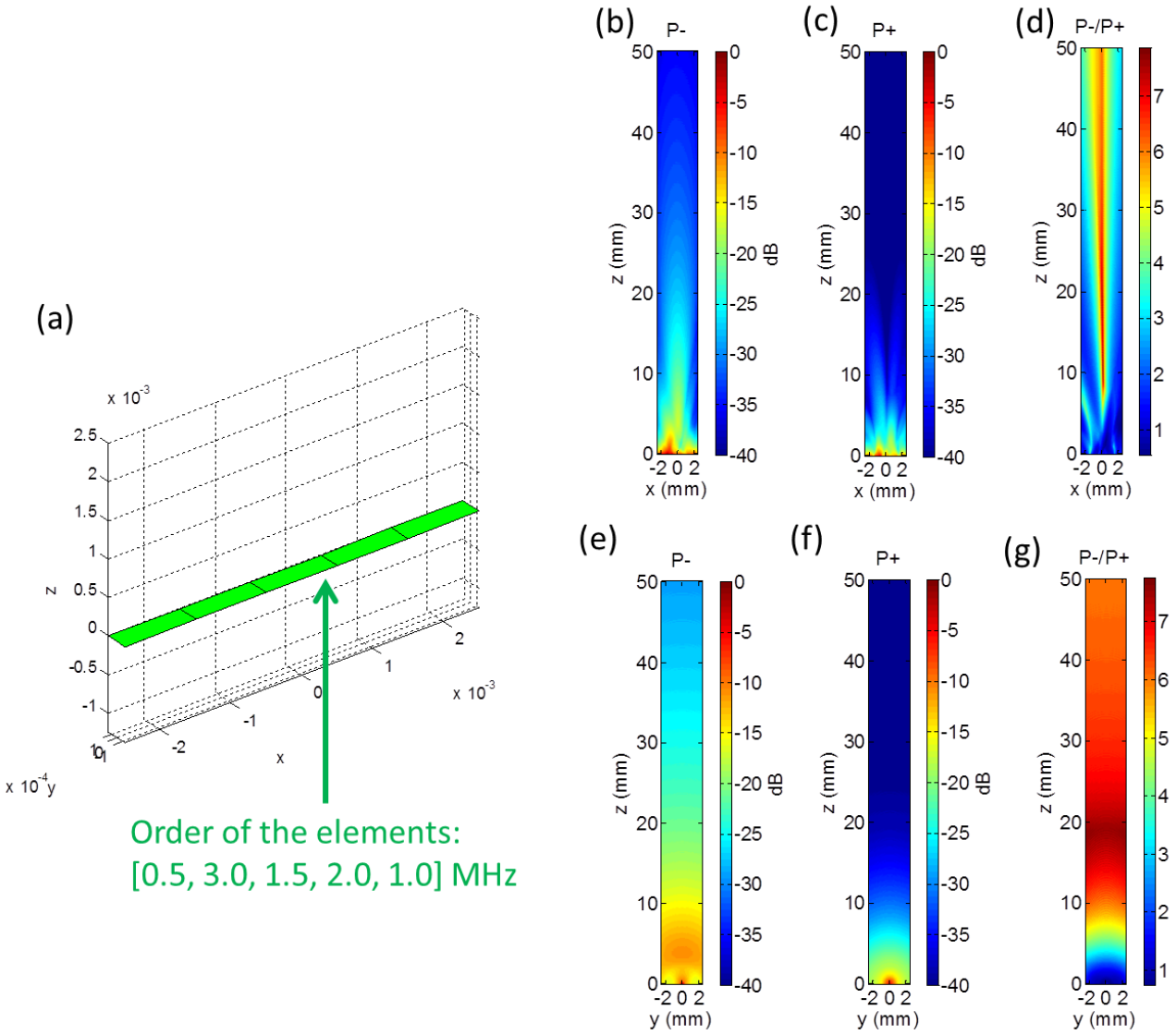

Figure 7.1 A simulation using FOCUS software showing an example of a 5-frequency module that can create a plane of monopolar region. (a) The arrangement of these elements (size of individual elements: 0.3 × 1 mm). The individual time delays are chosen to allow their peak of negative pressure to align at a depth of 15 mm. [X,Y, Z coordinates: (0, 0, 15)] 2-D pressure fields, (b) Normalized P–, (c) Normalized P+, and (d) P–/P+ in the X-Z plane (lateral-axial plane). 2-D pressure fields, (e) Normalized P–, (f) Normalized P+, and (g) P–/P+ in the Y-Z plane (elevational-axial plane).

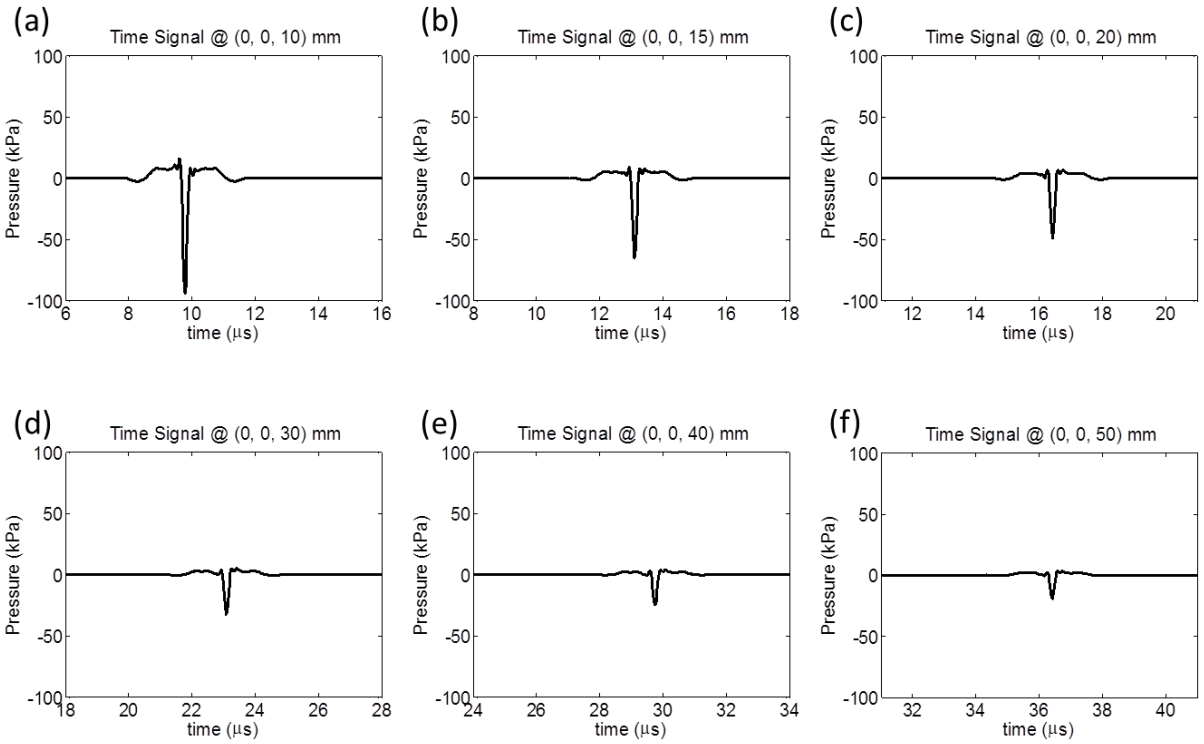

Figure 7.2 Representative FOCUS-simulated temporal signals of the 5-frequency module described in Figure 7.1 at a depth of 10 (a), 15 (b), 20 (c), 30 (d), 40 (e), and 50 (f) mm.

7.2.3 Other Applications in Ophthalmology

The precise lesion formation techniques described in this dissertation could be very useful in ophthalmological applications because of two reasons: (1) eyeballs are small delicate organs that require very precise and microscopic treatment, and (2) eyeballs are very superficial wherein prefocal cavitation often renders problematic treatment for conventional histotripsy using shock scattering mechanism. The microtripsy technique developed in this dissertation can limit shock scattering process and constrain lesions to supra-intrinsic-threshold regions (smaller than the diffraction limit), thus decreasing the extent of prefocal cavitation. The dual-beam histotripsy approach can further reduce the size of the supra-intrinsic-threshold regions with an introduction of a high frequency component in histotripsy pulsing, thus leading to more precise

and confined lesions. Additionally, using near half-cycle negative pulses generated by the frequency-compounding approach could completely diminish shock scattering process, which could further decrease prefocal cavitation and increase treatment precision. Shallow targets like eyeballs have less intervening tissue which could benefit the high frequency components used in these techniques. Two potential ophthalmological applications for these precise lesion formation techniques are described in the following.

Cataract Treatment

Cataract is a clouding of the lens inside the eye which leads to a decrease in vision. It is mostly due to biological aging but may have a wide range of other causes. Over time, yellow-brown pigment is deposited within the lens and this, together with disruption of the normal architecture of the lens fibers, leads to reduced transmission of light. As a result, vision loss occurs due to this opacification of the lens. An estimated 20.5 million (17.2%) Americans older than 40 years old have cataract in either eye [6]. Phacoemulsification [7] is a common surgery that removes cataract, and it can be performed at any stage and no longer requires ripening of the lens. The procedure involves a corneal incision, a phacoemulsification of the cataract with a handheld ultrasonic probe, an aspiration of emulsified content, and an insertion of an artificial intraocular lens.

In this application, we are investigating the possibility of using histotripsy to fractionate or homogenize cataract within lenses noninvasively. In this case, a major incision for phacoemulsification with the handheld ultrasonic probe can be avoided, and only a smaller incision is required for the insertion of the artificial intraocular lens after histotripsy treatment.

Strabismus Treatment

Strabismus (includes cross-eye and wall-eye) is a condition in which the eyes are not properly aligned with each other. It is often resulted from the lack of coordination of the extraocular muscles, and it may affect depth perception adversely. Strabismus affects 3.3% of white and 2.1% of African American children [8]. Current management for strabismus involves a combination of eyeglasses, vision therapy, and surgery, depending on the situation. Surgery shortens, lengthens, or changes the position of one or more of the extraocular muscles in an attempt to align the eyes, and this is often the only way to achieve cosmetic improvement. Botulinum Toxin (Botox) [9] may also be used in treating strabismus, most commonly used in adults. Botox is injected in the stronger extraocular muscle, causing temporary paralysis, but it may be repeated 3 – 4 months later once the paralysis effect wears off.

In this application, we're investigating the possibility of using histotripsy to weaken or paralyze one or more of the extraocular muscles. This would be a noninvasive and non-chemical-injection therapy for strabismus, which can potentially reduce the side effects created by surgery or botox injection.

7.3 References

[1] K.-W. Lin, T. L. Hall, R. J. McGough, Z. Xu, and C. A. Cain, "Synthesis of Monopolar Ultrasound Pulses for Therapy: The Frequency-Compounding Transducer," *IEEE Trans Ultrason Ferroelectr Freq Control,* accepted Jan. 2014.

[2] K.-W. Lin, Y. Kim, A. D. Maxwell, T.-Y. Wang, T. L. Hall, Z. Xu, J. B. Fowlkes, and C. A. Cain, "Histotripsy beyond the Intrinsic Cavitation Threshold using Very Short Ultrasound Pulses: Microtripsy," *IEEE Trans Ultrason Ferroelectr Freq Control,* vol. 61, pp. 251-265, 2014.

[3] K.-W. Lin, A. P. Duryea, Y. Kim, T. L. Hall, Z. Xu, and C. A. Cain, "Dual-Beam Histotripsy: A Low-Frequency Pump Enabling a High-Frequency Probe for Precise Lesion Formation," *IEEE Trans Ultrason Ferroelectr Freq Control,* vol. 61, pp. 325-340, 2014.

[4] K.-W. Lin, T. L. Hall, Z. Xu, and C. A. Cain, "Histotripsy Lesion Formation with an Ultrasound Imaging Probe Enabled by a Low-Frequency Pump Transducer," *IEEE Trans Ultrason Ferroelectr Freq Control,* submitted Feb. 2014.

[5] R. F. Wagner and S. W. Smith, "Statistics of speckle in ultrasound B-scans," *IEEE TRANS. SONICS ULTRASONICS.,* vol. 30, pp. 156-163, 1983.

[6] N. Congdon, J. R. Vingerling, B. E. Klein, S. West, D. S. Friedman, J. Kempen, B. O'Colmain, S. Y. Wu, and H. R. Taylor, "Prevalence of cataract and pseudophakia/aphakia among adults in the united states," *Archives of Ophthalmology,* vol. 122, pp. 487-494, 2004.

[7] M. Packer, W. J. Fishkind, I. H. Fine, B. S. Seibel, and R. S. Hoffman, "The physics of phaco: A review," *Journal of Cataract & Refractive Surgery,* vol. 31, pp. 424-431, 2005.

[8] D. S. Friedman, M. X. Repka, J. Katz, L. Giordano, J. Ibironke, P. Hawse, and J. M. Tielsch, "Prevalence of Amblyopia and Strabismus in White and African American Children Aged 6 through 71 Months: The Baltimore Pediatric Eye Disease Study," *Ophthalmology,* vol. 116, pp. 2128-2134.e2, 2009.

[9] A. B. Scott, "Botulinum toxin injection of eye muscles to correct strabismus," *Trans Am Ophthalmol Soc,* vol. 79, pp. 734-70, 1981.